



**INSTITUTO POLITÉCNICO NACIONAL**  
**ESCUELA SUPERIOR DE INGENIERÍA QUÍMICA E INDUSTRIAS EXTRACTIVAS**  
**DEPARTAMENTO DE INGENIERÍA EN METALURGIA Y MATERIALES**

**“TWINNING ACTIVITY, MICROSTRUCTURE AND  
TEXTURE EVOLUTION IN HOT ROLLED MAGNESIUM  
SINGLE CRYSTALS”**

**T E S I S**

**QUE PARA OBTENER EL GRADO DE  
MAESTRO EN CIENCIAS EN INGENIERÍA METALÚRGICA**

**P R E S E N T A**

**ING. JOSÉ ANTONIO ESTRADA MARTÍNEZ**



**Director: DR. DAVID HERNÁNDEZ SILVA**

**CIUDAD DE MÉXICO**

**JUNIO 2019**



# INSTITUTO POLITÉCNICO NACIONAL

## SECRETARÍA DE INVESTIGACIÓN Y POSGRADO

### ACTA DE REVISIÓN DE TESIS

En la Ciudad de  siendo las  horas del día  del mes de  del

se reunieron los miembros de la Comisión Revisora de la Tesis, designada por el Colegio de Profesores de Posgrado de:

para examinar la tesis titulada:

por el (la) alumno (a):

Apellido Paterno:	ESTRADA	Apellido Materno:	MARTÍNEZ	Nombre (s):	JOSÉ ANTONIO
-------------------	---------	-------------------	----------	-------------	--------------




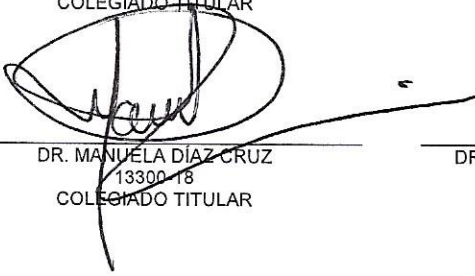

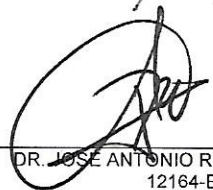
Número de registro:

Aspirante del Programa Académico de Posgrado:

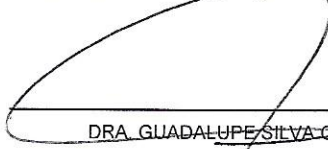
Después de la lectura y revisión individual, así como el análisis e intercambio de opiniones, los miembros de la Comisión manifestaron **APROBAR**  **NO APROBAR**  la tesis, en virtud de los motivos siguientes:

\_\_\_\_\_  
\_\_\_\_\_  
\_\_\_\_\_

#### Comisión Revisora de Tesis

 DR. DAVID HERNÁNDEZ SILVA DIRECTOR DE TESIS 12329-EI-16 COLEGIADO TITULAR	 DR. JOSÉ FEDERICO CHÁVEZ ALCALÁ 13673-EI-18/6 COLEGIADO TITULAR	 DR. CARLOS GÓMEZ YÁÑEZ 12174-EG-16 COLEGIADO TITULAR
 DR. MANUELA DÍAZ CRUZ 13300-18 COLEGIADO TITULAR	 DR. HÉCTOR JAVIER DORANTES ROSALES 12165-EI-16 COLEGIADO TITULAR	 DR. JOSÉ ANTONIO ROMERO SERRANO 12164-EI-16 COLEGIADO TITULAR

Presidente del Colegio de Profesores





DRA. GUADALUPE SILVA OLIVER ESCUELA SUPERIOR DE INGENIERÍA QUÍMICA E INDUSTRIAS EXTRACTIVAS SECCIÓN DE ESTUDIOS DE POSGRADO E INVESTIGACIÓN



**INSTITUTO POLITÉCNICO NACIONAL**  
**SECRETARÍA DE INVESTIGACIÓN Y POSGRADO**

**CARTA CESIÓN DE DERECHOS**

En la Ciudad de México, el día 18 del mes de Junio del año 2019, el que suscribe **José Antonio Estrada Martínez** alumno del Programa de Maestría en Ciencias en Ingeniería Metalúrgica, con número de registro **A170235**, adscrito a la **Sección de Estudios de Posgrado e Investigación de la ESIQIE**, manifiesta que es el autor intelectual del presente trabajo de Tesis bajo la dirección del **Dr. David Hernández Silva** y cede los derechos del trabajo titulado **“Twinning activity, microstructure and texture evolution in hot rolled magnesium single crystals”** al Instituto Politécnico Nacional para su difusión con fines académicos y de investigación.

Los usuarios de la información no deben reproducir el contenido textual, gráficas o datos del trabajo sin el permiso expreso del autor y/o director del trabajo. Este puede ser obtenido escribiendo a las siguientes direcciones **jaem.asm@gmail.com**, **dhs07670@yahoo.com**. Si el permiso se otorga, el usuario deberá dar el agradecimiento correspondiente y citar la fuente del mismo.

---

**Ing. José Antonio Estrada Martínez**  
Nombre y firma

*“I believe that we start to see our true personalities when we go through the most difficult moments. This is when we get stronger.”*

**AYRTON SENNA**

**A:**

Mis padres, Eusebia y Sergio

Mis hermanos; Sergio, Fabián, Edmundo y Julieta †

Mi novia Elizabeth

Mis amigos; Humberto, Samantha, Jessica, Nancy y Eduardo



# Acknowledgments



First, I would like to thank the Mexican people for generating all the resources that CONACY T grants to support public education institutions.



Second, I want to thank the Instituto Politécnico Nacional (IPN), to the Escuela Superior de Ingeniería Química e Industrias Extractivas (ESIQIE) and to the Departamento de Ingeniería en Metalurgia y Materiales (DIMM), for allowing me to complete my studies.

Third, I express my sincere thanks to Germany, to the Rheinisch-Westfälische Technische Hochschule Aachen (RWTH), to the Fakultät für Georessourcen und Materialtechnik (FGM) and to the Institut für Metallkunde und Metallphysik (IMM) for financing and allowing me to conduct this research at its facilities.



I would also like to express special thanks to my co-advisor, Dr. Ing. Talal Al-Samman, for the support and the opportunity he gave me to work with his teamwork at the IMM, his passion for his work and advice allowed me to realize that academic research would only be my starting point.



Thanks to the IMM staff, especially Nico, Saravana, Miriam, Sergej, Gerhard and Stefanie for all their support and for being good people with me, I will never forget you. To David and Marcel for making me a stronger person.

Also, I would like to thank my advisor Dr. David Hernández Silva, for his support and advice given, I learned too much from him not only as a professor, also as a person.



Finally, thanks to my labmates; Keff, Hugo, Cesar, Rodrigo and Aldo, for all the good times we had.





LIST OF FIGURES .....	V
LIST OF TABLES .....	VII
LIST OF ACRONYMS .....	VIII
ABSTRACT .....	IX
RESUMEN.....	XI
<b>1. INTRODUCTION.....</b>	<b>1</b>
<b>2. BACKGROUND.....</b>	<b>5</b>
2.1. DEFORMATION MECHANISMS IN HCP .....	6
2.1.1. Slip of $(a)$ type dislocations.....	6
2.1.2. Slip of $(c+a)$ type dislocations.....	8
2.1.3. Twinning. ....	9
2.2. SCHMID'S LAW.....	13
2.3. SINGLE CRYSTALS.....	14
2.3.2. Single Crystal Growth: Bridgman Technique.....	14
2.4. PROCESSING TECHNIQUES.....	15
2.4.2. Rolling.....	16
2.5. RECRYSTALLIZATION.....	17
2.6. STATE OF THE ART.....	19
<b>3. EXPERIMENTAL.....</b>	<b>25</b>
3.1. SINGLE CRYSTAL GROWTH .....	26
3.2. CRYSTAL ORIENTATION.....	28
3.3. HOT ROLLING .....	30
3.4. HEAT TREATMENT .....	31
3.5. CHARACTERIZATION .....	31
3.5.1. Sample Preparation .....	31
3.5.2. Optical Microscopy (OM) .....	33
3.5.3. X-Ray Diffraction (XRD).....	33
3.5.4. Electron Backscatter Diffraction (EBSD).....	34
<b>4. RESULTS.....</b>	<b>35</b>
4.5. MICROSTRUCTURE EVOLUTION DURING ROLLING PROCESS.....	37
4.6. TEXTURE EVOLUTION DURING HOT ROLLING.....	39
4.7. TWINNING ACTIVITY AND DRX DURING ROLLING.....	41
4.8. MICROSTRUCTURE POST ANNEALING TREATMENT.....	50



<b>5. DISCUSSION .....</b>	<b>53</b>
5.1. {1012} TWINNING AND ITS INFLUENCE ON THE BASAL TEXTURE.....	53
5.2. SHEAR LOCALIZATION ON {1011} TWINS AND THEIR INFLUENCE ON THE DRX BEHAVIOR. ....	56
5.3. DRX MECHANISMS DURING HOT ROLLING. ....	58
5.4. PREFERENTIAL GROWTH MECHANISM DURING POST ROLLING ANNEALING. ....	66
<b>CONCLUSIONS AND FUTURE RESEARCH.....</b>	<b>69</b>
6.2. CONCLUSIONS.....	69
6.2. FUTURE RESEARCH .....	70
APPENDIX A. CHEMICAL COMPOSITION OF MAGNESIUM USED FOR THE CRYSTAL GROWTH.....	71
APPENDIX B. LAUE PATTERNS OF MAGNESIUM SINGLE CRYSTALS.....	73
APPENDIX C. ROLLING SCHEDULE.....	75
APPENDIX D. COMPLEMENTARY POLE FIGURES .....	77
D.1. COMPLEMENTARY POLE FIGURES OF O-1 .....	77
D.2. COMPLEMENTARY POLE FIGURES OF O-2 .....	80
APPENDIX E. COMPLEMENTARY METALLOGRAPHIES .....	83
REFERENCES.....	85

# List of Figures

NUMBER	FIGURE	PAGE
FIG. 2.1.	SCHEMATIC REPRESENTATION OF HCP STRUCTURE.....	5
FIG. 2.2.	<A> SLIP SYSTEMS OF MAGNESIUM. ....	8
FIG. 2.3.	<A+C> SLIP SYSTEMS OF MAGNESIUM.....	9
FIG. 2.4.	SCHEMATIC REPRESENTATION OF TWINNING PHENOMENA. ....	10
FIG. 2.5.	THE VARIATION OF THE TWINNING SHEAR WITH THE C/A RATIO, FULL CIRCLES SHOW THE ACTIVE TWINNING SYSTEM. ....	10
FIG. 2.6.	TWINNING SYSTEMS OF MAGNESIUM.....	12
FIG. 2.7.	SCHEMATIC ILLUSTRATION OF PLASTIC DEFORMATION IN SINGLE CRYSTAL.....	13
FIG. 2.8.	SCHEMATIC REPRESENTATION OF A VERTICAL BRIDGMAN FURNACE. ....	15
FIG. 2.9.	HOT ROLLING PROCESS. ....	16
FIG. 2.10.	A) ACCUMULATION OF DISLOCATIONS AND LATTICE ROTATION AT A GRAIN BOUNDARY; B) REARRANGEMENT OF DISLOCATIONS INTO LOW ANGLE BOUNDARIES THROUGH DYNAMIC RECOVERY IN THE VICINITY OF THE ORIGINAL GRAIN BOUNDARY; C) FORMATION OF HIGH ANGLE BOUNDARIES THROUGH DYNAMIC RECOVERY IN THE VICINITY OF THE ORIGINAL GRAIN BOUNDARY; C) FORMATION OF HIGH ANGLE BOUNDARIES THROUGH A PROGRESSIVE INCREASE IN MISORIENTATION, I.E. NEW GRAINS EMERGE. ....	18
FIG. 3.1.	EXPERIMENTAL PROCEDURE DIAGRAM. ....	25
FIG. 3.2.	FANUC ROBOCUT A-01A EDM MACHINE. ....	26
FIG. 3.3.	A) STEEL CRUCIBLE, B) POLYCRYSTALLINE BLANK, C) CRYSTAL SEED .....	27
FIG. 3.4.	BRIDGMAN VERTICAL FURNACE FOR SINGLE CRYSTAL GROWTH.....	27
FIG. 3.5.	A) ENTIRE SINGLE CRYSTAL AFTER CLEANING, B) UPPER END, C) CONICAL SINGLE CRYSTAL, D) LOWER END (SEED). ....	28
FIG. 3.6.	CRYSTAL MOUNTED ON THE GONIOMETER. ....	28
FIG. 3.7.	LAUE CAMERA USED FOR CRYSTAL ORIENTATION BY X-RAY BACK DIFFRACTION .....	29
FIG. 3.8.	CRYSTAL ORIENTATION SCHEME OF ROLLING BLOCKS.....	30
FIG. 3.9.	A) THERMOCONCEPT FURNACE USED FOR HEATING, B) CARL WEZEL ROLLING MILL. ....	30
FIG. 3.10.	SCHEME OF THE SAMPLES CUT FROM THE SHEET (MM).....	31
FIG. 3.11.	ELECTROLYTIC CELL AND ELECTROLYTE USED FOR ELECTROPOLISHING. ....	32
FIG. 3.12.	ZEISS AXIOSCOP II MAT OPTICAL MICROSCOPE .....	33
FIG. 3.13.	BRUKER D8 ADVANCE DIFFRACTOMETER USED FOR GLOBAL TEXTURE MEASUREMENTS. ....	34
FIG. 3.14.	JEOL JSM-6701F SCANNING ELECTRON MICROSCOPE EQUIPPED WITH HKL-NORDLYS II EBSD DETECTOR.....	34
FIG. 4.1.	PICTURES OF MAGNESIUM HOT ROLLED SHEETS OF ORIENTATION 1 AND ORIENTATION 2 AT $\epsilon = 30, 50$ AND 80% A) RD-TD PLANE, B) RD-ND PLANE. ....	36
FIG. 4.2.	OPTICAL MICROGRAPHS OF THE RD-TD PLANE AFTER ROLLING AT DIFFERENT STRAINS. ....	38
FIG. 4.3.	INVERSE POLE FIGURES OF MAGNESIUM SHEETS AT DIFFERENT STRAINS FOR BOTH ORIENTATIONS. ....	40
FIG. 4.4.	EBSD RESULTS OBTAINED FROM AN O-1'S SPECIMEN AT STRAIN OF 30% A) EBSD MAP IN INVERSE POLE FIGURE (IPF) COLORING RELATIVE TO ND, B) CORRESPONDING IPF'S. C) CORRESPONDING SCATTERED DATA ND IPF, D) BOUNDARY MISORIENTATION MAP, E) CORRESPONDING MISORIENTATION ANGLE DISTRIBUTION.....	42
FIG. 4.5.	EBSD RESULTS OBTAINED FROM AN O-2'S SPECIMEN AT STRAIN OF 30% A) EBSD MAP IN INVERSE POLE FIGURE (IPF) COLORING RELATIVE TO ND, B) CORRESPONDING IPF'S. C) CORRESPONDING SCATTERED DATA ND IPF, D) BOUNDARY MISORIENTATION MAP, E) CORRESPONDING MISORIENTATION ANGLE DISTRIBUTION.....	44
FIG. 4.6.	EBSD RESULTS OBTAINED FROM AN O-1'S SPECIMEN AT STRAIN OF 50% A) EBSD MAP IN INVERSE POLE FIGURE (IPF) COLORING RELATIVE TO ND, B) CORRESPONDING IPF'S. C) CORRESPONDING SCATTERED DATA ND IPF, D) BOUNDARY MISORIENTATION MAP, E) CORRESPONDING MISORIENTATION ANGLE DISTRIBUTION.....	46
FIG. 4.7.	EBSD RESULTS OBTAINED FROM AN O-2'S SPECIMEN AT STRAIN OF 50% A) EBSD MAP IN INVERSE POLE FIGURE (IPF) COLORING RELATIVE TO ND, B) CORRESPONDING IPF'S. C) CORRESPONDING SCATTERED DATA ND IPF, D) BOUNDARY MISORIENTATION MAP, E) CORRESPONDING MISORIENTATION ANGLE DISTRIBUTION.....	47

FIG. 4.8.	EBSD RESULTS OBTAINED FROM AN O-1'S SPECIMEN AT STRAIN OF 80% A) EBSD MAP IN INVERSE POLE FIGURE (IPF) COLORING RELATIVE TO ND, B) CORRESPONDING IPF'S. C) CORRESPONDING SCATTERED DATA ND IPF. ....	49
FIG. 4.9.	EBSD RESULTS OBTAINED FROM AN O-2'S SPECIMEN AT STRAIN OF 80% A) EBSD MAP IN INVERSE POLE FIGURE (IPF) COLORING RELATIVE TO ND, B) CORRESPONDING IPF'S. C) CORRESPONDING SCATTERED DATA ND IPF. ....	50
FIG. 4.10.	O-1 AND O-2 MICROSTRUCTURES AFTER ANNEALING AT 400°C. ....	51
FIG. 4.11.	EBSD RESULTS OBTAINED FROM AN O-1'S SPECIMEN AFTER ANNEALING TREATMENT A) EBSD MAP IN INVERSE POLE FIGURE (IPF) COLORING RELATIVE TO ND, B) CORRESPONDING IPF'S. C) CORRESPONDING SCATTERED DATA ND IPF. ....	52
FIG. 4.12.	EBSD RESULTS OBTAINED FROM AN O-2'S SPECIMEN AFTER ANNEALING TREATMENT A) EBSD MAP IN INVERSE POLE FIGURE (IPF) COLORING RELATIVE TO ND, B) CORRESPONDING IPF'S. C) CORRESPONDING SCATTERED DATA ND IPF. ....	55
FIG. 5.1.	(0002) PF SHOWING THE INITIAL ORIENTATIONS A) O-1 AND B) O-2 AS WELL AS THEIR CORRESPONDING 1012 EXTENSION TWIN VARIANTS. SCHEMATIC REPRESENTATION OF ACTIVE TWIN VARIANTS FOR A) O-1 AND B) O-2. RECALCULATED (0002) PF AT $\epsilon=30\%$ FOR E) O-1 AND F) O-2. ....	57
FIG. 5.2.	ORIENTATION MAPS IN ND IPF COLORING SHOWS DRXED TWIN BANDS DUE STRAIN LOCALIZED INSIDE CT'S. FOR O-1 A) $\epsilon = 30\%$ , B) $\epsilon = 50\%$ AND O-2, C) $\epsilon = 30\%$ , D) $\epsilon = 50\%$ . ....	59
FIG. 5.3.	EBSD ANALYSIS AT $\epsilon = 30\%$ : EBSD MAP IN ND IPF COLORING AND CORRESPONDING MISORIENTATION LINE PROFILES ALONG THE BLACK ARROWS FOR A) O-1 AND B) O-2. ....	62
FIG. 5.4.	EBSD ANALYSIS AT $\epsilon = 50\%$ : EBSD MAP IN ND IPF COLORING AND CORRESPONDING MISORIENTATION LINE PROFILES ALONG THE BLACK ARROWS FOR A) O-1 AND B) O-2. ....	64
FIG. 5.5.	EBSD ANALYSIS AT $\epsilon=80\%$ : EBSD MAP IN ND IPF COLORING AND CORRESPONDING MISORIENTATION LINE PROFILES ALONG THE BLACK ARROWS AS WELL AS GRAIN MISORIENTATION PROFILE FOR A) O-1 AND B) O-2. ....	66
FIG. 5.6.	EBSD ANALYSIS AT $\epsilon=80\%$ : EBSD MAP IN ND IPF COLORING AND CORRESPONDING MISORIENTATION LINE PROFILES ALONG THE BLACK ARROWS AS WELL AS GRAIN MISORIENTATION PROFILE FOR A) O-1 AND B) O-2. ....	65
FIG. 5.7.	BOUNDARY MISORIENTATION MAPS AND CORRESPONDING MISORIENTATION ANGLE DISTRIBUTION OF A) O-1 AND B) O-2. ....	67
FIG. B.1.	(0002) LAUE PATTERNS OF A) O-1 AND B) O-2. ....	73
FIG. D.1.	POLE FIGURES OF O-1 AT $\epsilon = 30\%$ ....	79
FIG. D.2.	POLE FIGURES OF O-1 AT $\epsilon = 50\%$ ....	80
FIG. D.3.	POLE FIGURES OF O-1 AT $\epsilon = 80\%$ ....	81
FIG. D.4.	POLE FIGURES OF O-2 AT $\epsilon = 30\%$ ....	80
FIG. D.5.	POLE FIGURES OF O-2 AT $\epsilon = 30\%$ ....	81
FIG. D.6.	POLE FIGURES OF O-2 AT $\epsilon = 30\%$ ....	82
FIG. E.1.	METALLOGRAPHY USED FOR GRAIN SIZE MEASUREMENTS OF ORIENTATION 1. ....	83
FIG. E.2.	METALLOGRAPHY USED FOR GRAIN SIZE MEASUREMENTS OF ORIENTATION 2. ....	84

## *List of Tables*

NUMBER	TABLE	PAGE
TABLE 2.1.	CRYSTALLOGRAPHIC ELEMENTS AND MISORIENTATION (ANGLE/AXIS PAIR) FOR COMMONLY OBSERVED AND PREDICTED DEFORMATION TWIN MODES IN Mg AND Mg ALLOYS.....	12
TABLE 4.1.	DIMENSIONS OF THE OBTAINED SHEETS FOR BOTH ORIENTATIONS. ....	35
TABLE A.1.	CHEMICAL COMPOSITION (WT.%) OF THE INITIAL PURE Mg MATERIAL USED FOR CRYSTAL GROWTH (OBTAINED BY SPARK OPTICAL EMISSION SPECTROSCOPY).....	71
TABLE A.2	CHEMICAL COMPOSITION (WT.%) OF A GROWN PURE Mg SINGLE CRYSTAL (OBTAINED BY SPARK OPTICAL EMISSION SPECTROSCOPY). ....	71
TABLE C.1.	ROLLING SCHEDULE .....	73

## *List of Acronyms*

GB	grain boundary
CD	compression direction
CDRX	continuous dynamic recrystallization
CRSS	critical resolved shear stress
CT	contraction twin
DDRX	discontinuous dynamic recrystallization
DRX	dynamic recrystallization
EBSD	electron backscatter diffraction
EDM	electrical discharge machining
hcp	hexagonal close packed
IPF	inverse pole figure
LD	longitudinal direction
MRD	multiples of a random distribution
ND	normal direction
O-1	orientation 1
O-2	orientation 2
ODF	orientation density function
PET	primary extension twin
PF	pole figure
PSC	plane strain compression
RSS	resolved shear stress
RT	room temperature
SEM	scanning electron microscope
SET	secondary extension twin
SF	Schmid factor
TB	twin band
TD	transverse direction
TET	tertiary extension twin

# Abstract

**M**agnesium and its alloys are becoming increasingly used in the automotive industry to achieve lighter units due to their low densities and high specific strengths. These potential applications motivate great efforts to improve the processing methods which requires an extensive knowledge about the deformation mechanisms involved. A good option to achieve this is to start with a simple microstructure material such as single crystals to isolate and identify the mechanisms of deformation depending on the initial orientation of the crystal. Therefore, in this work magnesium single crystals were subjected to hot rolling at 450°C in two specific orientations. For orientation 1 the  $[11\bar{2}0]$  direction was parallel to the normal direction of the sheet plane (ND), while for orientation 2 it was  $[10\bar{1}0]$  direction. The microstructure and texture evolution were characterized with respect to the deformation and recrystallization mechanisms.

The deformation was dominated by  $\{10\bar{1}2\}$  twinning at the first rolling steps, which rotated 86° the original crystal and formed a new matrix of grains with basal plane almost parallel to the sheet plane (basal texture). In the orientation 1 several grains with particular orientations were observed, it is believed that they were generated by primary, secondary and tertiary extension twinning. Contraction twins were observed in the basal matrix at strain ( $\varepsilon$ ) of 30% and 50%. At  $\varepsilon = 80\%$  the deformation was accommodated without twinning. The contraction twins lead to twin-induced continuous dynamic recrystallization (CDRX) and formed dynamic recrystallized (DRXed) twin bands giving rise to grains with its c-axis 30° rotated from its parent grain.

Discontinuous dynamic recrystallization (DDRX) was observed at  $\varepsilon = 30\%$  for both orientations, fine grains and sub-grains-boundaries formed at the triple junctions of the grains. Instead, CDRX were observed at all strains by the transition of low angle grain boundaries (LAGBs) to high angle grain boundaries (HAGBs) within the grains of basal texture and the grains inside the twin bands.

After annealing, grain growth was observed in both orientations. An evident transition sequence of movement of grain boundaries was observed, high angle grain boundaries ( $>15^\circ$ ) converted to low angle grain boundaries ( $5-15^\circ$ ) that turned to very low angle grain boundaries (VLAGB, $2-5^\circ$ ), which tend to disappear. The grains with the c-axis most parallel to the normal sheet (ND) grew preferentially (coarsening) during annealing, strengthening the basal texture.



# Resumen

**E**l magnesio y sus aleaciones son usados cada vez más en la industria automotriz para la construcción de unidades más ligeras debido a sus baja densidad y alta resistencia específica. Estas potenciales aplicaciones han motivado grandes esfuerzos para mejorar los métodos de su procesamiento, lo cual requiere un amplio conocimiento sobre los mecanismos de deformación involucrados. Una buena opción para lograr esto es comenzar con un material de microestructura simple, tal es el caso de los monocristales que permiten aislar e identificar los mecanismos de deformación dependiendo de la orientación inicial del cristal. Por lo anterior, en este trabajo, monocristales de magnesio fueron laminados en caliente a 450°C en dos orientaciones específicas. Para la orientación 1, la dirección  $[11\bar{2}0]$  fue paralela a la dirección normal del plano de laminación (ND), mientras que para la orientación 2 esta dirección fue la  $[10\bar{1}0]$ . La evolución de la microestructura y textura fue caracterizada con respecto a los mecanismos de deformación y recristalización.

En los primeros pasos de laminación, la deformación fue dominada por maclado  $\{10\bar{1}2\}$ , el cual rotó 86° el monocristal original y formó una nueva matriz de granos con el plano basal casi paralelo al plano de la laminación (textura basal). En la orientación 1 se observaron varios granos con orientaciones particulares que se cree que fueron generados por maclado primario, secundario y terciario. A una deformación ( $\epsilon$ ) de 30% y 50% se observaron maclas de contracción en la matriz basal mientras que a  $\epsilon = 80\%$  la deformación se acomodó sin maclado. Las maclas de contracción condujeron a la recristalización dinámica continua (CDRX) y formaron bandas de macla recristalizadas que dieron origen a granos con su eje c rotado 30° con respecto al de su grano original (macla).

A  $\epsilon = 30\%$  se observó recristalización dinámica discontinua (DDRX) para ambas orientaciones, además de granos finos y subgranos formados en los puntos triples de la microestructura. En cambio, se observó CDRX durante todos los estados de deformación mediante la transición de límites de grano de ángulo bajo (LAGB) a límites de grano de ángulo alto (HAGB) dentro de los granos con orientación basal y los granos dentro de las bandas de maclado.

Después del recocido, se observó crecimiento de grano en ambas orientaciones. Se estableció una secuencia de transición evidente del movimiento de los límites de grano, los límites de grano de ángulo alto ( $> 15^\circ$ ) se convirtieron en límites de grano de ángulo bajo ( $5-15^\circ$ ) que se convirtieron en límites de grano de ángulo muy bajo (VLGB,  $2-5^\circ$ ), estos últimos tienden a desaparecer. Los granos con el eje c más paralelo a la lámina normal (ND) crecieron preferentemente (engrosándose) durante el recocido, fortaleciendo la textura basal.





# *Introduction*

**E**very great story has a beginning, this one started with a challenge, to build the fastest car in the world and the **magnesium** made it possible in 1921 when Tommy Milton won the Indianapolis 500, the biggest auto race in United States, with a Frontenac car featuring magnesium pistons, but as already mentioned, this was just the beginning. [1]

In 1938 the VW Beetle was the commercial car with the largest application of magnesium alloys in its air-cooled engine and transmission with a total weight of 17 kg. In 1940 Boeing used magnesium in the Wright R-3350 aviation engine of the B-29 bomber. In 1971 Porsche used ZE41A magnesium alloy in the engine, gearbox, suspension and frame in the 917K that won Le Mans that year. In 1990 Mercedes Benz used an AM20 and AM50 magnesium alloys die castings in a three-point safety belt for the SL Roadster seat structure. In 1997 the WE43AT6 magnesium alloy was used in the main transmission of the Boeing MD600 helicopter drive system. In 2010 the Jaguar XJ model used a one-piece die cast front-end carrier to replace a welded assembly of 13 aluminum components [2-7].

It can be noted that magnesium is used mainly for automotive and aerospace applications, because it is the lightest structural metal, i.e., the lighter piston would require less power to operate, and the engine would go faster. In addition, the use of lighter materials leads to an improvement in fuel efficiency and thus reduce the emission of gases and environmental impact [8-11].

However, magnesium alloys have some limitations such as high mechanical anisotropy and low formability at room temperature, owing to its hexagonal close packed (hcp) structure with limited number of slip modes, it only has three easily activate slip systems [12]. This results in strong anisotropy in the material giving rise to a strong ‘basal texture’ with grain orientations having basal planes parallel to the sheet plane. This type of texture has often been seen to be unaffected by any annealing treatment [13,14]. Regarding to deformation mechanisms, the activation of the basal slip system,  $(0001) \langle 11\bar{2}0 \rangle$ , occurs during deformation at room temperature because it has the lowest values of critical resolved shear stress (CRSS) [15]. The second lowest value of CRSS reported is for the tensile twinning,  $\{10\bar{1}2\} \langle 10\bar{1}1 \rangle$ , the other active deformation mechanism at room temperature but it causes a strong yield asymmetry [16, 17]. In the case of the prismatic  $\{10\bar{1}0\}$  and pyramidal  $\{10\bar{1}1\}$  slip systems, the CRSSs value decrease as the temperature increases, so it can be predicted that the CRSSs values for the non-basal slip systems will be thermally activated above  $230^\circ\text{C}$  [18]. Because of that, the forming of magnesium must be performed at elevated temperature by thermomechanical treatments (i.e., rolling, extrusion, forging, etc.). In addition, magnesium sheets have a poor formability at room temperature, which is improved above  $175^\circ\text{C}$  [19]. During thermomechanical treatments grains rotate and acquired a strong texture, which is unfavorable for further processing steps that must also be carried out at elevated temperatures to thermal activation of additional slip systems, leading to high production costs [20].

In recent years, magnesium alloys gained substantial momentum due to the pursuit toward achieving lightweight constructions in automotive engineering, which has spurred academic and industrial research to identify more efficient manufacturing ways. In magnesium alloys, plastic anisotropy is greatly pronounced, i.e. grains of varying orientations are expected to exhibit different mechanical response. Compared to polycrystal investigations, studies on single crystals claim several advantages. Performing experiments on specially oriented single crystals with respect to the loading axes allows to isolate and identify the mechanisms of deformation depending on the initial orientation of the crystal, since the operating deformation modes can be determined using the Schmid’s law. Single crystal studies aim at exposing the underlying physical mechanisms, rather than claiming to directly predict the deformation behavior of polycrystals. However, despite the presence of grain boundaries and grain orientation spread the plastic deformation in *textured* materials is similar to that in single crystals. The analogy between single crystals and polycrystalline material with strong texture was studied by Kelley [21] and Graff [22].

A lot of research effort was dedicated to uncover the operating modes of deformation in magnesium. Well-known studies on magnesium single crystals were performed by Wonziewicz and Backofen [23] as well as by Kelly and Hosford [24] in the 1960s. Both studies included plane strain compression tests (PSC) on differently oriented magnesium single crystals, demonstrating their complex deformation behavior, which is characterized by profuse deformation twinning and the occurrence of recrystallization. However, the investigations mentioned above were limited to rather small strains as their focus was on the temperature dependence of slip and twinning activation.

More recently, Molodov [25-31] characterized the deformation behavior and microstructure evolution of Mg single crystals with the same orientations proposed for this work but on PSC, using advanced characterization techniques as Electron Backscatter Diffraction (EBSD) and focusing on the dynamic recrystallization (DRX) mechanisms and the influence of twinning on the texture evolution. However, it is mandatory to reveal the deformation behavior of magnesium under strain patterns of real forming process such as rolling, which allows the broadening of the sample, contrary to PSC where this phenomenon it is disabled by the walls of the channel die. Therefore, the aim of this master thesis is to provide an overview of the plastic response and establishing a basic understanding of the deformation and recrystallization mechanisms involved in hot rolled magnesium single crystals at 450°C. It is worth noting that although single crystals were used for these studies, owing to the occurrence of deformation twinning and DRX process, the initial single crystal was turned into a polycrystal since early strains, thus, the mechanisms reported are directly relevant for a magnesium polycrystalline material. That said, in the case of magnesium, very strong basal textures are predominant, hence individual grains often undergo a similar deformation as compared to what is observed in the current studies.



# Background

The atoms in magnesium are arranged in hexagonal close-packed structure (HCP) (Fig. 2.1). It has two lattice parameters,  $a$  and  $c$ . It is characterized by the six-fold symmetry along the  $c$ -axis and three equivalent directions  $a_1$ ,  $a_2$  and  $a_3$  that make up an angle of  $120^\circ$  and are perpendicular to the  $c$ -axis. For magnesium the  $c/a=1.623$  ratio is very close to the ideal theoretical value  $\sqrt{8/3} \cong 1.633$ . The deformation behavior of materials with the HCP structure are significantly influenced by the  $c/a$  ratio [32], topic that will be addressed in the next section.

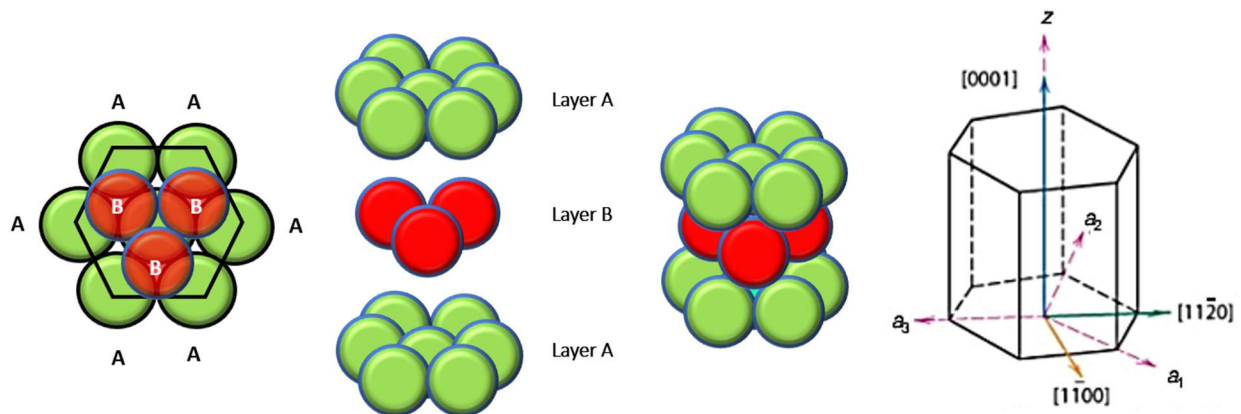


Fig. 2.1. Schematic representation of HCP structure.

### 2.1. DEFORMATION MECHANISMS IN HCP

The main deformation mechanisms in HCP metals are dislocation slip and deformation twinning.

#### 2.1.1. SLIP OF $\langle a \rangle$ TYPE DISLOCATIONS

The slip is realized by movement of dislocations. The magnitude and direction of slip are represented by the Burgers vector  $\vec{b}$ . To initiate the slip, the component of shear stress, resolved in a particular slip direction, which is independent of the crystal orientation, must overcome the critical value – critical resolved shear stress (CRSS). Generally, the slip system with the lowest CRSS is on the close-packed plane and in close-packed direction, however, other slip systems can be activated as well. The value of CRSS for the slip system depends also on temperature and alloying content [33, 34].

The effect of  $c/a$  ratio on the dislocation activity is significant. In an ideal case, when  $c/a = \sqrt{8/3}$ , the HCP structure has one close packed plane family, it is basal plane (0001) with three close-packed  $\langle a \rangle$  directions ( $\langle 11\bar{2}0 \rangle$ ). For materials with  $c/a$  higher than ideal value (Zn, Cd), basal slip is the most easily activated deformation system. For materials with  $c/a$  lower than ideal value (Ti, Zr, Be), the most easily activated slip is on the prismatic  $\{10\bar{1}0\}$  and pyramidal  $\{10\bar{1}1\}$  plane in the  $\langle a \rangle$  direction. For those close to the ideal value (Mg, Co, Cr) the main slip system is basal, but it can be partly substituted by pyramidal or prismatic slip [32].

The dominant deformation mechanism in magnesium is slip on the basal plane (0001) in a close packed  $\langle 11\bar{2}0 \rangle$  direction, as was established by Schiebold and Siebel [35] and Schmid [36]. Dislocations gliding in the basal plane have the smallest possible perfect Burgers vector  $\vec{b} = 1/3 \langle 11\bar{2}0 \rangle$  and dissociate in the basal plane, giving rise to intrinsic Shockley-type  $I_2$  stacking faults [37]. Basal slip operates readily at room temperature, being characterized by a very low critical resolved shear stress (CRSS) of 0.5 - 1.5 MPa [36, 38-48] and provides two independent slip systems.

For single basal slip, i.e. when a single slip system is activated, the resulting shear is accompanied by a lattice rotation around a  $\langle 10\bar{1}0 \rangle$  direction. When two different crystallographic  $\langle 11\bar{2}0 \rangle$  slip directions are equally favored (due to their geometric alignment with respect to the applied stress), the crystal deforms by coplanar double basal slip. In this case the lattice orientation change depends on the slip activity in each system. In any case, under compressive loading, the orientation change due to basal slip is such that the *c*-axis is rotated towards the compression direction rendering basal slip geometrically less favorable. This rotation of the *c*-axis towards the compression direction is the origin of the 'hard' basal texture in rolled polycrystalline magnesium sheets that is associated with a poor ductility.

Besides basal slip, prismatic slip, i.e. the glide of  $\langle a \rangle$  type dislocations on  $\{10\bar{1}0\}$  planes along  $\langle 11\bar{2}0 \rangle$  directions, is also possible in pure magnesium, albeit observed only at elevated temperature (above 180 °C) to contribute to deformation on a larger scale without being accompanied by twinning [49].

When prismatic slip is activated, the resulting lattice spin (as long as the stable orientation is not reached) yields an orientation change such that the crystal is rotated around the *c*-axis, i.e. prismatic slip has no effect on the alignment of the *c*-axis with respect to the load axis and is not able to prevent the formation of a 'hard' basal texture component.

All above listed systems have their Burgers vector in  $\langle a \rangle$  direction. Basal and prismatic slip together provide only 4 independent slip systems. The slip of  $\langle a \rangle$  type dislocations, i.e. along a  $\langle 11\bar{2}0 \rangle$  direction, has also been reported to occur at elevated temperatures (above 225 °C) on the first-type first-order  $\{10\bar{1}1\}$  and first-type second-order  $\{10\bar{1}2\}$  pyramidal planes [36, 50-52], providing four independent slip systems. However, these four slip systems are equivalent to the combination of basal and prismatic slip, still lacking a fifth system to enable an arbitrary shape change, i.e., their combination does not fulfill the criterion of five independent slip systems necessary for homogeneous plastic deformation according to Von Mises [53] and Taylor [54].



*$\langle a \rangle$  Slip Systems*

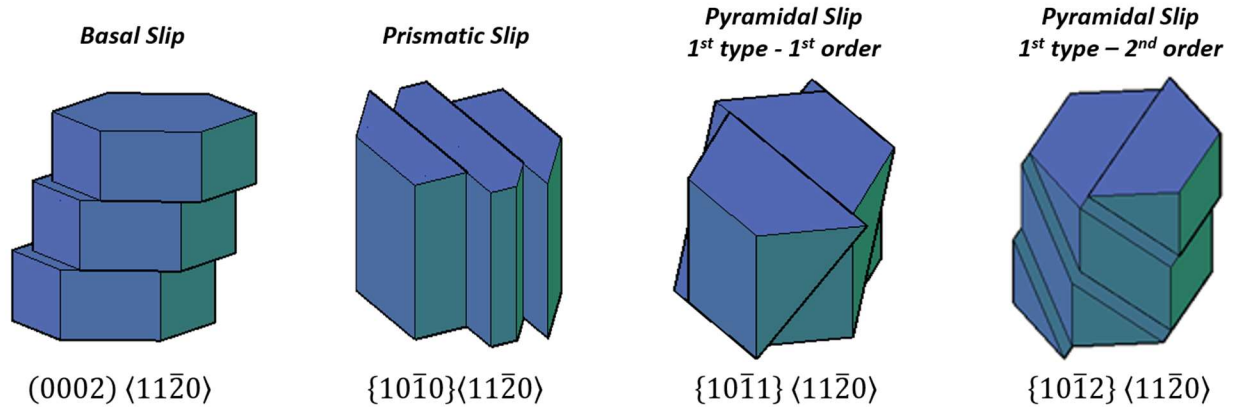


Fig. 2.2.  $\langle a \rangle$  Slip systems of Magnesium.

**2.1.2. SLIP OF  $\langle c+a \rangle$  TYPE DISLOCATIONS**

The slip in  $\langle c + a \rangle$  direction on 2<sup>nd</sup> order pyramidal plane fulfills the von Mises criterion, but the CRSS for its activation at room temperature is much higher than for  $\langle a \rangle$  slip [55]. It can be explained by relative large  $b \rightarrow$  in comparison to the lattice parameters.

In order to accommodate deformation along the  $c$ -axis by crystallographic slip, the glide of dislocations with a non-basal  $\langle c+a \rangle$  type Burgers vector is required. The operation of a deformation mode such as pyramidal  $\langle c+a \rangle$  slip, that alone provides five independent slip systems, further reduces incompatibility stresses as well as the plastic anisotropy and propensity to fracture. To this end, pyramidal  $\langle c+a \rangle$  slip can be understood to considerably improve ductility. Thus, it is widely recognized that the ductility of magnesium polycrystals at elevated temperature, i.e. the brittle-to-ductile transition at about 200 °C [36, 56] depends strongly on the activation of pyramidal  $\langle c+a \rangle$  slip in order to accommodate the  $c$ -axis contraction, especially taking into account the prevalence of sharp basal textures in magnesium sheets.

The slip of dislocations with the Burgers vector  $b = 1/3 \langle 11\bar{2}3 \rangle$  on  $\{11\bar{2}2\}$  planes was established to operate in Mg single crystals deformed by  $c$ -axis compression in a wide temperature range (RT-500 °C) [57], despite the very large Burgers vector. Pyramidal  $\langle c+a \rangle$  slip was also investigated by Stohr and Poirier [58], who reported an anomalous temperature dependence of the CRSS and proposed a thermally activated blocking of  $1/3 \langle 11\bar{2}3 \rangle$  edge dislocations.

In contrast to the original study by Obara et al. [57] where  $\langle c+a \rangle$  slip on second-order  $\{11\bar{2}2\}$  pyramidal planes (pyramidal-II) was identified, a recent investigation by Kelvin et al. [59] showed that first-order (pyramidal-I) slip, i.e.  $\{10\bar{1}1\}\{11\bar{2}3\}$ , is presumably the more dominant slip system in  $c$ -axis compression at room temperature with a CRSS of 54 MPa.

**$\langle c + a \rangle$  Slip Systems**

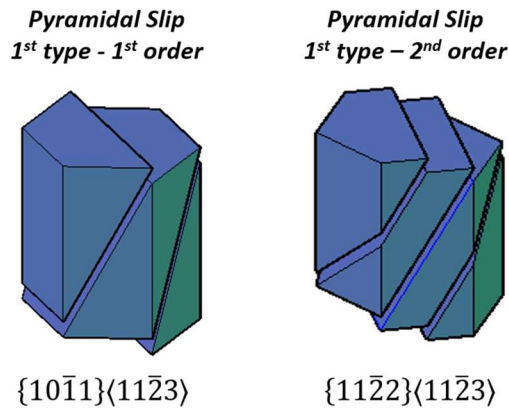


Fig. 2.3.  $\langle a+c \rangle$  slip systems of magnesium

**2.1.3. TWINNING.**

A deformation twin is a region of a crystalline body that was subjected to a homogeneous deformation (shape change) such that the resulting crystal structure remains the same but the crystal orientation differs from the parent structure, by a mirror reflection in defined plane or by the rotation around defined axis [60], i.e. the original lattice, called parent, and the twinned lattice have same structure but different orientation. The twinned volume is separated from the surrounding matrix by interfaces that are referred to as twin boundaries, i.e. grain boundaries satisfying a specific crystallographic relationship.

Each deformation twin mode can be described by four invariants. The invariant plane of the shear is called the twinning plane and marked as  $K_1$  and the shear direction is  $\eta_1$ .  $K_1$  is also the plane of mirror symmetry. Second undistorted plane is called conjugate plane and marked as  $K_2$ . Shear plane  $S$  is perpendicular to the planes  $K_1$  and  $K_2$  and contains the direction  $\eta_1$ . In Fig. 2.4 it is the plane of the paper. After deformation the plane  $K_2$  is rotated to the plane  $K_2'$  which forms the same angle  $\theta$  with the plane  $K_1$ . During the homogeneous shearing action atoms are translated parallel to the twinning plane in the twinning direction ( $\eta_1$ ), which implies highly coordinated atom displacements.

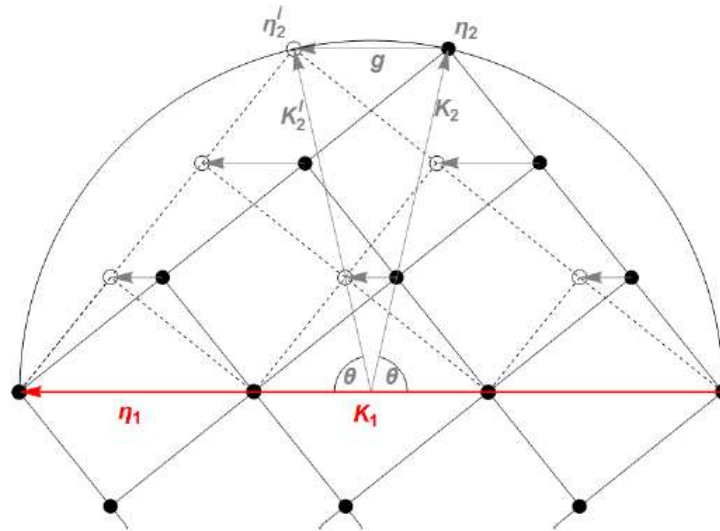


Fig. 2.4. Schematic representation of twinning phenomena.

The shear magnitude can be calculated as  $g=2\cot\theta$ . The twinning shear  $g$  as a function of  $c/a$  ( $\gamma$ ) is depicted in Fig. 2.5. The polar character of twinning causes that application of the shear stress in the opposite direction  $-\eta_1$  does not produce twins. Hence, twinning modes can be divided into two groups: twin modes causing the contraction along the parent  $c$ -axis are called compression twins; twin modes causing the elongation along the parent  $c$ -axis are called extension twins. The character of the twins can be seen from Fig. 2.5, where tensile twins have negative slope and compression twins have positive slope [61].

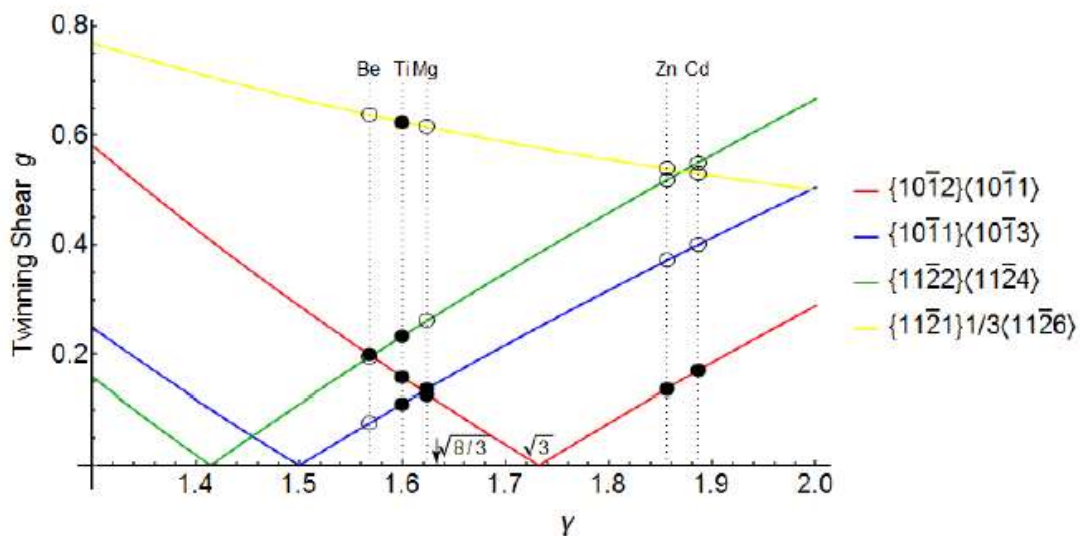


Fig. 2.5. The variation of the twinning shear with the  $c/a$  ratio, full circles show the active twinning system.

The key difference between crystallographic slip and deformation twinning is that the twinning (shear) direction is polar, as implied by Schmid and Wassermann [62], i.e. the shear in twinning can occur to one side only [63] (and not in the opposite shear direction).

Process of twinning can be separated into 3 parts: twin nucleation, propagation and thickening. Twin nucleation is driven by a local stress state and appears when the projection of applied stress to the  $\eta_1$  direction reaches its critical value [64]. During the propagation the twin grows rapidly in the  $\eta_1$  direction. Twin thickening is driven by long-range stress states across grains through the motion of twin boundaries in the normal direction to the twinning plane. The velocity of the thickening is by several orders lower than it is for the propagation [65].

All studies agree that CRSS for twinning is between the CRSS for basal and prismatic slip: It is estimated as 2–12 MPa and the dependence on grain size is much stronger than in the case of dislocation slip [66]. Common methods for twin observation are optical and electron microscopy. The electron back-scatter diffraction (EBSD) is a powerful method for the study of twinning, as it shows the particular orientation of grains and twins.

In magnesium, the major twinning system is  $\{10\bar{1}2\}\{10\bar{1}1\}$  extension twinning, associated with extension along the  $c$ -axis and reorientation of the lattice by  $86.3^\circ$  [67]. Other twinning systems like  $\{10\bar{1}1\}\{10\bar{1}2\}$  contraction twinning, that reorient the lattice by  $56.15^\circ$ , and  $\{10\bar{1}3\}\{30\bar{3}2\}$  contraction twinning, that reorient the lattice by  $64.0^\circ$ , or  $\{10\bar{1}2\} - \{10\bar{1}1\}$  double twinning has been also reported, however, they are minor deformation mechanisms [68].

Deformation twins with the  $\{10\bar{1}2\}$  plane, established to operate in Be, Mg, Zn and Cd by Mathewson and Phillips [69] are known to be profuse in magnesium [70]. By contrast,  $\{10\bar{1}1\}$  contraction twins were first reported by Schiebold and Siebel [35] in magnesium typically appear as narrow lamellae and are much harder to activate. Being less common than the  $\{10\bar{1}2\}$  extension twins,  $\{10\bar{1}1\}$  contraction twins in polycrystalline magnesium usually do not produce much texture change during deformation due to their low volume fraction.

Table 2.1. Crystallographic elements and misorientation (angle/axis pair) for commonly observed and predicted deformation twin modes in Mg and Mg alloys.

Twinning plane ( $K_1$ )	Shear direction ( $\eta_1$ )	Conjugate plane ( $K_2$ )	Conjugate direction ( $\eta_2$ )	Amount of shear $s$	Tilt angle $\theta_k$ ( $^\circ$ )	Tilt axis
$\{10\bar{1}2\}$	$\langle\bar{1}011\rangle$	$\{\bar{1}012\}$	$\langle10\bar{1}1\rangle$	0.1294	86.3	$\langle\bar{1}2\bar{1}0\rangle$
$\{10\bar{1}1\}$	$\langle10\bar{1}2\rangle$	$\{10\bar{1}3\}$	$\langle30\bar{3}2\rangle$	0.1373	56.15	$\langle\bar{1}2\bar{1}0\rangle$
$\{10\bar{1}3\}$	$\langle30\bar{3}2\rangle$	$\{10\bar{1}1\}$	$\langle10\bar{1}2\rangle$	0.1373	64.0	$\langle\bar{1}2\bar{1}0\rangle$
$\{11\bar{2}1\}$	$\langle\bar{1}\bar{1}26\rangle$	$\{0001\}$	$\langle11\bar{2}0\rangle$	0.6159	34.23	$\langle\bar{1}100\rangle$
$\{11\bar{2}4\}$	$\langle22\bar{4}3\rangle$	$\{11\bar{2}2\}$	$\langle11\bar{2}3\rangle$	0.2612	78.14	$\langle\bar{1}100\rangle$

The  $\{10\bar{1}3\}\langle30\bar{3}2\rangle$  twinning mode is a conjugate or reciprocal mode of  $\{10\bar{1}1\}$  twinning, as reported by Reed-Hill [71] in the case of magnesium, i.e.  $K_1$  and  $K_2$  as well as  $\eta_1$  and  $\eta_2$  are interchanged, whereas the amount of shear  $s$  remains identical. Though  $\{10\bar{1}3\}$  twins are considered to be reciprocal twins to  $\{10\bar{1}1\}$ , the former are not extension twins in magnesium, as is often assumed erroneously, but produce contraction along the  $c$ -axis, very much like  $\{10\bar{1}1\}$  twins. The Though  $\{10\bar{1}3\}$  twins were observed experimentally by Reed-Hill in uniaxial tension normal to the  $c$ -axis and by Yoshinaga et al. [72] in  $c$ -axis compression of magnesium single crystals.

### Twinning Systems

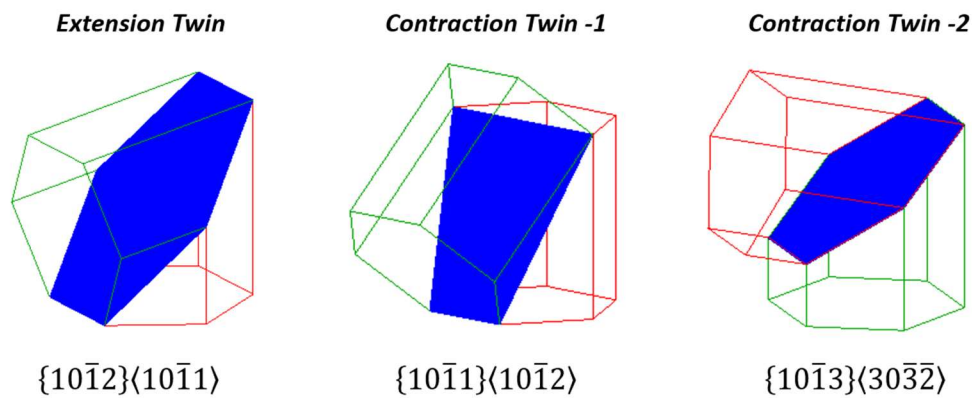


Fig. 2.6. Twinning systems of magnesium.

## 2.2. SCHMID'S LAW.

The probability of the activation of particular slip system strongly depends on the mutual orientation of the loading direction, slip plane and slip direction and CRSS  $\tau$ . The orientation dependence is characterized by the Schmid factor ( $SF$ ) –  $m$ , which is defined by the cosine of the angle ( $\varphi$ ) between loading axis  $\vec{F}$  and normal to slip plane  $\vec{N}$  and the cosine of the angle ( $\lambda$ ) between loading axis  $\vec{F}$  and the slip direction  $\vec{R}$  (Fig. 3.7).

$$\tau = \frac{F}{S_0} \cdot m = \sigma \cdot m = \sigma \cdot \cos\lambda \cdot \cos\varphi \quad (2.1)$$

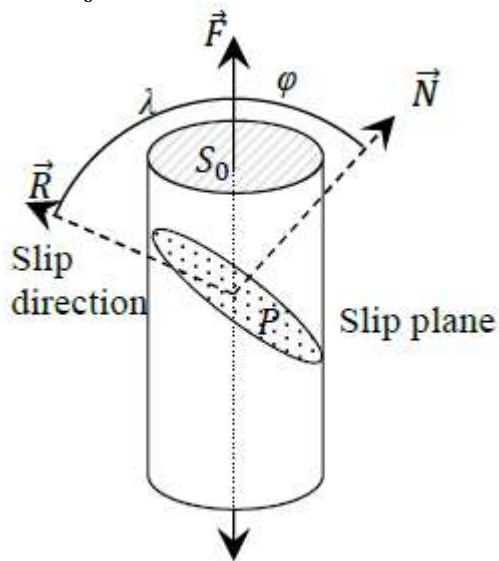


Fig. 2.7. Schematic illustration of plastic deformation in single crystal.

The  $\{10\bar{1}2\}$  extension twins typically obey the Schmid criterion, i.e. the twin variants with the highest Schmid factor ( $SF$ ) are activated first in a fashion similar to slip and therefore govern the texture evolution [73-75].

By analysis of  $\{10\bar{1}1\}$  contraction twinning in polycrystals, Jonas et al. [76] established a relationship between the twin variant selection and the necessary strain accommodation in neighboring grains. They found that high  $SF$  twin variants were less likely if their accommodation required appreciable amounts of prismatic slip in the neighboring grain. The same principle was used by Mu et al. [77] for the variant selection of primary, secondary and tertiary twins.

### 2.3. SINGLE CRYSTALS

When the atomic arrangement of a crystalline solid is perfect, throughout the entire sample, i.e., all the cells have a long-range order and it is not interrupted by grain boundaries, it is said that we have a single crystal.

The single crystals exist in nature but can also be generated artificially. The growth of these, in general, is difficult since the process must be controlled rigorously. In laboratories, growth techniques are used to avoid nucleation and favor the slow growth of appropriately sized crystals.

#### 2.3.2. SINGLE CRYSTAL GROWTH: BRIDGMAN TECHNIQUE.

In 1924 Percy Williams Bridgman achieved to grow single crystals of various materials in a cylindrical capsule, which was provided with a capillary tube at the bottom, the growth started at the tip of the capillary tube and propagated upwards along the tube as the capsule was slowly subtracted from the bottom of a vertical tube furnace of single temperature zone, this was due to the super cooling that was generated at the tip of the capillary when it was outside the furnace [78].

In 1935 Donald C. Stockbarger used a so-called "vertical riser furnace" that had two graphite heaters separated by a Mo deflector through which a coated crucible containing the melt could pass from the upper temperature region to a section of lower temperature by a motorized device. The use of a two-zone furnace led to better control of the thermal gradient in the growth interface [79].

The difference between the Bridgman technique and its variant by Stockbarger is simple, although both methods use a temperature gradient and a mobile crucible, the Bridgman technique uses a relatively uncontrolled gradient produced by the exit of the capsule towards the outside of the furnace; on the other hand, the Stockbarger variant uses a baffle that separates two coupled ovens with temperatures above and below the melting point. The Stockbarger modification of the Bridgman technique allows better control over the temperature gradient in the metal/glass bath interface.

There are many variants of the Bridgman technic, which depend on the physical-chemical and thermo-mechanical properties of the crystal materials to be obtained; but in general the system consists of a crucible in which polycrystalline material of the material of interest is introduced and is slowly passed through the interior of a furnace with two temperature zones, one of which is higher than the melting temperature and the other is slightly less than the same. The material passes to its liquid state when it is in the first zone, and then solidifies very slowly when descending to the zone of lower temperature, at the end of the crucible there is a monocrystalline seed, responsible for the nucleation process and consequent directional solidification, resulting in the formation of a monocrystal with the same crystallographic orientation as the seed along the crucible. The process can be carried out both horizontal and vertical configuration [80].

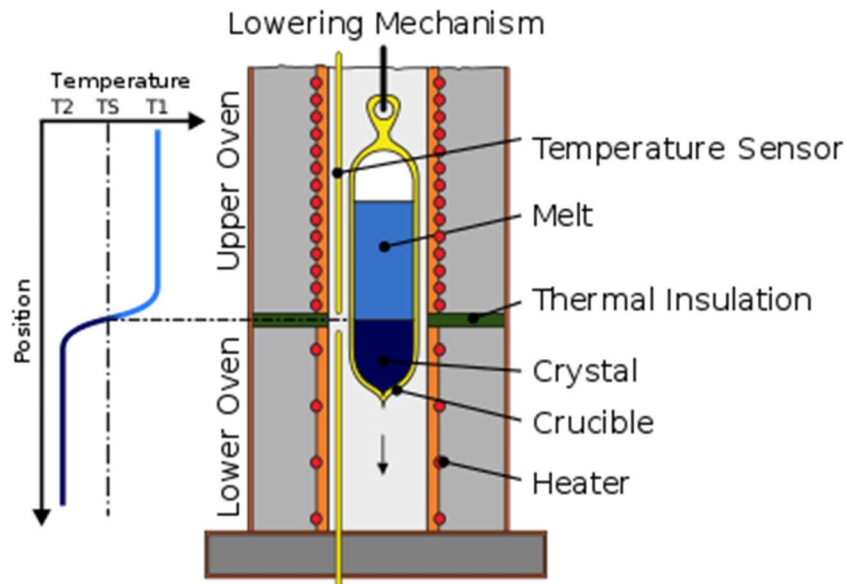


Fig. 2.8. Schematic representation of a vertical Bridgman furnace.

### 2.4. PROCESSING TECHNIQUES

Magnesium can be manufactured by all the conventional techniques including casting, forging, extruding and rolling. The choice of a method depends upon factors such as the configuration of the design, the application, the properties required, the total number of parts and the castability or formability of the alloy. In recent years, alternative techniques have been commercialized to improve the overall effectiveness of net shape forming.



### 2.4.2. ROLLING

Magnesium and its alloys can be processed by conventional thermomechanical treatments, which, by heating, deformation and controlled cooling, performed cyclically modify the microstructure, which influences on its mechanical properties. The most common processes for forming magnesium alloys are extrusion, rolling and forging, however, the most used for obtaining large volumes of material is rolling. Rolling is a process in which a metal is plastically deformed, passing it two rolls in order to reduce its gauge. Due to its high productivity and strict dimensional control in the product, it is the most studied plastic metal forming process.

As other plastic deformation processes, the rolling process can be identified according to the temperature, hot or cold rolling. The difference between both lies in the generation or not of work hardening during deformation. In the first, it does not occur, due to the processes of softening (recrystallization), in the second, a hardening will be generated. In both cases the presence and level of hardening obtained will depend strongly on a) level and strain rate applied, b) microstructural properties of the material, and c) of the conditions under which the deformation process is carried out, (temperature, lubrication, state of deformation/stress, etc). Due to its limited formability and low heat capacity, magnesium rolling is carried out at high temperature. Further, re-heating has to be repeated several times to keep the material within the 250–450 °C range and complete the process. Typically, the magnesium develops a basal deformation texture during rolling, i.e. the c-axis alignment parallel to normal direction (basal texture), which difficult its post-rolling deformation [81].

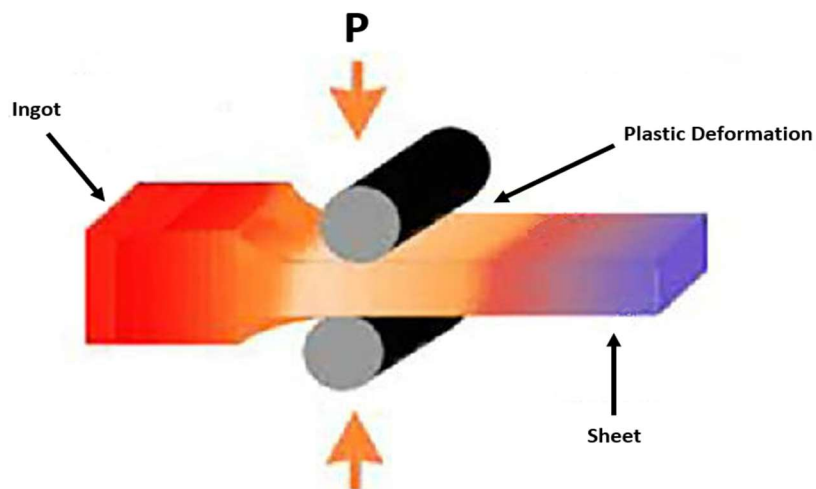


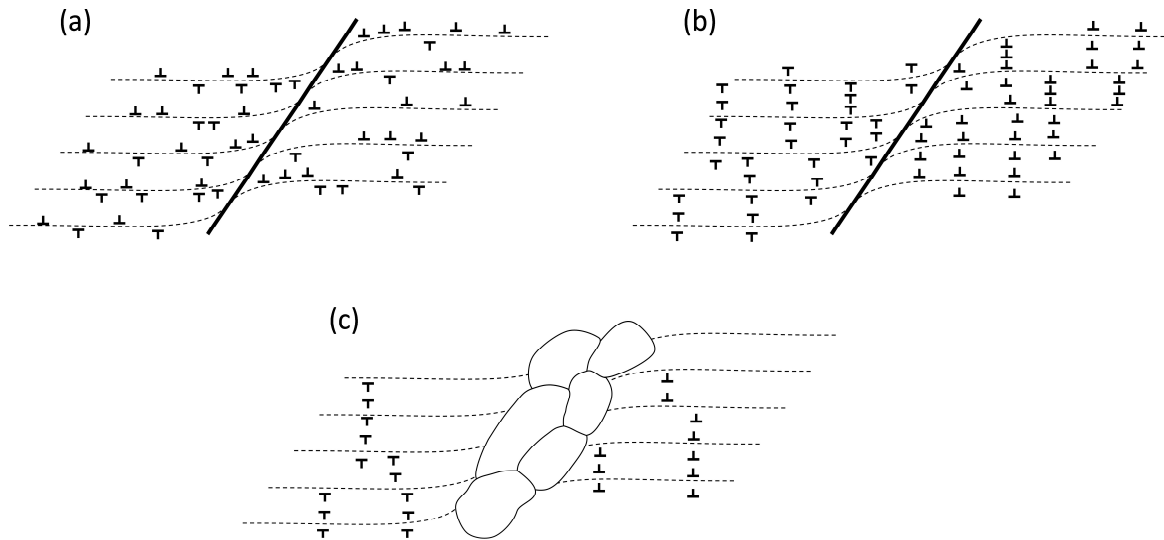
Fig. 2.9. Hot rolling process.

## 2.5. RECRYSTALLIZATION.

During plastic deformation of a crystalline solid at low homologous temperatures the free energy is considerably raised as result of an increase in dislocation density. These defects are retained after cold working, although not being thermodynamically stable. During subsequent annealing, new dislocation-free grains are formed, these grow and consume the surrounding deformed microstructure, reducing the free energy. This process that is characterized by nucleation and growth of strain-free grains, i.e. the migration of high angle grain boundaries, is referred to as static recrystallization (SRX).

When recrystallization is synchronous with plastic deformation, usually taking place at elevated temperature, it is referred to as dynamic recrystallization (DRX). Dynamic recrystallization is a softening mechanism, its occurrence lowers the flow stress and improves the ductility/formability. Since DRX has a great impact on the deformation behavior and texture evolution of polycrystalline magnesium during hot working, it is subject to extensive research efforts [82-90].

Generally, dynamic recrystallization can be of a continuous or discontinuous type. Discontinuous dynamic recrystallization (DDRX) is a classical nucleation and grain growth process, whereas continuous dynamic recrystallization (CDRX) is characterized by extensive recovery. CDRX proceeds by dynamic polygonization of rotated lattice regions near grain boundaries, i.e. rearrangement of dislocations into energetically more favorable substructures [82] (Fig. 2.10). With respect to the subgrain formation, it is important to point out that non-planar movement of dislocations as well as dislocations with  $\langle a \rangle$  type and  $\langle c+a \rangle$  type Burgers vectors are required for the formation of a three-dimensional dislocation network. With increasing strain, the subgrain (low angle grain boundaries) further evolve into high angle grain boundaries through an increase in misorientation. This increase in misorientation may be *i)* due to the absorption of dislocations from the adjacent subgrains or *ii)* a result of limited subgrain migration [91]. In the latter case, subgrain boundaries, which migrate under mechanical stress or driven by the locally high stored energy, collect dislocations and/or merge with other subgrain boundaries.



*Fig. 2.10. a) Accumulation of dislocations and lattice rotation at a grain boundary; b) rearrangement of dislocations into low angle boundaries through dynamic recovery in the vicinity of the original grain boundary; c) formation of high angle boundaries through dynamic recovery in the vicinity of the original grain boundary; c) formation of high angle boundaries through a progressive increase in misorientation, i.e. new grains emerge.*

In the particular case of Mg and Mg alloys, large experimental evidence suggests the occurrence of CDRX [82, 85, 87, 92-99] although conventional DDRX has also been reported as well, for instance, involving nucleation by grain boundary bulging [93, 100-102], i.e. strain induced grain boundary migration. In terms of the microstructure evolution, CDRX in grain mantle regions as well as grain boundary bulging produces a necklace-type microstructure, i.e. fine recrystallized grains along the original boundaries. However, CDRX has also been reported to result in the formation of shear bands by broadening and merging of recrystallized bands, with a higher strain rate in the shear zones producing a finer, yet equiaxed grain structure [82].

The occurrence of CDRX in magnesium is primarily ascribed to the lack of five independent slip systems needed for a homogeneous deformation of a polycrystal rather than an effect of the stacking fault energy. The inability of a grain to comply with an arbitrary shape change results in high local stresses and strain localization in the vicinity of grain boundaries, i.e. in the grain mantle region, involving pyramidal  $\langle c+a \rangle$  slip. In other words, plastic strain is accommodated in the mantle regions while the interior of the grains remains largely undeformed [82] or exhibits single crystal behavior with slip on the basal plane [100]. As a result, the grain boundary regions become increasingly misoriented with respect to the matrix. With increasing temperature, these mantle regions become wider [82].

Only at elevated temperature (above 300 °C), a homogeneous deformation of the whole grain is possible as  $\langle c+a \rangle$  slip becomes sufficiently available by thermal activation. In this sense, CDRX is a result of the prevalent deformation heterogeneity due to a lack of easily activated slip systems at intermediate temperatures and the constraints imposed by neighboring grains. Hence, the prerequisite for the occurrence of CDRX is inhomogeneous plasticity, activation of additional slip systems and dynamic recovery in the vicinity of grain boundaries. Retardation of grain boundary migration, e.g. due to solute drag, may also favor CDRX over conventional nucleation and grain growth [103].

Owing to the nature of CDRX, the deformation conditions determine the texture of the recrystallized grains [111], rather than the preferred nucleation and/or selective grain growth, which can lead to sharp recrystallization textures. This means that the orientations of newly recrystallized grains are usually well traceable to the parent host grain. Al-Samman et al. [104] reported CDRX in contraction twin bands during plane strain compression of pure Mg single crystals at elevated temperature (370 °C). The newly formed grains shared the same c-axis of their parent host twin but were rotated around the c-axis, forming a basal fiber texture. In a similar fashion, Chapuis [104] also observed recrystallization in double twins with newly recrystallized grains being rotated by 30° around the c-axis of the initial twin. This was interpreted in terms of a higher mobility of 30° [0001] grain boundaries. That said, Li et. al [105] studied the structure of boundaries with a 30° [0001] misorientation by MD (molecular dynamics) simulations and concluded that such boundaries have a high energy and form as a result of plastic spin, i.e. their formation is not thermodynamically driven.

### **2.6. STATE OF THE ART.**

In this section, a brief chronology of the research work in magnesium monocrystals will be presented, focusing on those involving plain strain compression (PSC) due to the similarity it presents with the rolling process, starting with those classic works that have been the basis of further research until the works currently developed.

In 1966, Wonsiewicz [23] studied the plasticity transition in magnesium in plane-strain compression of single crystals and polycrystalline material from room temperature to 307° C and conclude that in magnesium crystals unfavorably oriented for basal slip, extensive  $\{10\bar{1}1\}$ ,  $\{10\bar{1}2\}$  and  $\{10\bar{1}3\}$  twinning occurred. Large strains along the c-axis are only possible by operation of a double twinning mechanism -  $\{10\bar{1}1\}$  twinning followed by  $\{10\bar{1}2\}$  – and basal shear within the doubly twinned volume, hence enough independent shears for arbitrary shape change can be obtained through double twinning. However, fracture is a possible result of localized unloading from the high level of stress for initiating twinning to the much lower level for basal shear in a twin. It has been argued that ductility is achieved by raising temperature because the stress difference is lowered and the twin volume, in which elastic strain energy is dissipated on unloading, is increased. There is no critical resolved shear stress for  $\{10\bar{1}1\}$  twinning. That has been attributed to the influence of local stress concentration at the twin site from prior intersecting shear.

In 1967, Kelly [24] performed deformation studies conducted at room temperature on single crystals and textured polycrystals of magnesium. Single crystals oriented to suppress shear on the easily activated basal slip systems were deformed by plane-strain compression. Compression along the c-axis was accommodated by  $\{10\bar{1}1\}$  banding consisting of  $\{10\bar{1}1\}$  twinning followed by  $\{10\bar{1}2\}$  retwinning and basal slip within the double twinning band. Compression perpendicular to the unconstrained c-axis activated  $\{10\bar{1}2\}$  twinning, and, after virtually complete twinning, deformation continued by  $\{10\bar{1}1\}$  banding in the twinned material. Compression perpendicular to the constrained c-axis was accommodated by the simultaneous operation of  $\{10\bar{1}2\}$  twinning against the constrain and  $\{10\bar{1}1\}$  banding. Although this orientation was favorable for  $\{10\bar{1}0\}$   $\langle 1\bar{2}10 \rangle$  prism and  $\{10\bar{1}1\}$   $\langle 1\bar{2}10 \rangle$  pyramidal slip, these modes were not observed in pure magnesium. Fracture in pure magnesium occurred parallel to  $\{11\bar{2}4\}$  under compression along the c-axis or  $\langle 10\bar{1}1 \rangle$  by compression perpendicular to the c-axis.

Recently, in 2011, Chapuis [47] characterized the critical resolved shear stresses (CRSSs) of slip and twinning in magnesium crystals, as a function of temperature, by channel-die compression tests from room temperature to 450°C using the experimental stress–strain curves and orientation maps from EBSD measurements, which gave unequivocal primary and secondary twin determinations. It is shown that under these straining conditions basal slip and  $\{10\bar{1}2\}$  tensile twinning are not very temperature-dependent. Prismatic and Pyramidal II slip are clearly identified and measured only above 300°C. Both compressive twinning systems  $\{10\bar{1}1\}$  and  $\{10\bar{1}3\}$  are very temperature-dependent so that their CRSSs decrease by a factor of three from 150 to 350°C.

In 2012, Al-Samman [87] studied the recrystallization mechanism on magnesium single crystals subjected to plane strain compression along the c-axis at 200 and 370°C and a constant strain rate of  $10^{-3} \text{ s}^{-1}$ . The microstructure of the specimen strained at 200 °C was characterized by a high density of extensive  $\{10\bar{1}1\}$  and  $\{10\bar{1}3\}$  compression twins, as well as  $\{10\bar{1}2\}$  twins formed within the primary twins by secondary twinning events. Some compression twins in the specimen tested at 200 °C were transformed into recrystallized bands comprising new grains. During straining at 370 °C, mechanical twinning was markedly less intensive than at 200°C, and all twins were practically converted into extensively recrystallized macroscopic bands. The mechanism of dynamic recrystallization within the twin bands was identified to be of a “continuous” nature (CDRX), based upon extensive dynamic recovery generating new grains. These new recrystallized grains were found to retain the same c-axis orientation as in their compression twin host. The orientation distribution of the recrystallized grains correlated with the specific character of the boundaries separating these grains from the adjoining matrix. These boundaries were characterized by the same misorientation angle ( $56^\circ \pm 5^\circ$ ) relating a  $\{10\bar{1}1\}$  compression twin to its parent grain. The rotation axes of the new grain boundaries were scattered within a maximum spread of  $30^\circ$  from the ideal twin rotation axis  $\langle 1\bar{2}10 \rangle$ . It is anticipated that the new boundaries resulting from CDRX have a higher mobility than the initial twin boundary with a tilt character, which explains the observed expansion of twin bands as a function of strain.

In 2013, Li [106] tested magnesium single crystals under compressive loadings at a quasistatic strain rate ( $0.001 \text{ s}^{-1}$ ) and a dynamic strain rate ( $1000 \text{ s}^{-1}$ ) at room temperature. Dynamic loading led to much higher maximum strength and larger strain hardening rate than quasistatic loading for the tested material. The microstructure features were clearly different from each other for the two loading conditions, which indicated that the deformation mechanisms for the quasistatic testing were different from those for the dynamic testing. The results showed that the dominating deformation mechanism was dislocation motion on  $\{1\bar{1}00\}$   $\{1\bar{2}10\}$  prismatic slip systems and  $\{11\bar{2}2\}$   $\{1\bar{1}23\}$  secondary pyramidal slip systems for dynamic loading. Both dislocation motion and twinning were observed in the sample under quasistatic loading, and the sample became polycrystalline through  $\{10\bar{1}1\}$ - $\{10\bar{1}2\}$  double twinning and  $\{10\bar{1}2\}$  tension twinning; and no twinning was observed for the sample subjected to dynamic loading, a possible reason was the faster increase of the critical resolved shear stress for twinning than that for dislocation slip.

In 2014, Chapuis [104] analyzed single crystals of magnesium compressed along  $\langle 10\bar{1}10 \rangle$  and with the (0001)  $\langle c \rangle$  axis constrained deformed at 150 and 250°C. A combination of tensile twinning  $\{10\bar{1}2\}$ , compression twinning  $\{10\bar{1}1\}$  and double twinning  $\{10\bar{1}1\}$ - $\{10\bar{1}2\}$  was observed by EBSD analysis. At 250°C recrystallization took place in double twins and the orientation of the new grains have the same  $\langle c \rangle$  axis as the double twin but with an  $\langle a \rangle$  axis misoriented at 30°.

Since 2013, Molodov [25-31] has performed detailed and systematic studies on single crystal under PSC. Compression along the  $c$ -axis, i.e. crystals of 'hard' orientations, revealed limited room-temperature ductility. However, pyramidal  $\langle c+a \rangle$  slip was very well active, even at room temperature, while  $\{10\bar{1}1\}$  contraction twinning was not revealed. Fracture in  $c$ -axis contraction always occurred along recrystallized  $\{11\bar{2}4\}$  bands that were found to be a result of highly localized shear. At elevated temperature,  $c$ -axis compression is aided by contraction twinning, dynamic recrystallization and a reduced tendency for shear localization. In the case of  $c$ -axis extension, a high room temperature ductility could be achieved by preventing the formation of a basal texture component due to multiple extension/contraction twinning and the occurrence of dynamic recrystallization inside contraction twin bands as a result of shear localization.

In the case of *c*-axis extension, a high room temperature ductility could be achieved by preventing the formation of a basal texture component due to multiple extension/contraction twinning and the occurrence of dynamic recrystallization inside contraction twin bands as a result of shear localization. Dynamic recrystallization was not found to operate in  $\{10\bar{1}2\}$  extension twins, owing to a lack of shear localization in this twin type and the ease of growth of  $\{10\bar{1}2\}$  extension twins. At room temperature, prismatic slip was not revealed to operate in single crystals that were most favorably aligned for prismatic slip, which is at odds with the apparent activation of prismatic slip in  $\{10\bar{1}1\}$  twin bands under conditions of extensively localized shear. Instead,  $\{10\bar{1}2\}$  extension and  $\{10\bar{1}1\}$  contraction twinning was activated in a cooperative fashion to substitute prismatic slip and enable plane strain compression of the single crystals. Deformation localized within  $\{10\bar{1}1\}$  contraction bands (including  $\{10\bar{1}1\}$ - $\{10\bar{1}2\}$  double twins), as in the case of *c*-axis extension, and led to continuous dynamic recrystallization, i.e. softening and continued deformation within the bands.  $\{10\bar{1}1\}$  contraction twin bands were also revealed to be crack initiation sites with fracture occurring along such bands when the capacity to accommodate the localized shear was exhausted. To this end, the propensity for fracture was highly sensitive to the strain rate imposed; at high strain rates fracture occurred immediately along  $\{10\bar{1}1\}$  contraction twin bands, while at low strain rates dynamic recrystallization aided to prevent fracture. While the dominant  $\{10\bar{1}2\}$  extension twin variants were generally found to correspond to high Schmid factor variants, particularly when such twins constituted a primary mode of deformation, the anomalous extension twins, which formed in the case of 'soft' orientations aligned for basal slip, were characterized by negative Schmid factors and produced strain opposite to the imposed deformation. The twinning shear brought about a lattice spin opposite to the lattice rotation introduced by basal slip. Hence, such anomalous twins were activated as a result of deformation heterogeneity with respect to the orientation change induced by basal slip. An increase in temperature reduced the tendency for anomalous extension twinning but resulted in the formation of small angle grain boundaries with a misorientations axis parallel to the spin axis for basal slip, i.e. polygonization occurred as a result of slip heterogeneity.





# Experimental

The experimental procedure of this work is presented in Fig. 3.1 as a block diagram and each step is described in detail below. It is worth mentioning that most of the experimental work was carried out at the *Institut für Metallkunde und Metallphysik (IMM)* facilities of the *RWTH Aachen University* and the complementary work was done at *Departamento de Ingeniería en Metalurgia y Materiales (DIMM)* of the *Instituto Politécnico Nacional*.

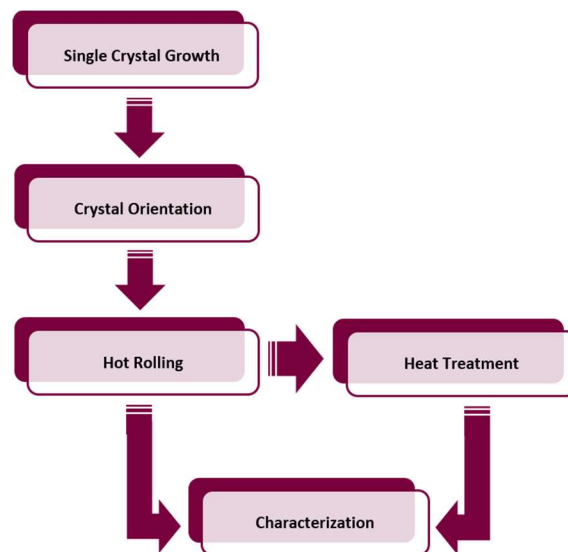


Fig. 3.1. Experimental Procedure Diagram.

### 3.1. SINGLE CRYSTAL GROWTH

For the growth of single crystals of commercially pure magnesium (min. 99.95%, the chemical composition is given in Appendix A), cylindrical single crystal seeds ( $\varnothing$  5 mm  $\times$  25 mm) with the *c*-axis aligned parallel to its symmetry axis were cut from a randomly oriented magnesium single crystal by electrical discharge machining (EDM) on a *Fanuc Robocut  $\alpha$ -0iA* machine in order to avoid any plastic deformation in the material.



Fig. 3.2. *Fanuc Robocut  $\alpha$ -0iA* EDM machine.

The polycrystalline blanks (Fig. 3.3b) and seeds (Fig. 3.3c) were etched with a 15%  $\text{HNO}_3$ , the blank was boiled in distilled water for several minutes in order to form a stable oxide layer on the surface. The oxide layer acted as a barrier between the mold and the molten Mg inside, preventing diffusion and adherence. In order to guarantee physical contact between the seed and the blank, the oxide layer was removed from the front face of the seed and blank by careful grinding with 4000 silicon carbide paper until expose the metallic surface, i.e., until observe with the naked eye a change in the surface from opaque gray-white to a metallic shine.

After the preparation the polycrystalline blank and the crystal seed were placed inside a cylindrical steel crucible (Fig. 3.3.a) and fixed with graphite paper. It is important to mention that steel used for the crucible did not contain any Ni to prevent contamination. The inside of the crucible was covered with a graphite-based die coating (*Acheson Hydrokollag IP 5*).

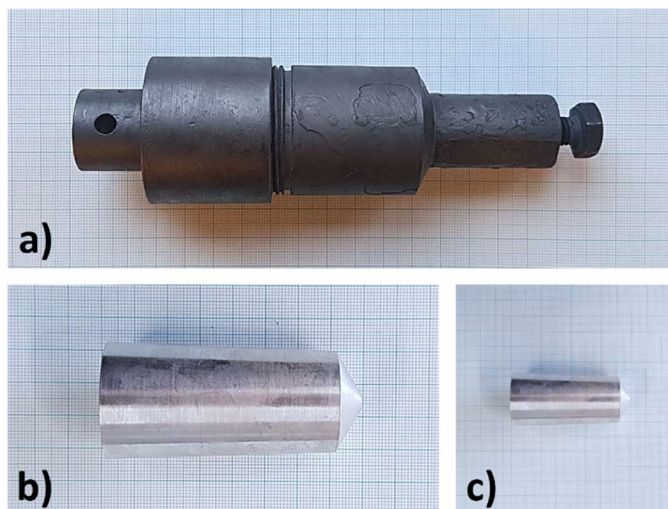


Fig. 3.3. a) Steel Crucible, b) Polycrystalline Blank, c) Crystal seed

Finally, the oriented single crystals were grown by directional solidification using the Bridgman-method in a vertical configuration (Fig. 3.4). Argon atmosphere was used to avoid oxidation of the magnesium melt. After a holding time of 3 h in order to completely melt the polycrystalline blank and the upper part of the single crystal seed (that was in contact with the blank), the crucible was lowered slowly at a velocity of 0.53 cm/h, translating the Mg melt along the temperature gradient from the hot zone to the cold zone in the furnace. Including the initial holding and final cooling time the procedure took about 20 h. After cooling was complete, the crystal was carefully taken out of the crucible and etched in a 15% solution of nitric acid to clean the surface.



Fig. 3.4. Bridgman vertical furnace for single crystal growth.

The front end (seed) and the rear end of the crystal were cut off by electrical discharge machining, polished and etched with a 5% acid nitric solution to verify that no grain boundaries were present. The resulting crystals had a conical shape with a base diameter of 34 mm, a length of 56 mm and an opening angle of  $4^\circ$  (Fig. 3.5c).

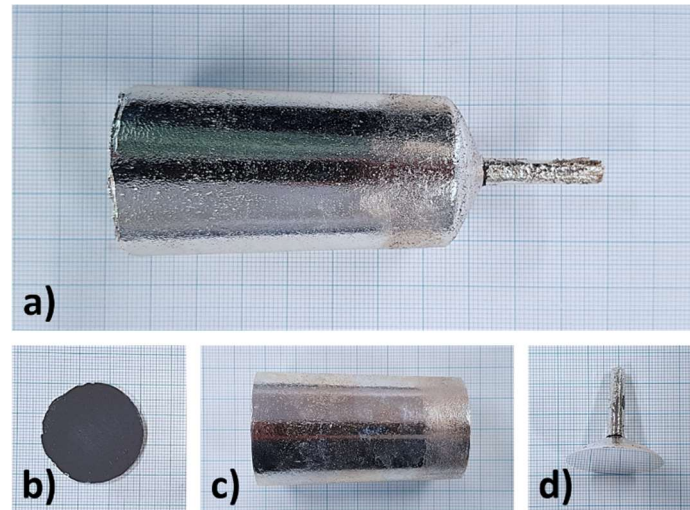


Fig. 3.5. a) Entire single crystal after cleaning, b) Upper end, c) Conical single crystal, d) Lower end (seed).

### 3.2. CRYSTAL ORIENTATION

After the growth process each single crystal was etched with a 15%  $\text{HNO}_3$  solution and the back end of the crystal was stuck to a brass disk using glue with copper wire immersed in it to ensure conductivity during EDM, then the crystal was fixed in a 3-axis brass goniometer (Fig. 3.6) and aligned according to the desired final orientation of the specimens by means of the Laue X-ray back diffraction method [107].



Fig. 3.6. Crystal mounted on the goniometer.

The Laue-reflections were acquired using a Laue camera developed at IMM (Fig. 3.7) equipped with a *Seifert Analytical* x-ray source, *Photonic Science* Laue Detector and the *PSL Viewer* software using 45 kV and 30 mA. The positions of Laue-reflections were analyzed and indexed with the *OrientExpress* software which allows to know the necessary rotations to obtain the desired orientation of the crystal. The crystallographic axes of the grown single crystals were oriented with respect to the specimen coordinate system. The Laue-patterns are presented in Appendix B. After alignment, monocrystalline rolling blocks with dimensions of 40 mm × 20 mm × 6 mm were fabricated from the oriented single crystals by EDM.

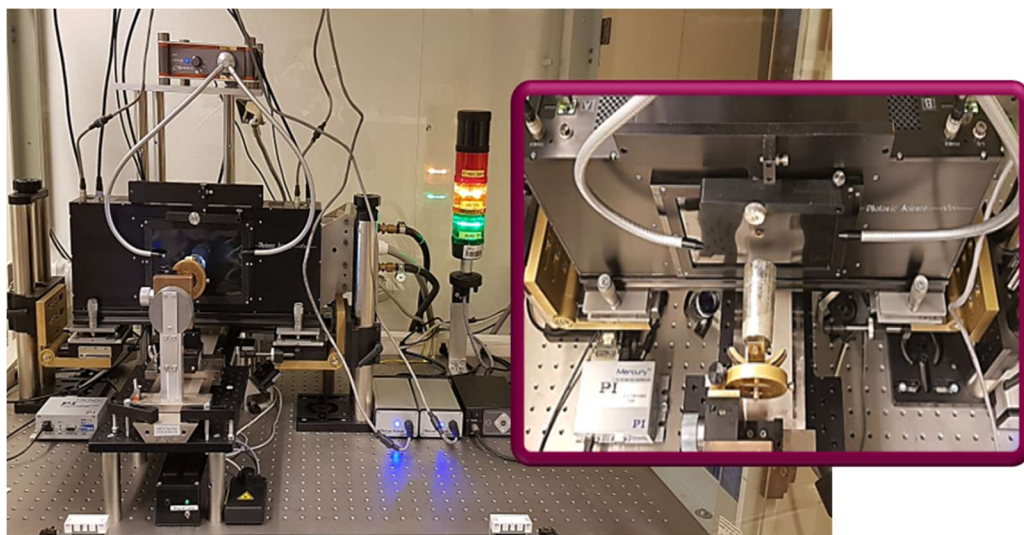


Fig. 3.7. Laue camera used for crystal orientation by X-ray back diffraction

The crystal orientation with respect to the rolling system coordinate of the samples is illustrated in Fig. 3.8. The c-axis of the crystal were aligned parallel to the rolling direction, both  $[10\bar{1}0]$  as well as  $[11\bar{2}0]$  crystal directions were aligned parallel to the normal direction giving rise to two different orientations. In “orientation 1” (O-1) the normal direction was aligned to  $[10\bar{1}0]$  crystal direction and the transversal direction corresponds to  $[11\bar{2}0]$ . In the case of the “orientation 2” (O-2) the normal direction was aligned to  $[11\bar{2}0]$  crystal direction and the transversal direction to  $[10\bar{1}0]$ . The misalignment between the crystallographic directions and the specimen axes, rolling (RD), normal (ND) and transversal directions (TD), was less than  $0.5^\circ$ .

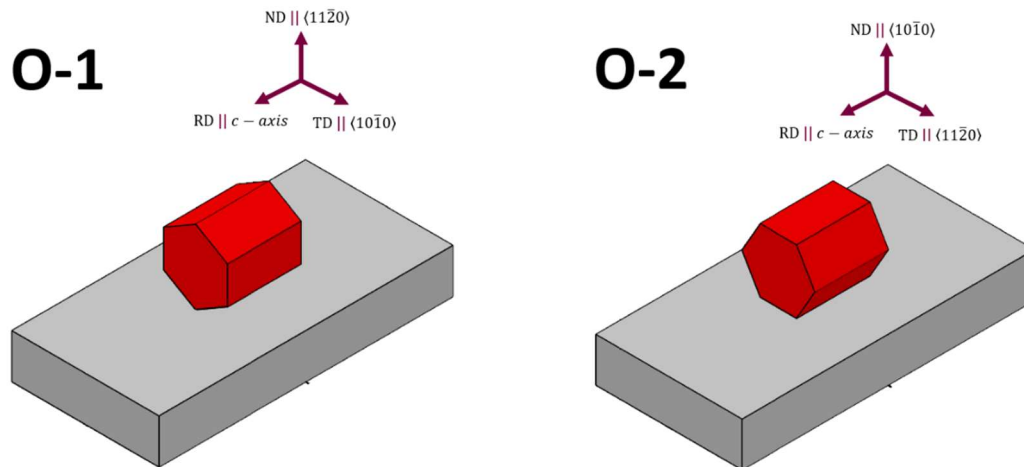


Fig. 3.8. Crystal orientation scheme of rolling blocks.

### 3.3. HOT ROLLING

For the rolling experiment the specimens of both orientations were heated at  $400^\circ\text{C}$  (nominal furnace temperature) for 30 min. inside a *Thermoconcept* furnace (Fig. 3.9a), then each sample was rolled at a speed of 200 mm/s to 80% thickness reduction in a *Carl Wezel* rolling mill (Fig. 3.9b) by 16 rolling passes at different true strains ranging from 0.05 to 0.2 ( $\varphi = \ln \left( \frac{t_1}{t_0} \right)$ ;  $t_1$  and  $t_0$  are final and initial thicknesses), a heating time of 10 min at  $400^\circ\text{C}$  was given between each rolling pass. The rolling schedule can be consulted in Appendix C for more details. For minimizing friction between magnesium blocks and rolls, oil was used as lubricant.

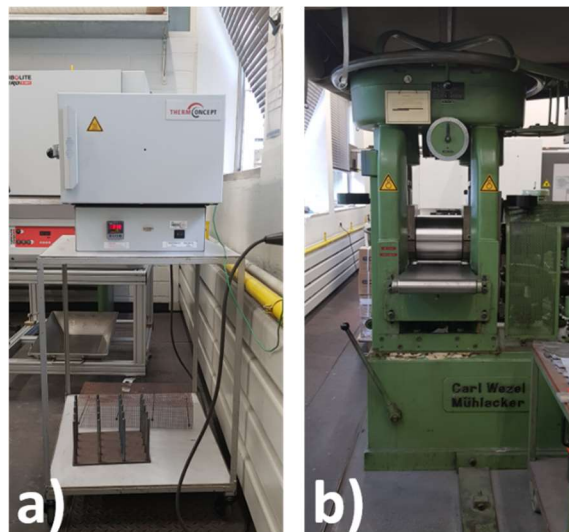


Fig. 3.9. a) Thermoconcept Furnace used for heating, b) Carl Wezel Rolling Mill.

For a more complete analysis some samples were rolled to intermediate deformations of ~30 and ~50% (7 and 11 passes) in order to characterize the phenomena that take place in the different stages of deformation. At the end of the tests the sheets were rapidly quenched in water to freeze the microstructure and prevent post deformation static recrystallization.

### 3.4. HEAT TREATMENT

Post rolling, some samples were cut from the sheets by electrical discharge machining in order to analyze the deformation microstructure along the whole sheet as shown in Fig. 3.10. As already mentioned, the sheets were quenched to retain the deformation microstructure and analyze the variants of twins present. Therefore, it was necessary to submit a section of the 80 % sheet to a thermal treatment to give rise to the recrystallization process and its subsequent analysis. For this, one of the samples was subjected to annealing treatment at 400°C for 30 min followed by a cooling inside the furnace.

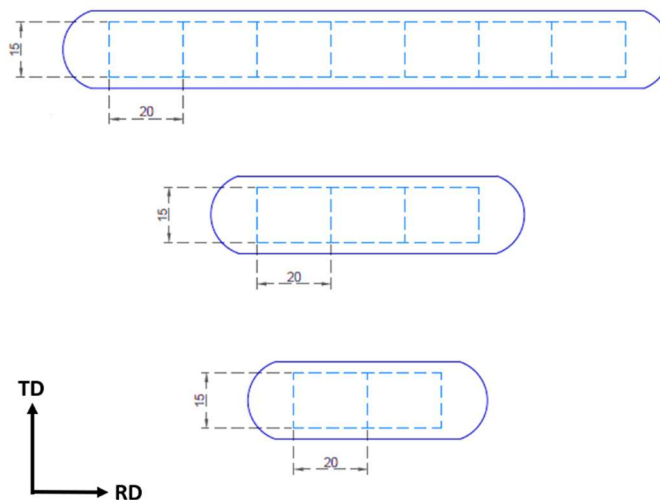


Fig. 3.10. Scheme of the samples cut from the sheet (mm).

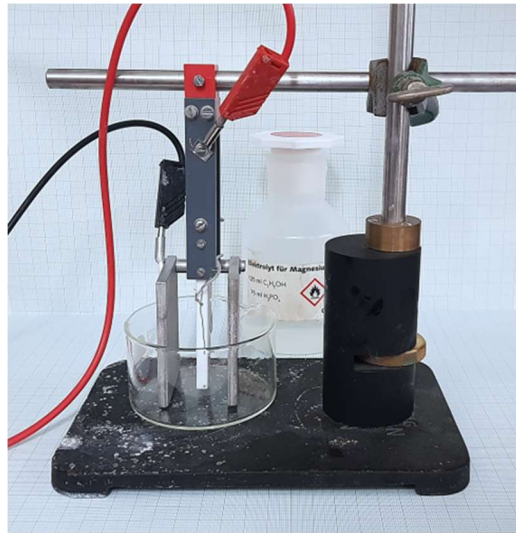
### 3.5. CHARACTERIZATION

#### 3.5.1. SAMPLE PREPARATION

The sample preparation consisted of soft grinding with 2000 and 4000 SiC-paper using ethanol as lubricant, followed by 3 and 1  $\mu\text{m}$  diamond polishing at a very low rotation speed using ethanol as coolant until scratches could not be recognized visually.



Post diamond polishing, electropolishing in a solution of 125 ml ethanol and 75 ml  $\text{H}_3\text{PO}_4$  was performed at 2.0 V completely submerging the specimens in the electrolyte for 40 min (Fig. 3.11). After removing the specimens from the electrolyte they were immediately rinsed under water jet and subsequently washed with ethanol to get a mirror surface. Electropolishing was performed for all the characterization techniques used, optical microscopy, X-ray and electron backscatter diffraction.



*Fig. 3.11. Electrolytic cell and electrolyte used for electropolishing.*

In the case of microstructural characterization by optical microscopy, after electropolishing a chemical color-etching with a freshly solution of 10 ml  $\text{H}_2\text{O}$ , 10 ml  $\text{CH}_3\text{COOH}$  and 70 ml picral 4% was necessary. Specimens were immersed into the solution until samples turned brown while maintaining a slow circling agitation and subsequently rinsed with ethanol.

For EBSD, the electropolishing was followed by a chemical polishing with a solution comprising 12 ml  $\text{HCl}$ , 8 ml  $\text{HNO}_3$  and 100 ml methanol for 5 s by a process similar to chemical etching in order to remove the oxide layer that could have formed in the electropolishing due to water, finally the samples were immediately taken to vacuum to avoid a subsequent oxidation.

### **3.5.2. OPTICAL MICROSCOPY (OM)**

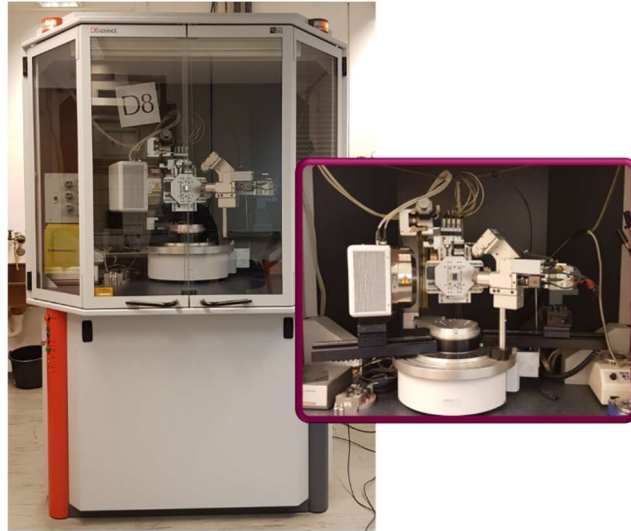
Microstructural characterization was performed on a *Zeiss Axioscop II Mat* optical microscope (Fig. 3.12). Metallographies of the lamination plane (RD-TD) were acquired at different magnifications (50-500X).



*Fig. 3.12. Zeiss Axioscop II Mat optical microscope*

### **3.5.3. X-RAY DIFFRACTION (XRD)**

The X-ray pole figure (PF) measurements were conducted using a Bruker D8 Advance diffractometer (Fig. 3.13), equipped with a HI-STAR multi-wire X-ray area detector with a circular beryllium window. Filtered iron ( $\text{Fe-K}\alpha$  with a characteristic wavelength  $\lambda\alpha=1.937 \text{ \AA}$ ) radiation and polycapillary focusing optics were used to concentrate the flux from the long fine focus X-ray tube, operating at 30 kV and 25 mA. Measurements were performed with a 0.5 mm pinhole collimator, resulting in a circular spot with a diameter of about 0.8 mm when the specimen surface was normal to the incident beam. The sample stage was oscillated to cover a larger measurement area/volume for improved statistics. The calculated penetration depth of the incident beam was in the range of 5-55  $\mu\text{m}$ , depending on the diffraction angle and tilt of the sample. A set of six incomplete pole figures of the  $\{10\bar{1}0\}$ ,  $(0002)$ ,  $\{10\bar{1}1\}$ ,  $\{10\bar{1}2\}$ ,  $\{11\bar{2}0\}$ , and  $\{10\bar{1}3\}$  families of lattice planes were measured and used to determine the orientation density function (ODF) using MTEX toolbox [108]. Measurement times were about 1 h per sample for an exposure time of 10 s per frame.



*Fig. 3.13. Bruker D8 Advance diffractometer used for global texture measurements.*

### **3.5.4. ELECTRON BACKSCATTER DIFFRACTION (EBSD)**

Electron backscatter diffraction (EBSD) measurements were conducted on a JEOL JSM-6701F scanning electron microscope (Fig. 3.14) equipped with a field emission gun with a LaB6 filament and an HKL-Nordlys II EBSD detector to characterize the microstructure and microtexture. The samples were mounted on brass holders to ensure a perfect alignment and tilted to 70° (from the horizontal) towards the EBSD detector to increase the backscattering yield. An acceleration voltage of 30 kV was used for all measurements.



*Fig. 3.14. JEOL JSM-6701F scanning electron microscope equipped with HKL-Nordlys II EBSD detector.*

# Results

The investigated pure Mg single crystals rolled at 400°C with two different initial orientations showed a very similar behavior. The sheets are shown in the Fig. 4.1, all of them present a smooth surface without visible cracks at all strains for both cases. The table 4.1 presents the final dimensions of each sheet, it is important to note that both orientations shared a geometry with the c-axis parallel to the rolling direction but orientation 1 (O-1) has a 30° rotation around the c-axes with respect to the orientation (O-2), despite this there is not significant changes in the final dimensions which could indicate changes in the deformation behavior caused by the crystallographic orientation difference, displaying the characteristic anisotropy of magnesium and its hcp structure.

Table 4.1. Dimensions of the obtained sheets for both orientations.

(mm)	Orientation 1			Orientation 2		
	30%	50%	80%	30%	50%	80%
Thickness	4.16	2.81	1.21	4.17	2.80	1.21
Long	54.00	79.00	172.00	56.00	79.00	166.00
Wide	23.50	23.00	24.50	22.00	23.00	25.00

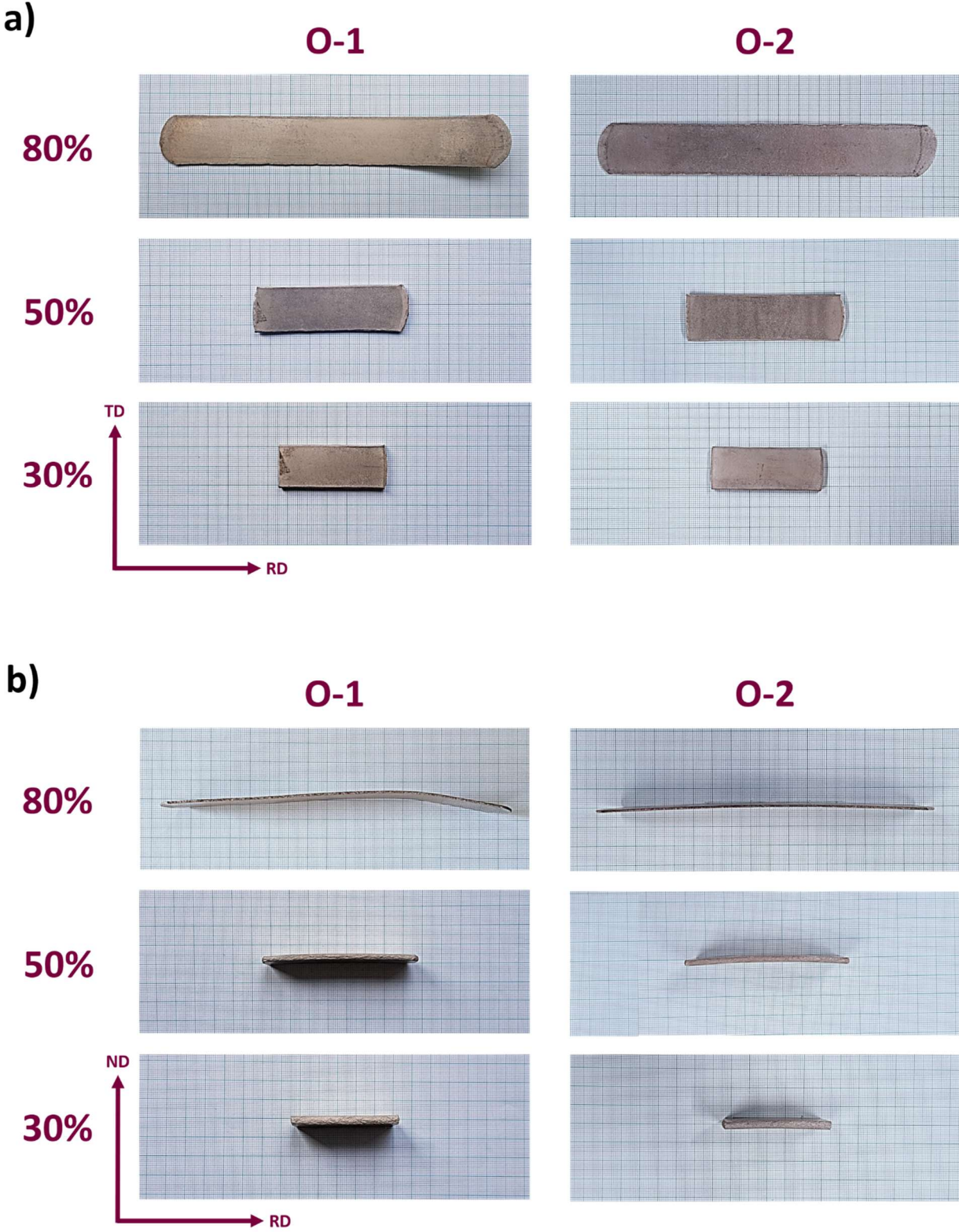


Fig. 4.1. Pictures of magnesium hot rolled sheets of orientation 1 and orientation 2 at  $\epsilon = 30, 50$  and  $80\%$ . a) RD-TD plane, b) RD-ND plane.

#### 4.5. MICROSTRUCTURE EVOLUTION DURING ROLLING PROCESS.

The microstructure of the rolled samples was examined by optical microscopy and the results are presented in Fig.4.2. It shows the microstructure gradually changed with the deformation during rolling. Different microstructural features can be clearly observed at different strains for both orientations. But overall, the single crystal has been totally turned into a polycrystal of relatively equiaxial grains with a particular characteristic, they present straight grain boundaries, so it seems more accurate to describe them as polygonal grains. In addition, twinning seems to be active and leads the subsequent development of recrystallized twin bands consisting of fine dynamic recrystallized (DRXed) grains along twin bands, indicating their importance as nucleation sites, both rolled orientations exhibited a dense network of twin bands distributed homogeneously throughout the whole RD–ND plane and formed symmetric pairs inclined  $\sim 60^\circ$  between them. It is important to note that these twins are within a matrix totally different from the initial matrix (single crystal) as shown by the orientation maps in section 4.3.

At  $\varepsilon = 30\%$  many lenticular twins were observed in all grains, in O-1 as well as in O-2. In the case of O-1, the darker grains seem to have been consumed almost completely by twinning, another important feature to mention is the presence of some recrystallized twins within the lighter grains suggesting the onset of DRX process. As for the O-2, in some grains the twins have a lamellar structure and seem to be coarser compared to O-1, also the phenomenon of recrystallization within the twins is more evident.

With further deformation (at  $\varepsilon = 50\%$ ) the microstructure of O-1 was finer due to the formation of new twins, most of these twins show very fine recrystallized grains inside, however, some recrystallization free twins were observed. Regarding the O-2, fewer twins were observed but, in this case, they were even thicker than those observed at 30% and coalesced in some grains. As in the O-1, recrystallized grains were also observed inside the twins and some twins without recrystallization were still identified.

Finally, at  $\varepsilon = 80\%$ , the O-1 exhibited a partially recrystallized and heterogeneous microstructure perfectly described by three zones, one of them to the left, the second at the center and the last to the right of the micrograph. In the first, recrystallized grains almost consumed all the matrix (there was a grain growth considering the size of recrystallized grains observed in previous strains). In the second, some recrystallized coarse twins as well as recrystallization-free twins were found. Finally, the third zone can be described as the transition between the first two zones, some twin-like morphologies, recrystallized twin bands and perfect twins were observed, suggesting that the grains initially recrystallized within the twins, grow and consume the surrounding matrix.

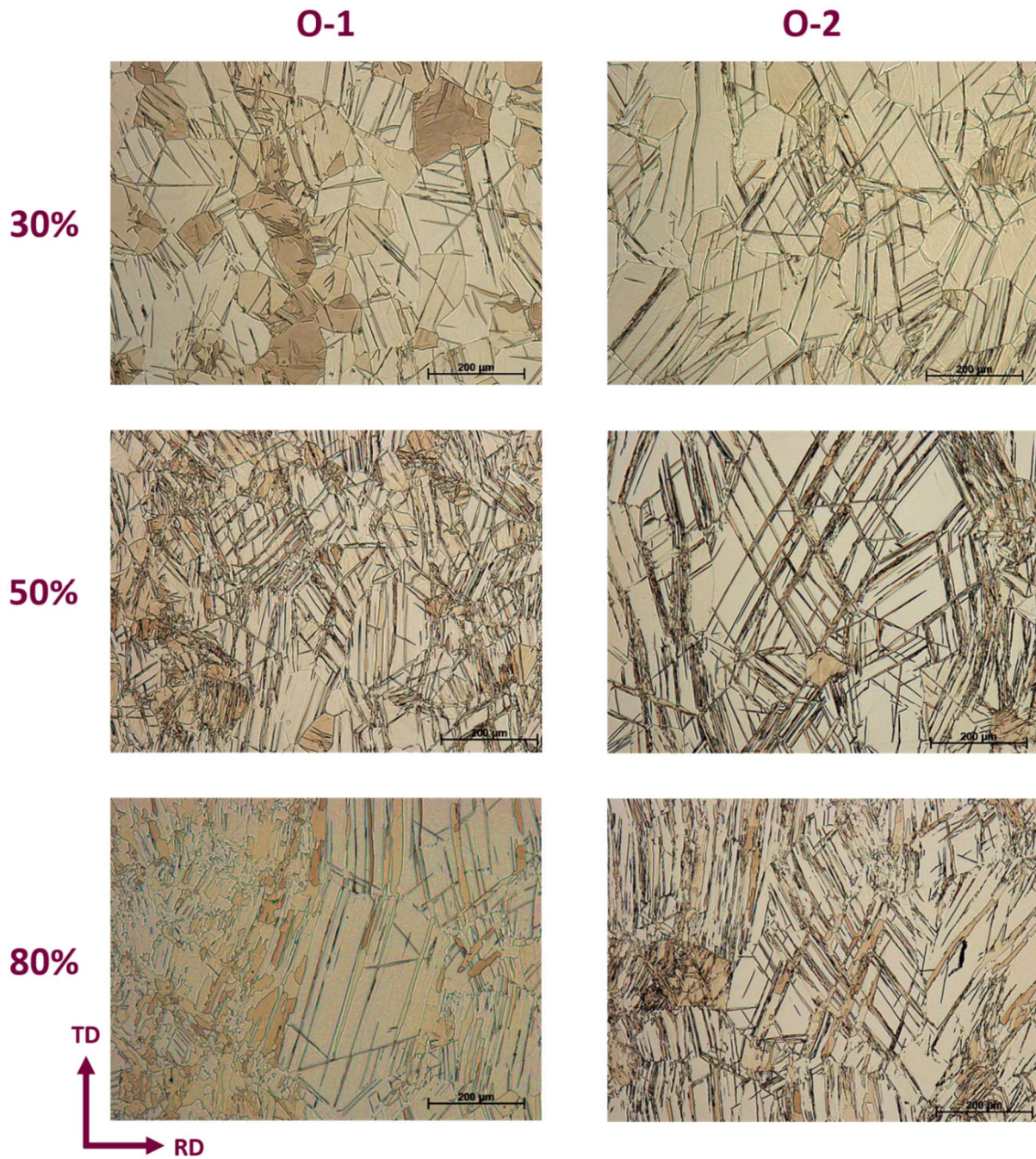


Fig. 4.2. Optical micrographs of the RD-TD plane after rolling at different strains.

As for O-2, the microstructure is very similar to O-1 at 50%, the formation of new twins and the presence of recrystallized twin bands were observed, the latter seem to have become thicker consuming the surrounding matrix.

It can be observed that recrystallized fraction within the twins increased markedly and consume the matrix as the rolling progresses. These observations indicate that twinning and subsequent DRX process play dominant roles in the microstructural evolution during rolling.

#### 4.6. TEXTURE EVOLUTION DURING HOT ROLLING.

Texture measurements were carried out on all the samples along the sheets (Fig. 3.10) and the average texture was reported by means of inverse pole figures in Fig. 4.3, the texture measurements for each particular specimen are presented in Appendix D.

Fig. 4.3. shows the texture evolution during hot rolling for both orientations by means inverse pole figures (IPF), there are not significant differences between them, in general a strong basal texture was observed for both orientations at any strain. This suggests that the typical basal texture of rolled magnesium had already formed at the first rolling passes which can be attributed to the rotation of the structure caused by extension twinning where the basal planes are aligned parallel to the RD topic that will be addressed in chapter 5.

For O-1 at the early stage of  $\varepsilon = 30\%$ , the ND inverse pole figure exhibits a strong basal texture with an intensity value of **15.8** and the corresponding RD and TD inverse pole figures reveal a very weak basal component parallel to RD and TD respectively, but the principal texture component in this IPFs tended to distribute homogeneously along the arc between  $\langle 10\bar{1}0 \rangle // RD$  and  $\langle 11\bar{2}0 \rangle // RD$ . On the other hand the O-2 presents a stronger basal texture with a maximum of **22.3** and shows a weak  $\langle 10\bar{1}0 \rangle$  component parallel to RD, therefore the  $\langle 11\bar{2}0 \rangle$  component is parallel to TD.

With increasing strain at  $\varepsilon = 50\%$ , in the O-1 texture, the basal component intensity became strengthened and reached a peak value of **18.5** according to the ND inverse pole figure, only the TD still retained the very weak basal component. By contrast the ND inverse pole figure of the O-2 shows a basal intensity decrease to **20.8** and the components in RD and TD inverse pole figures seems to tend to distribute along  $\langle 10\bar{1}0 \rangle$  and  $\langle 11\bar{2}0 \rangle$ .

At the final strain,  $\varepsilon = 80\%$ , the basal component intensity in the ND was weakened to **16.0**, the RD presents a very weak basal component and no specific  $\langle 10\bar{1}0 \rangle$  and  $\langle 11\bar{2}0 \rangle$  fibers parallel to RD and TD were found in the O-1. Regarding to O-2, increasing the strain resulted in slight intensification to **22.5** of the basal texture component parallel to ND, the  $\langle 10\bar{1}0 \rangle$  and  $\langle 11\bar{2}0 \rangle$  components were also distributed homogeneously along RD and TD.



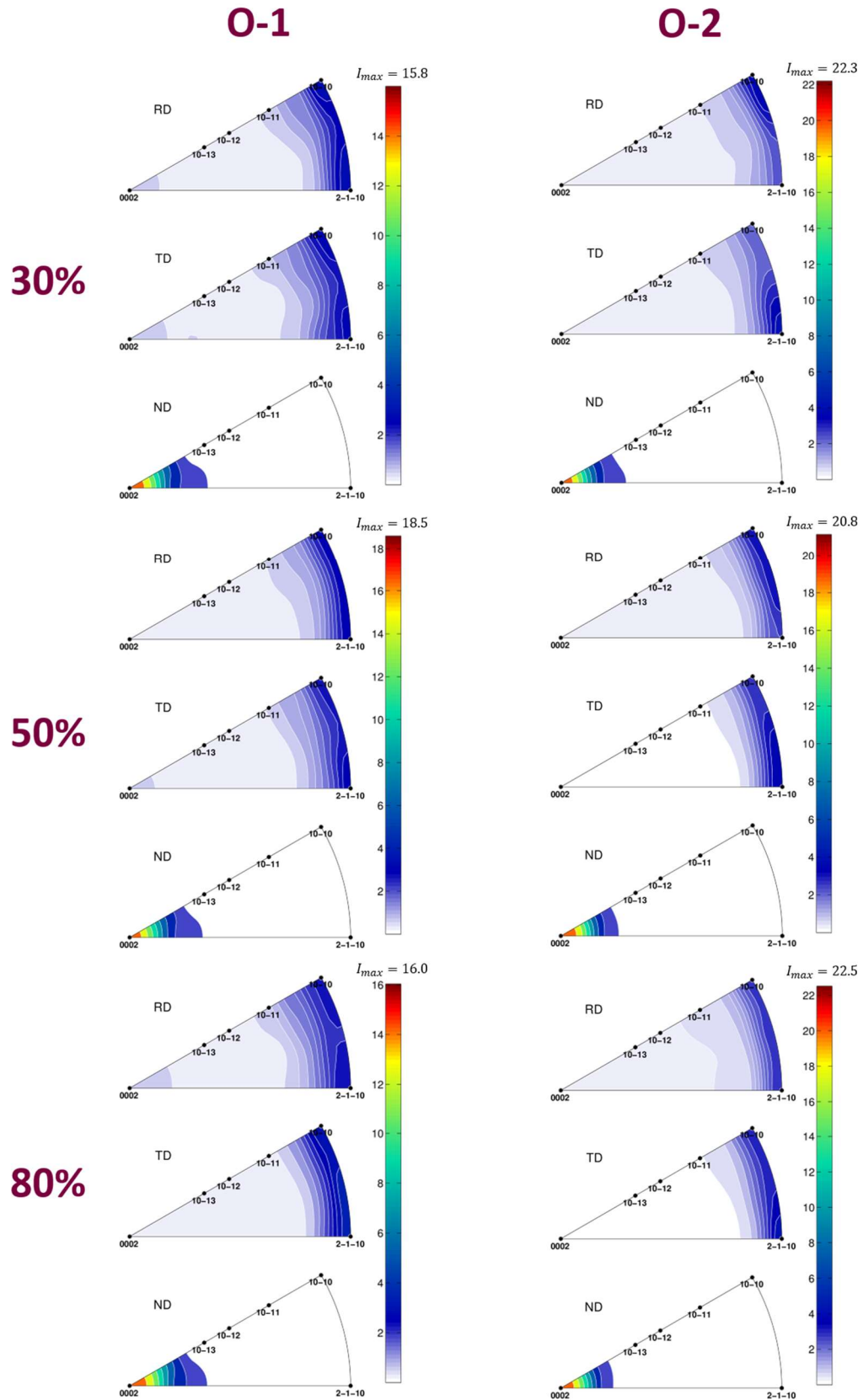


Fig. 4.3. Inverse Pole Figures of magnesium sheets at different strains for both orientations.

According to the microstructure evolution, it is certain that the texture development is strongly associated with the active twin types and subsequent DRX process during rolling, but the deformation response showed no significant alteration of texture features for both orientations, if the initial (30%) and final (80%) values are compared, texture intensity and components remained virtually unaffected with a typical predominant basal texture parallel to ND.

#### **4.7. TWINNING ACTIVITY AND DRX DURING ROLLING.**

In the following section, the microstructure evolution was characterized by EBSD in order to reveal the twin types and DRX mechanisms present during magnesium single crystals rolling. The orientation maps are presented in terms of inverse pole figure coloring with respect to the ND. High angle grain boundaries (HAGBs,  $>15^\circ$ ) were highlighted in black and gray for low angle grain boundaries (LAGBs,  $2-15^\circ$ ). Black areas appearing in Fig. 4.4-9 show remaining zero solutions (non-indexed EBSD patterns) that, in this case, were assigned to highly deformed regions. Noise reduction was carefully applied to improve the original indexing using a minimum of five indexed neighbors. The IPFs from local texture are also presented to correlate the local texture features with those of the x-ray diffraction macrotexture. The types of twins in Table 2.1 and double twins were determined on the basis of their particular misorientation angles and rotation axes [118]. The deviation of angle and axis to identify the twin boundaries was within  $5^\circ$  of the ideal values.

Nowadays, there is a controversy between the researchers on the parameters that affect the twinning activity, some report that the activity of magnesium is negligible at high temperatures [13, 14, 120], others report that the twinning will be found active at high deformation rates independently of temperature [23, 121], while some others associate this activity with large grain sizes [121- 1223]. In the current work the twinning was an important mechanism to accommodate the deformation at high temperature of rolling ( $450^\circ\text{C}$ ), at relative high strain rates ( $2-8\text{ s}^{-1}$ ) and very large grain size (single crystal), this twinning behavior will also be analyzed below.

Fig. 4.4 shows the EBSD results of the interrupted rolling of an O-1 sample at  $\varepsilon = 30\%$ . The original indexing for the mapping was 82% and was improved to 95%. In the map, some twins were observed within the new matrix but any grain with the original orientation was observed, within all the grains many LAGBs were appreciated and tend to pile up in triple junctions. The inverse pole figures show a strong basal texture on the ND with a maximum of 8.46.

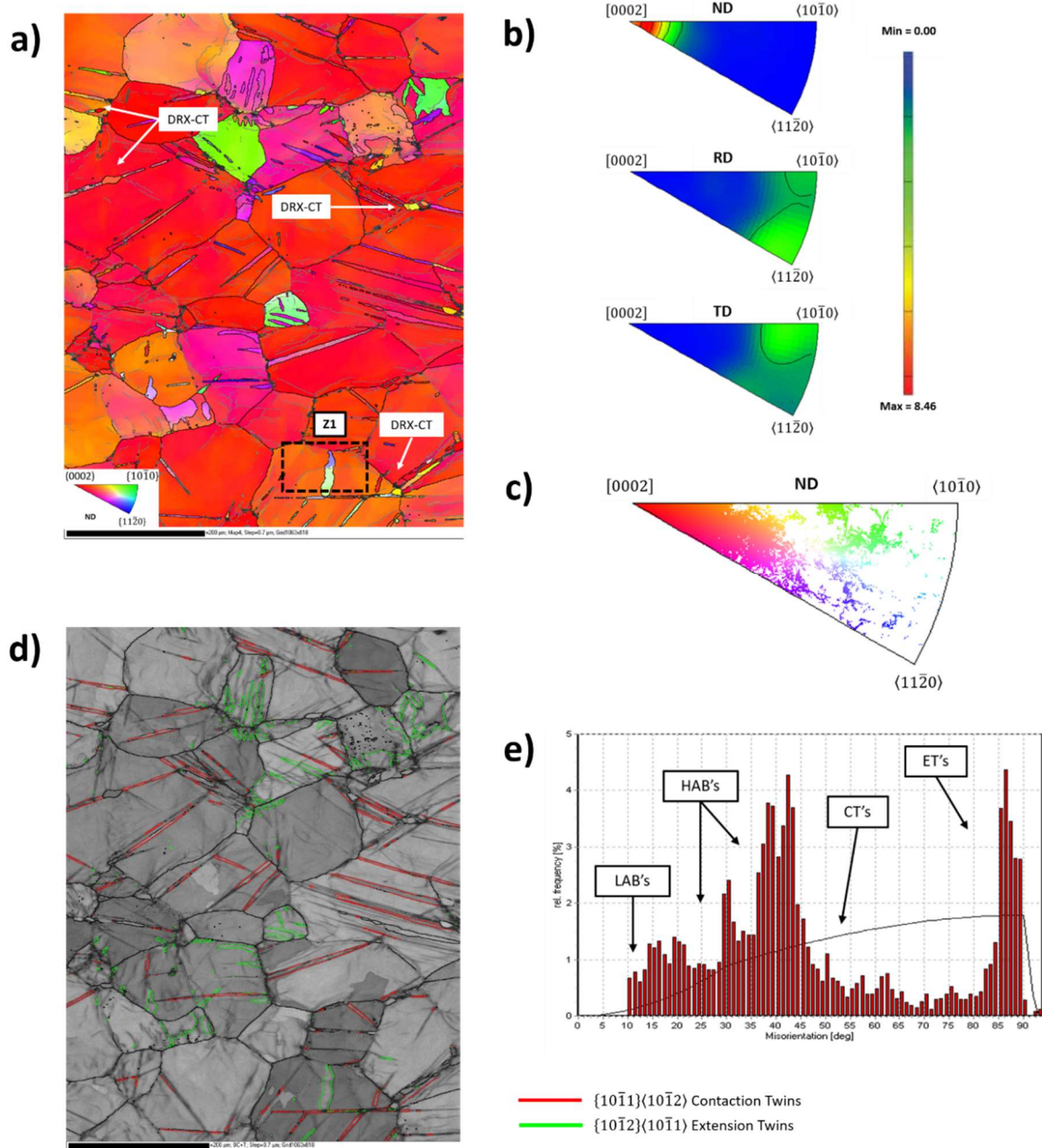


Fig. 4.4. EBSD results obtained from an O-1's specimen at strain of 30% a) EBSD map in inverse pole figure (IPF) coloring relative to ND, b) corresponding IPF's. c) corresponding scattered data ND IPF. d) boundary misorientation map, e) corresponding misorientation angle distribution

Most of the grains with the basal planes perpendicular to ND which being subject to compression on the c-axis, developed compression twins inside, also a oriented grain close to the  $\langle 10\bar{1}1 \rangle$  component was observed, they were subjected to compression almost perpendicular to the c axis, consequently tensile twins were observed inside. However, extension twins inside grains with an orientation close to the  $\langle 2\bar{1}\bar{1}4 \rangle$  (which could be considered favorable for the slip) were observed. Most of the twins are recrystallization-free but some recrystallized twins were also found.

At this strain and  $2.5 \text{ s}^{-1}$ , the microstructure was characterized by basal planes  $\sim 30^\circ$  deviated from the sheet plane (red-orange grains). According to the boundary misorientation map,  $\{10\bar{1}2\}$  extension twins (ETs) and  $\{10\bar{1}1\}$  contraction twins (CTs) were active during the deformation process.

The starting orientation was aligned for  $\{10\bar{1}2\}$  tensile twinning (Schmid factor of 0.37, compression perpendicular to c-axis), blue areas ( $\{11\bar{2}0\}$ ) from this orientation can still be observed but in a very marginal proportion, these areas correspond to  $\{10\bar{1}2\}$  extension twins. This means that the singlecrystal was almost completely rotated by extension twins (ETs) and the red grains now constitute a new matrix wherein contraction twins were favorable owing to c-axis at  $30^\circ$  from ND (Schmid factor of 0.44, compression along c-axis).

The misorientation angle distribution (Fig. 4.4e) shows frequency peaks for low angle ( $<15^\circ$ ) boundaries, as well as high angle boundaries (HAGBs) with distinct peaks close to  $30^\circ$  and  $40^\circ$  attributed to the recrystallized matrix and  $85^\circ$  peak to extension twins. The green and pink grains will be discussed with detail in section 5.1.

The corresponding orientation map and IPF's of O-2 at  $\varepsilon = 30\%$  is presented in Fig. 4.5. The original indexing for the mapping was 78% and was improved to 94%. The inverse pole figure map shows a profuse twinning activity, compared to O-1 the fraction of recrystallized twins is higher. Also, the new matrix has a basal orientation, consequently compression twins were formed inside but any grain with the original orientation was observed.

The IPFs show a strong basal texture on the ND with a maximum of 42.37. Besides, few oriented grains close to the  $\langle 10\bar{1}2 \rangle$  were found, one of them (the biggest) presents tensile twins inside, another grain that presents tensile twins is close to  $\langle 2\bar{1}\bar{1}4 \rangle$  component. Many low angle grain boundaries (LAGBs) were observed within all the grains, even those twins inside, but in this case, they grouped in the center of the grains instead of triple junctions.

The boundary misorientation map (Fig. 4.5d) shows that most of the twins were identified to be  $\{10\bar{1}1\}$  twins, less  $\{10\bar{1}2\}$  twins were also found. In compared to O-1, more contraction twins (CTs) were observed, it can be explained because the basal planes in this orientation were aligned almost parallel to the plane of the sheet (higher  $SF=0.41$  for CTs) due to the rotation by the extension twinning. As the O-1, the O-2 was aligned for extension twinning ( $SF=0.49$ , compression perpendicular to c-axis) but the active variants were slightly different. The initial orientation must be colored in green according to the Standard IPF, but no grains with this characteristic can be appreciated.

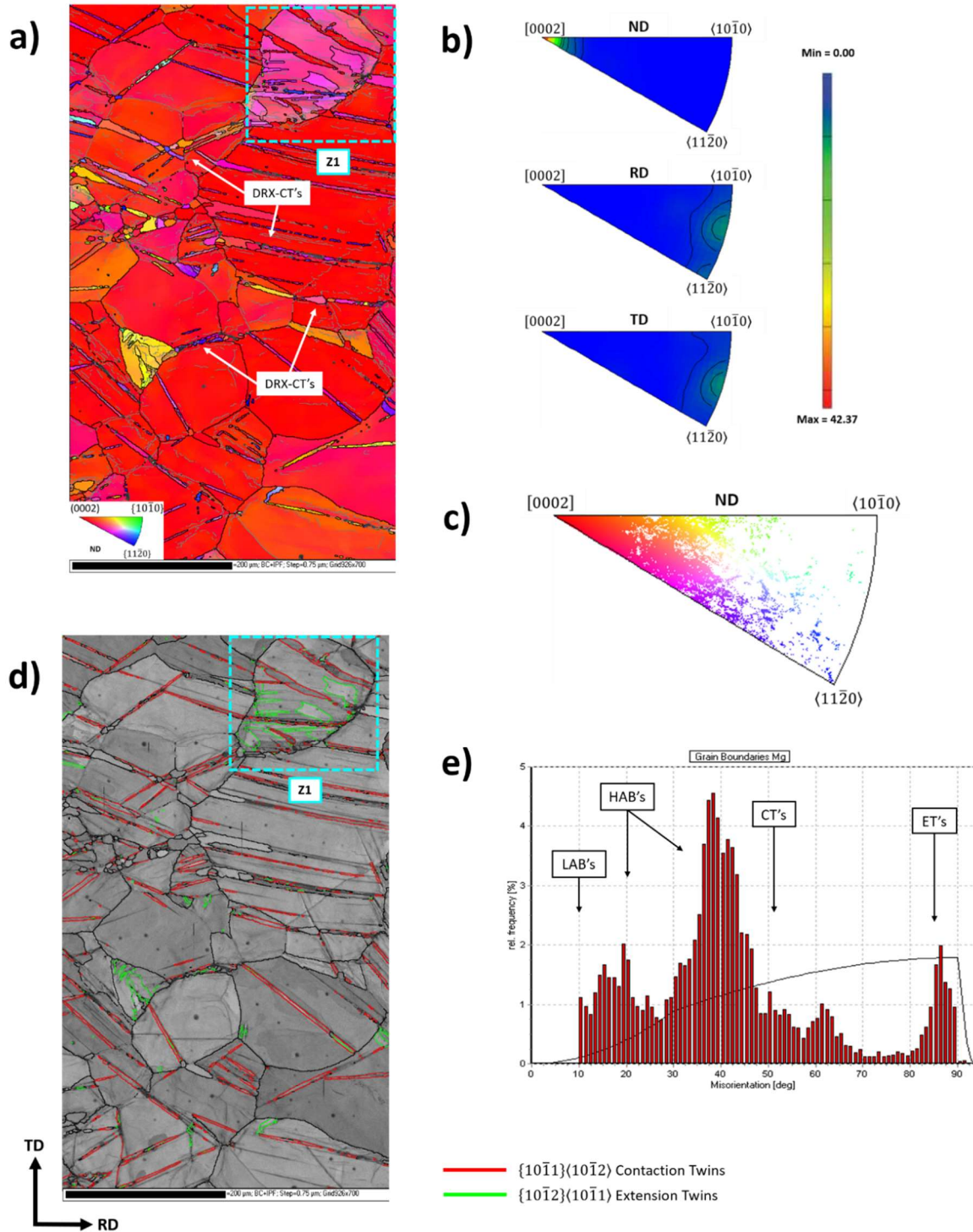


Fig. 4.5. EBSD results obtained from an O-2's specimen at strain of 30% a) EBSD map in inverse pole figure (IPF) coloring relative to ND, b) corresponding IPF's. c) corresponding scattered data ND IPF, d) boundary misorientation map, e) corresponding misorientation angle distribution.

The misorientation angle distribution (Fig. 4.5e) displays frequency peaks for low angle grain boundaries (LAGBs- <math>15^\circ</math>), as well for high angle grain boundaries (HAGBs) close to  $20^\circ$ ,  $40^\circ$  and  $62^\circ$  for recrystallized grains, the  $55^\circ$  peak is attributed to contraction twins (CTs) and  $88^\circ$  for extension twins (ETs).

It is important to note the presence of recrystallized twins since this strain, which gave rise to more and well-defined peaks, by contrast, in the O-1 the twins remained un-recrystallized at this strain. The special case for the extension twinning in the pink grain will be addressed in the next chapter.

At  $\varepsilon = 50\%$  (Fig. 4.6), the O-1 shows thicker twins (some of them were recrystallized) and more low angle grain boundaries (LAGBs) within the grains than those observed at 30%. In spite of the low index ratio in these zones, fine grains can be observed inside the twins derived from a high concentration of plastic deformation within the twins and its subsequent DRX process. A very small group of  $\{10\bar{1}2\}\{10\bar{1}1\}$  twins was found, which largely consumed their parent grain oriented close to the  $\langle 10\bar{1}1 \rangle$  component. It can be observed in the corresponding ND IPF a maximum intensity of 12.14 belonging to the basal component. The original indexing for the mapping was 58% and was improved to 82%.

At this stage with a strain rate of  $4.0 \text{ s}^{-1}$  more and coarser contraction twins were observed, inside them the DRX process was evident. Traces of a green grain consumed by extension twins was observed but as mentioned above this kind of twinning will be addressed in the next section. The misorientation angle distribution (Fig. 5.2d) shows a decrease in the frequency of low angle grain boundaries (LAGBs -  $<15^\circ$ ) and extension twins (ETs -  $85^\circ$ ), compared to 30%, on the other hand the frequency of contraction twins (CTs) and high angle grain boundaries (HAGBs) shows a slight increase.

In the orientation map of O-2 at  $\varepsilon = 50\%$  (Fig. 4.7), some tensile twinned grains oriented close to the  $\langle 10\bar{1}0 \rangle$  component were observed, they can probably be small remnants of the original single crystal. The other grains have a basal orientation and therefore many lenticular  $\{10\bar{1}1\}\{10\bar{1}2\}$  twins were located inside. Unfortunately, the quality of indexing is very low in areas that presumably are partially or completely recrystallized twin bands. The original indexing for the mapping was 68% and was improved to 91%.

Another characteristic of the microstructure is the division of the grains by low angle grain boundaries (LAGBs). Within the grains with a basal orientation, this phenomenon is more evident, however, it can be observed in all the grains even within twins. It is also possible to observe a grain with tensile and contractions twins inside, most of the grain has a basal orientation, which suggests that the  $\{11\bar{2}0\}$  twins consumed almost completely the parent grain with orientation close to  $\langle 10\bar{1}0 \rangle$  and then this new basal matrix developed contraction twins. The ND IPF describes a strong basal texture with a maximum of 13.22, while the  $\langle 10\bar{1}0 \rangle$  direction tends to be parallel to the RD and  $\langle 11\bar{2}0 \rangle$  to the TD.

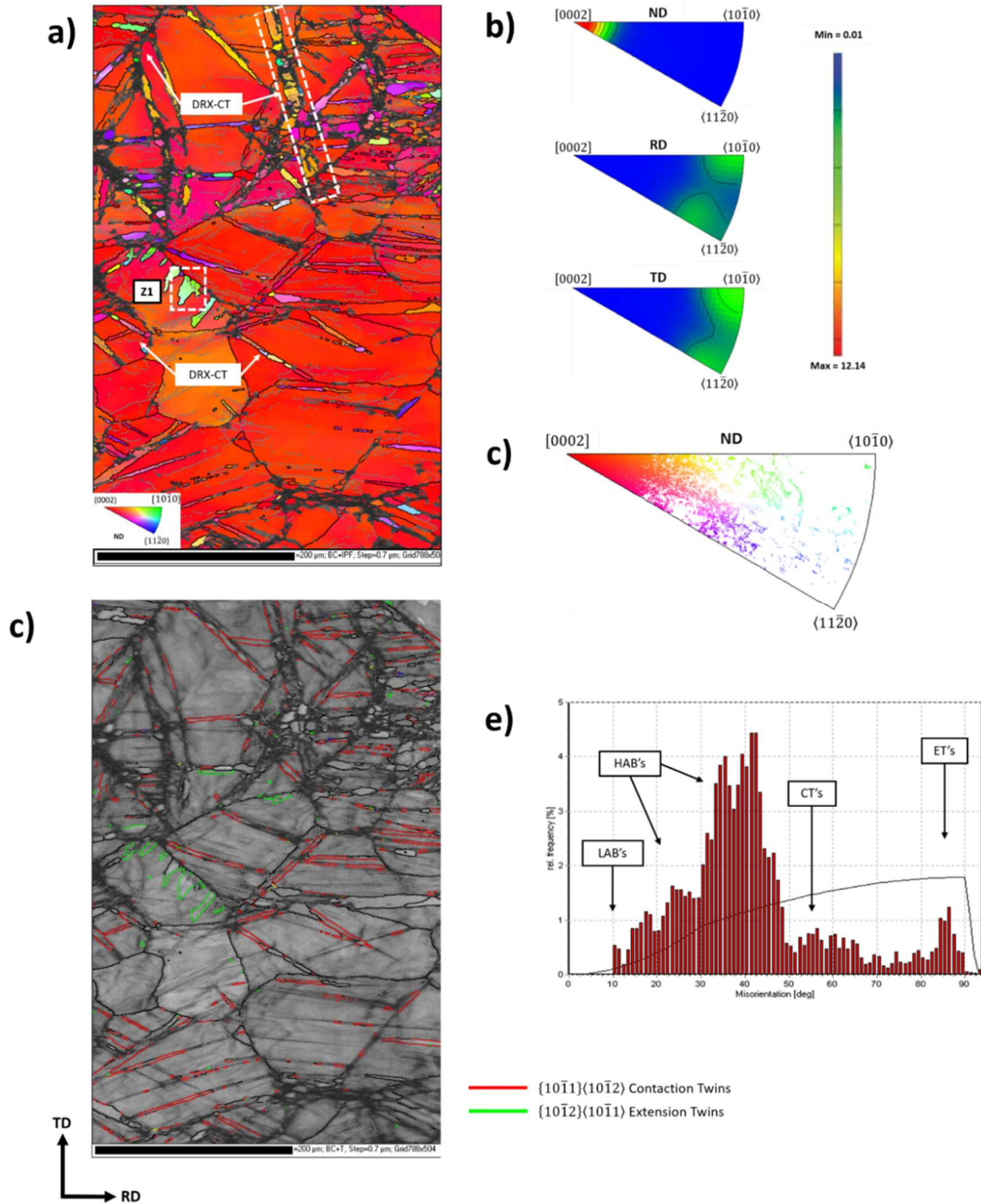


Fig. 4.6. EBSD results obtained from an O-1's specimen at strain of 50% a) EBSD map in inverse pole figure (IPF) coloring relative to ND, b) corresponding IPF's. c) corresponding scattered data ND IPF, d) boundary misorientation map, e) corresponding misorientation angle distribution

At  $\varepsilon = 50\%$  and  $4.0 \text{ s}^{-1}$ , contraction twins (CTs) inside red grains (0002) were observed, indications of recrystallized contraction twin bands (DRXed TBs) can be observed close to the zero-resolution zones, indicating a high strain inside them. Traces of two green grains (initial orientation) almost consumed by extension twins (ETs) were observed.

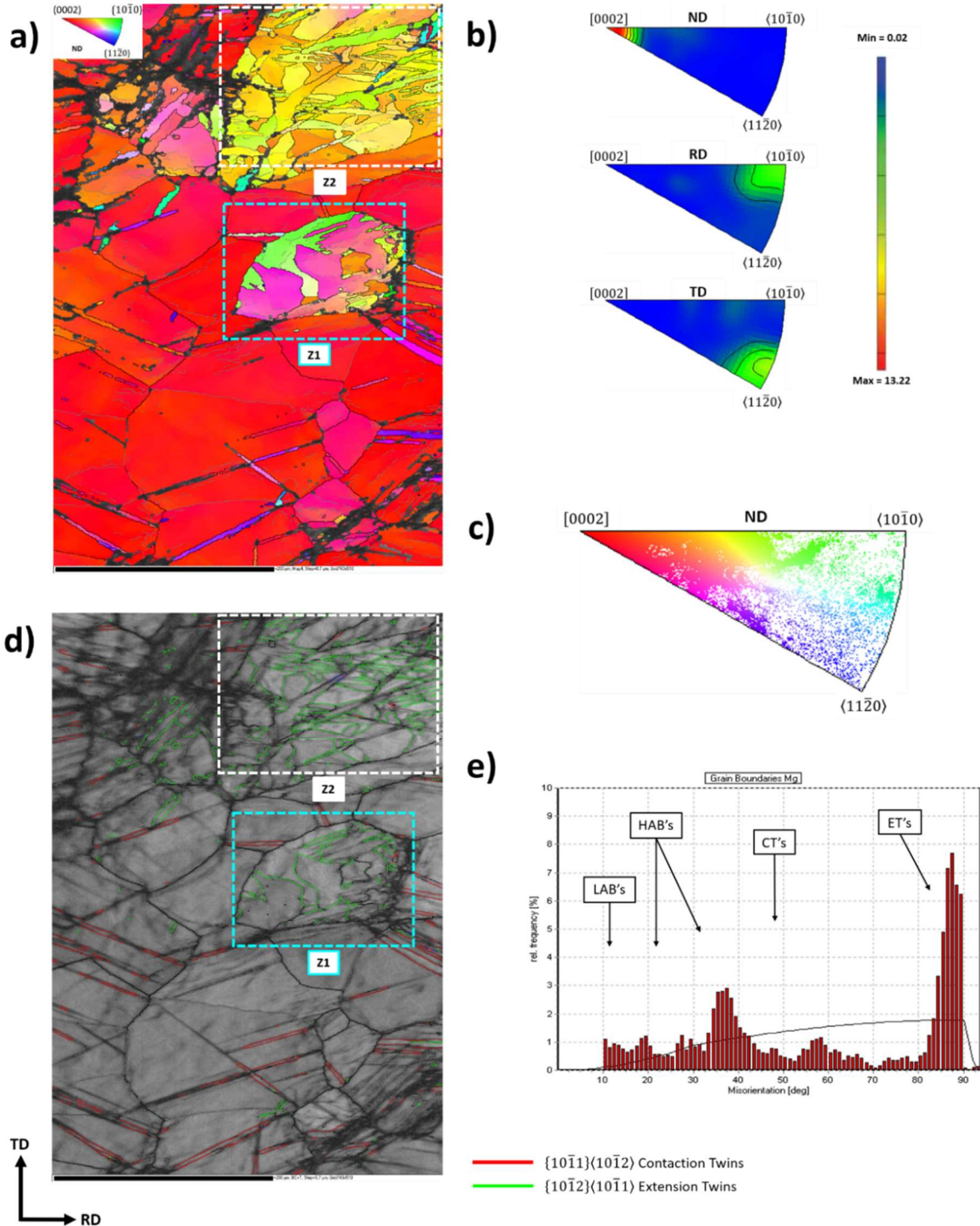


Fig. 4.7. EBSD results obtained from an O-2's specimen at strain of 50% a) EBSD map in inverse pole figure (IPF) coloring relative to ND, b) corresponding IPF's. c) corresponding scattered data ND IPF, d) boundary misorientation map, e) corresponding misorientation angle distribution

The misorientation angle distribution (Fig. 4.7e) shows the same peaks 30%, but the frequency decrease for all of them except by extension twins (ETs), but it is associated with the analyzed zone and not with any recrystallization phenomenon.



The Fig. 4.8 shows EBSD map for O-1 at  $\varepsilon = 80\%$  and corresponding IPF's. The original indexing for the mapping was 87% and was improved to 99%. The microstructure is not homogenous, a typical bimodal microstructure consisting of fine and coarse grains was observed. The coarse grains belong to the basal matrix observed in the previous strains. On the other hand most of the fine grains were originated by the DRX process inside the twins, some recrystallized grains with twin-like shape can still be observed. Virtually, all grains have a basal orientation or very close to it, which is reflected in the ND IPF which has a maximum intensity of 8.98 in the basal component.

However, some grains near to  $\langle 10\bar{1}1 \rangle$ ,  $\langle 10\bar{1}3 \rangle$ ,  $\langle 2\bar{1}\bar{1}1 \rangle$ ,  $\langle 2\bar{1}\bar{1}2 \rangle$  and  $\langle 2\bar{1}\bar{1}4 \rangle$  components can also be observed, although in a much smaller proportion, so much so that these components are not reflected in the IPF. As in the other stages the formation of low angle grain boundaries (LAGBs) was very evident, especially in the coarse grains. A pair of tensile and contraction twins could be found, one of them seems to still retain a small part of the original single crystal ( $\langle 2\bar{1}\bar{1}4 \rangle \parallel ND$ ).

At  $\varepsilon = 80\%$  and  $8.0 \text{ s}^{-1}$ , the orientation maps do not show twinning activity (Fig, 4.8), in spite of the same temperature of deformation, a similar texture and just a slight higher strain rate compared to 30% and 50%, but a evident smaller grain size, demonstrating a greater susceptibility of the twinning to the grain size than to other parameters.

Finally, the O-2 at strain of 80% (Fig, 4.9) presents recrystallized twin bands, leading to grains with orientations slightly deviated from  $\langle 10\bar{1}0 \rangle$ ,  $\langle 10\bar{1}1 \rangle$ ,  $\langle 10\bar{1}2 \rangle$ ,  $\langle 2\bar{1}\bar{1}0 \rangle$  and  $\langle 2\bar{1}\bar{1}4 \rangle$  components. These bands could also be grains elongated by deformation, since they were observed parallel to the RD, however due to their morphology (some bands are almost perpendicular to the RD) and what was observed in previous strains (30 and 50%), were considered as recrystallized twins. There is still a prominent matrix with a basal orientation, which has many LAGBs, but any original twins could find inside. This means that all or almost all the twins grew and recrystallized. But in this case these grains recrystallized in random orientations, if more deformation were applied, perhaps this would cause the formation of twins within the basal matrix, its subsequent recrystallization would give rise to a random texture.

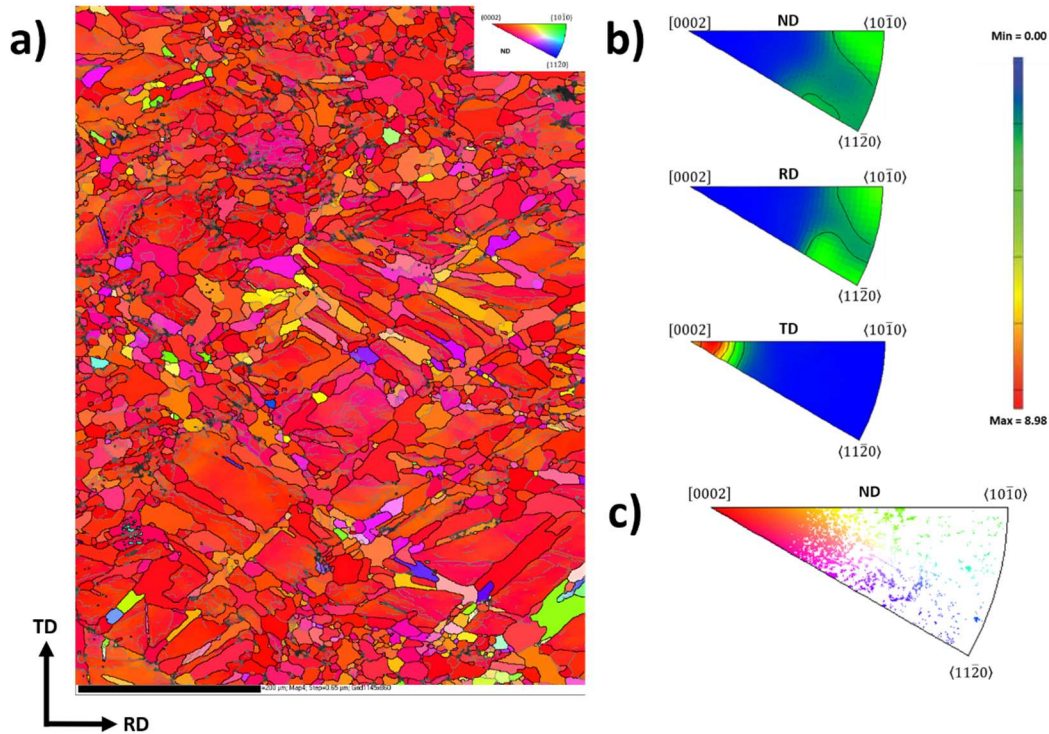


Fig. 4.8. EBSD results obtained from an O-1's specimen at strain of 80% a) EBSD map in inverse pole figure (IPF) coloring relative to ND, b) corresponding IPF's. c) corresponding scattered data ND IPF.

The corresponding IPFs show a strong basal component in the ND with a peak value of 20.20. The original indexing for the mapping was 87% and was improved to 99%.

At  $\varepsilon = 80\%$  and  $8.0 \text{ s}^{-1}$  the deformation was accommodated without twinning as it happened in the O-1. In this case there was not a grain refinement, the recrystallized twin bands (DRXed TBs) were coarser and show grains with a large spread orientation (away from basal orientation) allowing the basal slip and subsequent localized strain.

Both orientations do not present twin morphologies, in spite of having been converted into a new basal orientation matrix by the extension twins, instead it presents a polygonal grains morphology, bringing out dislocation slip inside this new matrix was necessary for subsequent DRX at the first rolling steps. The presence of more high angle grain boundaries in O-1 than O-2 after the conversion by extension twinning, possibly acted as nucleation sites for  $\{10\bar{1}1\}$  contraction twins followed by its recrystallization (see section 5.1.2). It is worth to note that in all the misorientation angle distribution there is a pick close to  $40^\circ$ , which correspond to the grains produced post tensile twinning reorientation.

Based on the above observation, it can be inferred that  $\{10\bar{1}2\}\langle 10\bar{1}1\rangle$  twinning with various variants was responsible for the consumption and reorientation of original single crystal, facilitating the formation of  $[0002]$  component at the early stage of rolling, where a profuse  $\{10\bar{1}1\}\langle 10\bar{1}2\rangle$  twinning took place, and its immediate recrystallization generated new grains with orientations close to the basal (O-1) or relatively random (O-2).

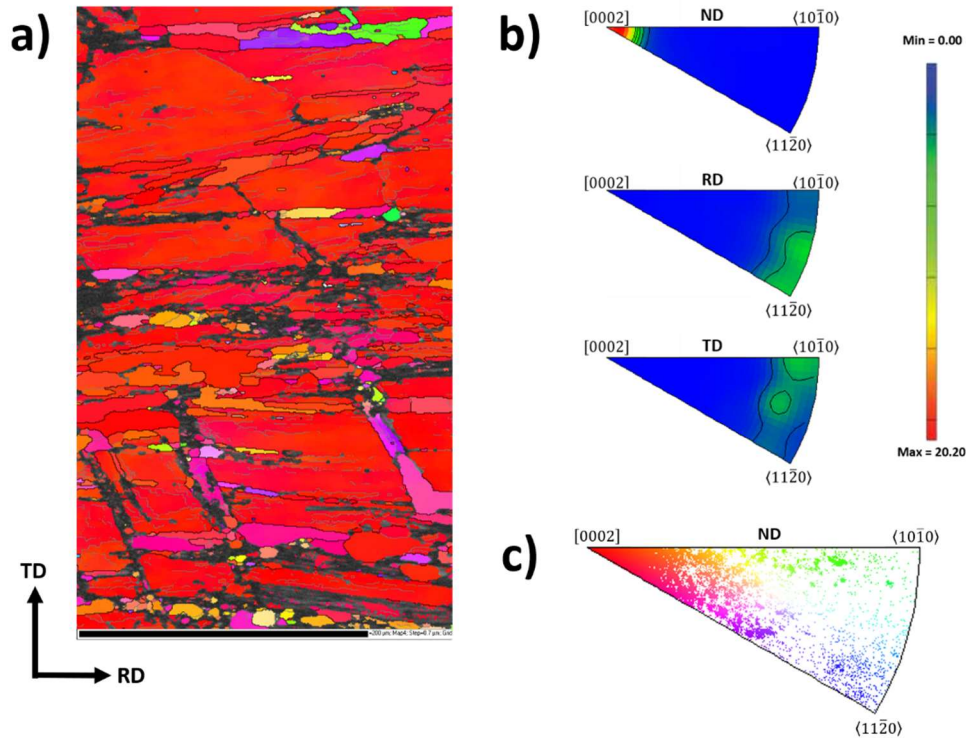


Fig. 4.9. EBSD results obtained from an O-2's specimen at strain of 80% a) EBSD map in inverse pole figure (IPF) coloring relative to ND, b) corresponding IPF's. c) corresponding scattered data ND IPF.

#### 4.8. MICROSTRUCTURE POST ANNEALING TREATMENT.

Post rolling at  $\varepsilon = 80\%$ , the specimens were subjected to annealing treatment at  $400^\circ\text{C}$  for 30 min followed by very slow cooling inside the furnace. With respect to the annealing microstructures, both orientations exhibit a bimodal microstructure, consisting of coarse grains and fine grains (Fig. 4.10), i.e. some grains appeared to have grown at a higher rate relative to their neighbors. Grain growth seemed to be slightly restricted in the O-1, whereas in the O-2 the growth advantage of selective grains over others became more evident, reaching larger grain size.

Additional larger metallographs, comprising of a reconstruction of microstructure by joining several micrographs, were used to yield statistically enough data in the grain size measurements by interception lineal method and presented in Appendix E. The number of detected grains were 262 and 322 grains and the average grain sizes were  $\sim 130 \mu\text{m}$  vs  $\sim 185 \mu\text{m}$  for O-1 and O-2 respectively. It is worth mentioning that the O-2, in addition to presenting a greater grain growth, also presents the most heterogeneous microstructure with areas of much finer grains ( $\sim 10 \mu\text{m}$ ) and much thicker ( $\sim 500 \mu\text{m}$ ) than those of the O-1. This feature is more evident in the Fig. E.2 but it is also possible to appreciate it in Fig. 4.10.

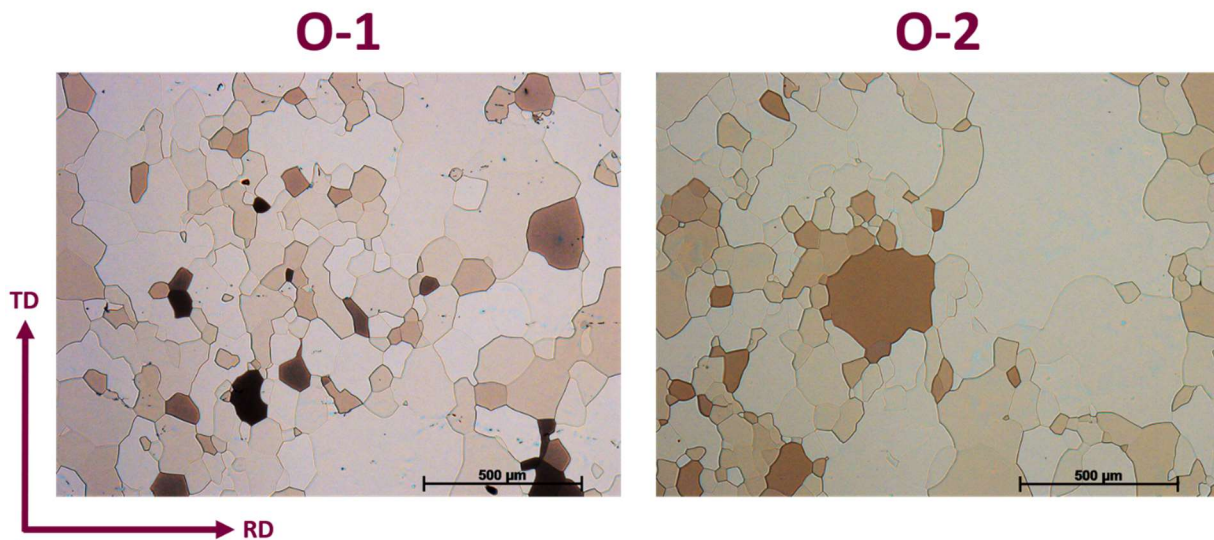


Fig. 4.10. O-1 and O-2 microstructures after annealing at  $400^\circ\text{C}$ .

Figures 4.11 and 4.12 present the EBSD orientation maps and local texture data of O-1 and O-2 annealed at  $400^\circ\text{C}$ . Both were measured at same magnifications for a better comparison of the microstructure development and grain size. The original indexing for both mappings was between 96% and 98%. Both maps show fully recrystallized microstructures that have already undergone grain growth, the presence of very fine grains around the coarse grains can be appreciated, which shows the preferential growth of certain grains that absorb the grains that surround them. In the case of O-1, the low angle grain boundaries (LAGBs) to high angle grain boundaries (HAGBs) transition of many fine grains can still be seen with clarity. On the other hand in the O-2 most of the fine grains have been absorbed by the coarse grains due to accelerated grain growth kinetics in the latter. The IPFs of both orientations show a stronger O-2 basal texture, with 18.75 MRD vs 8.46 MRD for O-1.

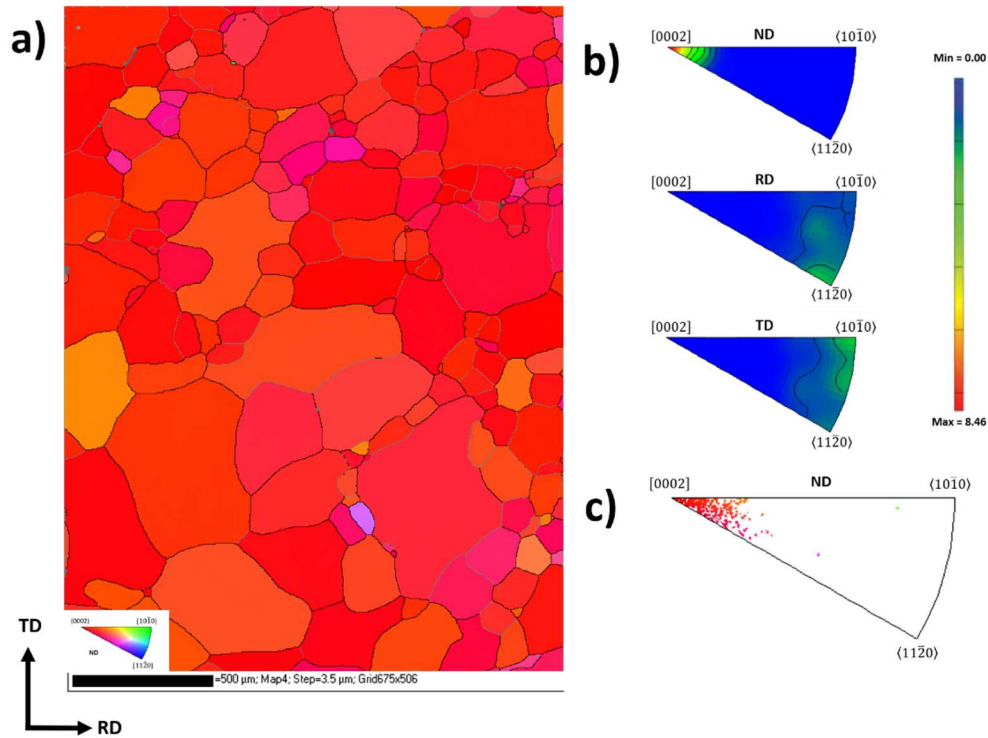


Fig. 4.11. EBSD results obtained from an O-1's specimen after annealing treatment a) EBSD map in inverse pole figure (IPF) coloring relative to ND, b) corresponding IPF's. c) corresponding scattered data ND IPF.

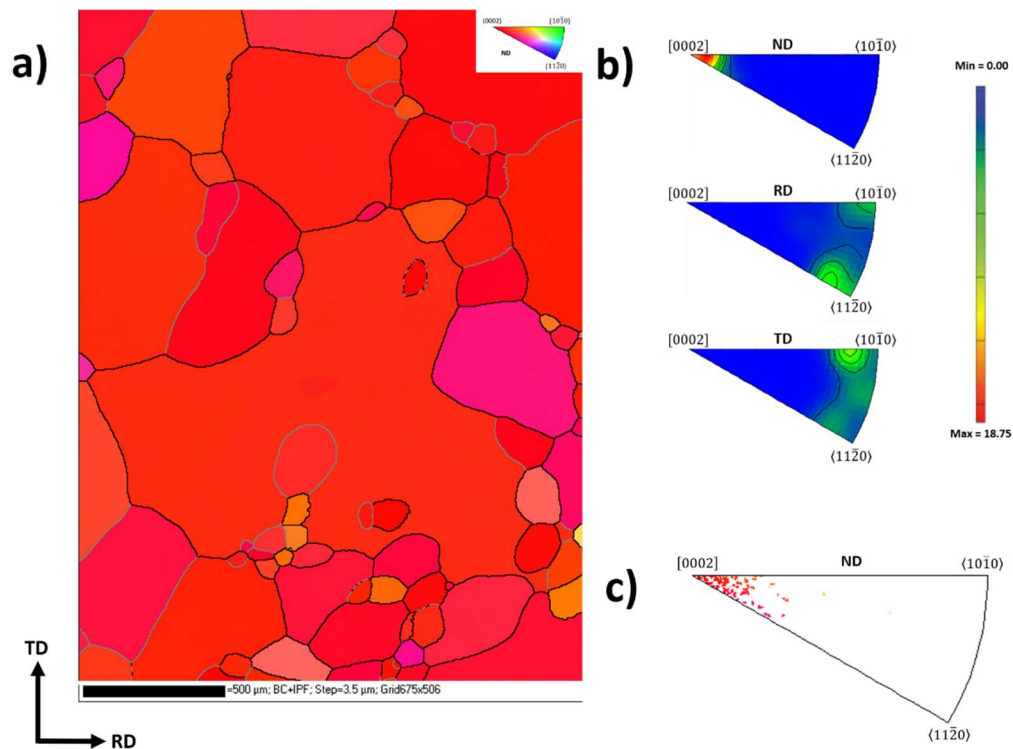


Fig. 4.12. EBSD results obtained from an O-2's specimen after annealing treatment a) EBSD map in inverse pole figure (IPF) coloring relative to ND, b) corresponding IPF's. c) corresponding scattered data ND IPF.

# Discussion

## 5.1. $\{10\bar{1}2\}$ TWINNING AND ITS INFLUENCE ON THE BASAL TEXTURE.

In the current work,  $\{10\bar{1}2\}$  twinning was extremely active and was responsible for the formation of the basal texture since the first rolling steps. The activation of  $\{10\bar{1}2\}$  twin variants depends on the strain path, compression perpendicular to the c-axis or tension parallel to the c-axis [121-123], and their activity is governed by the Schmid law, the twin variant with the higher Schmid Factor (SF) takes place favorably [124-126]. Therefore, in the following, the  $\{10\bar{1}2\}$  twinning behavior was analyzed with respect to the loading and crystal orientation at the early stage of rolling and discussed its corresponding effect on the evolution of grain orientation.

Under rolling, the initial single crystals with the c-axis parallel to the RD were favorably aligned for  $\{10\bar{1}2\}$  twinning (compression perpendicular to the c-axis). Theoretically,  $\{10\bar{1}2\}$  twinning is possible on six equivalent twin variants, six  $\{10\bar{1}2\}$  twinning planes and six  $\langle 10\bar{1}1 \rangle$  shear directions  $(10\bar{1}2)$   $[\bar{1}011]$ ,  $(01\bar{1}2)$   $[0\bar{1}11]$ ,  $(\bar{1}102)$   $[1\bar{1}01]$ ,  $(\bar{1}012)$   $[10\bar{1}1]$ ,  $(0\bar{1}12)$   $[01\bar{1}1]$  and  $(1\bar{1}02)$   $[\bar{1}101]$  [126-128].

Figure 5.13a-b shows basal pole figures depicting the calculated  $\{10\bar{1}2\}$  extension twin orientations for the initial specimen orientations 1 and 2. By the deformation  $\{10\bar{1}2\}$  twins would gradually consume its parent grain (single crystal) and reoriented it by  $\sim 86.3^\circ$  with basal planes 'parallel' to the RD since early stage of deformation contributing to the formation of the basal texture but by two very different ways:

For O-1,  $(01\bar{1}2)[0\bar{1}11]$ ,  $(1\bar{1}02)[\bar{1}101]$ ,  $(\bar{1}102)[1\bar{1}01]$  and  $(0\bar{1}12)[01\bar{1}1]$  variants have a SF value of 0.37 (Fig. 5.1a), making them equally active considering the Schmid law, these twin variants transformed the matrix into twin orientations with the *c*-axis aligned at an angle of 30° from ND (Fig. 5.5c). These orientations have a non-zero Schmid factor for basal, prismatic and pyramidal slip, but twinning continues to have the higher SF.

On the other hand, regarding O-2 only  $(10\bar{1}2)[\bar{1}011]$  and  $(\bar{1}012)[10\bar{1}1]$  variants have a SF=0.49 (Fi. 5.1b), laying the basal plane almost parallel to the sheet plane which strengthened the basal texture (Fi. 5.1d) converting the initial matrix into a 'hard' orientation, in which, slip was naturally suppressed. As a result of this reorientation, the basal intensity in the O-2 was higher than O-1 (Fig. 5.1e-f). The aforementioned is in total agreement with [29,32], in these works the specimens under plane strain compression (PSC) with the starting orientation D (O-2) were again almost single-crystalline with only low angle grain boundaries present after the conversion of the initial matrix by twinning.

A slight broadening in the basal component close to the ND on O-1 caused by the initial components for  $(10\bar{1}2)[\bar{1}011]$  and  $(\bar{1}012)[10\bar{1}1]$  variants corroborates that active twin variants in this orientation accommodated the basal plane ~30° rotated from the sheet plane. In fact, in Appendix D, it can still be noticed on the O-1's (0002) pole figure of sample 1 a double-peak basal component close to ND, originated by two picks of twins (Fig. 5.5a), which subsequently turned into a single sharper component due to rotation caused by the basal slip (*c*-axis towards load direction).

For the green and pink grains in Fig. 5.1a the only possible explanation that gives origin to this orientations is a sequence of 3 extension twinning: primary (PET), secondary (SET) and tertiary (TET) extension twinning. First (primary extension twins), the O-1 (blue) is rotated by  $(01\bar{1}2)[0\bar{1}11]$ ,  $(1\bar{1}02)[\bar{1}101]$ ,  $(\bar{1}102)[1\bar{1}01]$  and  $(0\bar{1}12)[01\bar{1}1]$  variants to a new orientation with the basal plane ~30° rotated from the sheet plane as above mentioned (red-magenta grains). In this new orientations contraction twins should be the preferential deformation mechanism because the *c*-axis was partially aligned to load direction (SF=0.49 for  $(10\bar{1}1)[\bar{1}012]$  and SF=0.44 for  $(01\bar{1}1)[1\bar{1}02]$ ,  $(1\bar{1}01)[\bar{1}102]$  twin variants).

Nevertheless, an exhaustive analysis of this Schmid Factors (SF) reveals the following extension twin variants  $(\bar{1}102)[1\bar{1}01]$ ,  $(0\bar{1}12)[01\bar{1}1]$  have a SF=0.43 and  $(01\bar{1}2)[0\bar{1}11]$ ,  $(1\bar{1}02)[\bar{1}101]$  have a SF=0.41, therefore extension twinning would not be unreasonable. This secondary extension twinning laid the prismatic plane slight deviated from the RD-TD plane (green grains), such orientation (same to O-2) is favorable for extension twinning (described above) leading to red orientations (TET).

For O-2, the origin of the pink and yellow grains (Fig. 5.3a and 5.4a) is easier to understand, some traces of green grains can still be recognized, in yellow and pink grains, it means the initial orientation (green) was rotated to yellow or pink orientations by  $(01\bar{1}2) [0\bar{1}11]$ ,  $(1\bar{1}02) [\bar{1}101]$ ,  $(\bar{1}102) [1\bar{1}01]$  and  $(0\bar{1}12) [01\bar{1}1]$  besides its low SF=0.12, y could be associated to a lattice rotation caused by prismatic slip, a very small rotation is necessary to significantly increase the value of the SF, it can be reasonable because prismatic slip posses a SF=0.43 in the initial orientation (O-2, which is not the stable orientation) [24].

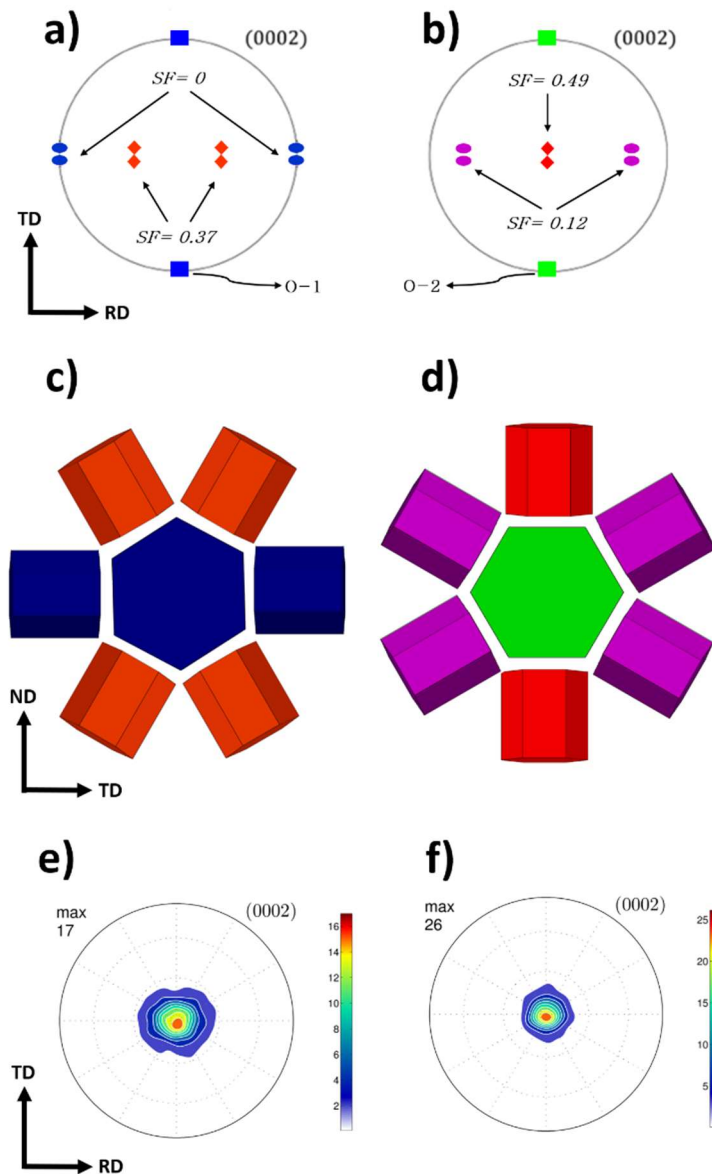


Fig. 5.1. (0002) PF showing the initial orientations a) O-1 and b) O-2 as well as their corresponding  $\{10\bar{1}2\}$  extension twin variants. Schematic representation of active twin variants for a) O-1 and b) O-2. Recalculated (0002) PF at  $\epsilon=30\%$  for e) O-1 and f) O-2.



### 5.2. SHEAR LOCALIZATION ON $\{10\bar{1}1\}$ TWINS AND THEIR INFLUENCE ON THE DRX BEHAVIOR.

Fig. 5 shows the EBSD results of the interrupted rolling at 30% and 50% for both orientations. Bands of  $\{10\bar{1}1\}$  contraction twins extended through the samples, these contraction twin bands became wider at  $\varepsilon = 50\%$  and were recrystallized in the case of O-1, conversely, twin bands recrystallized since  $\varepsilon = 30\%$  in O-2.

The microstructure comprised bands of fine recrystallized grains embedded in a 'hard' basal orientation matrix (*c*-axis nearly parallel to ND). It has been widely reported that  $\{10\bar{1}1\}$  contraction twins act as effective nucleation sites for DRX due to the high internal strain accumulation within them and difficult mobility of the twin boundaries, which is referred as twin-induced dynamic recrystallization mechanism [25, 87, 120-124].

The dynamic recrystallization induced by twin implies slip inside twins, leading to localized shear within contraction twin bands attributed to much easier conditions for plastic flow inside the band as opposed to the 'hard' matrix. This accumulation of (plastic) strain energy in a rather small volume produced extensive dynamic recovery in these areas, i.e. continuous dynamic recrystallization (CDRX), characterized by a progressive rotation of sub-grains formed during deformation until their boundary misorientations become sufficiently large to be considered as high angle grain boundaries [25].

Recent works [128, 129] found that recrystallized grains formed as result of twin-induced dynamic recrystallization were rotated around the *c*-axis of their parent twin by  $\sim 30^\circ$ . When these grains are deformed, they become scattered from the parent twins and acquire a definitive non-basal orientation [130]. Nevertheless, the grains that nucleate inside  $\{10\bar{1}1\}$  twins generally cannot grow outside the twin boundaries so the efficacy of twin-induced dynamic recrystallization mechanism on the final texture weakening is limited [121-122].

This exhibits good agreement with the observed results in the current study, the formation of  $\{10\bar{1}1\}$  twins was observed but twin-induced recrystallized grains with non-basal orientation were not intensive enough to change the final formation basal component (Fig. 4.3). However, it is very likely that at low temperatures and higher deformation speeds (higher thickness reduction applied per rolling pass) high density of twins induced by rolling provide sufficient nucleation sites for recrystallization to alter the final texture [123-124].

From the results shown in Fig. 5.6 it is evident that the highly deformed shear bands nucleate a wide spectrum of recrystallization orientations. The formation of high angle grain boundaries with a misorientation angle of about  $30^\circ$ , according to the misorientation angle distributions, is associated with a shift of orientations from the second type  $\langle 11\bar{2}0 \rangle$  to the first type  $\langle 10\bar{1}0 \rangle$  prismatic fiber owing to the rotation of grains around their  $c$ -axes within their respective  $\{10\bar{1}1\}$  twin bands.

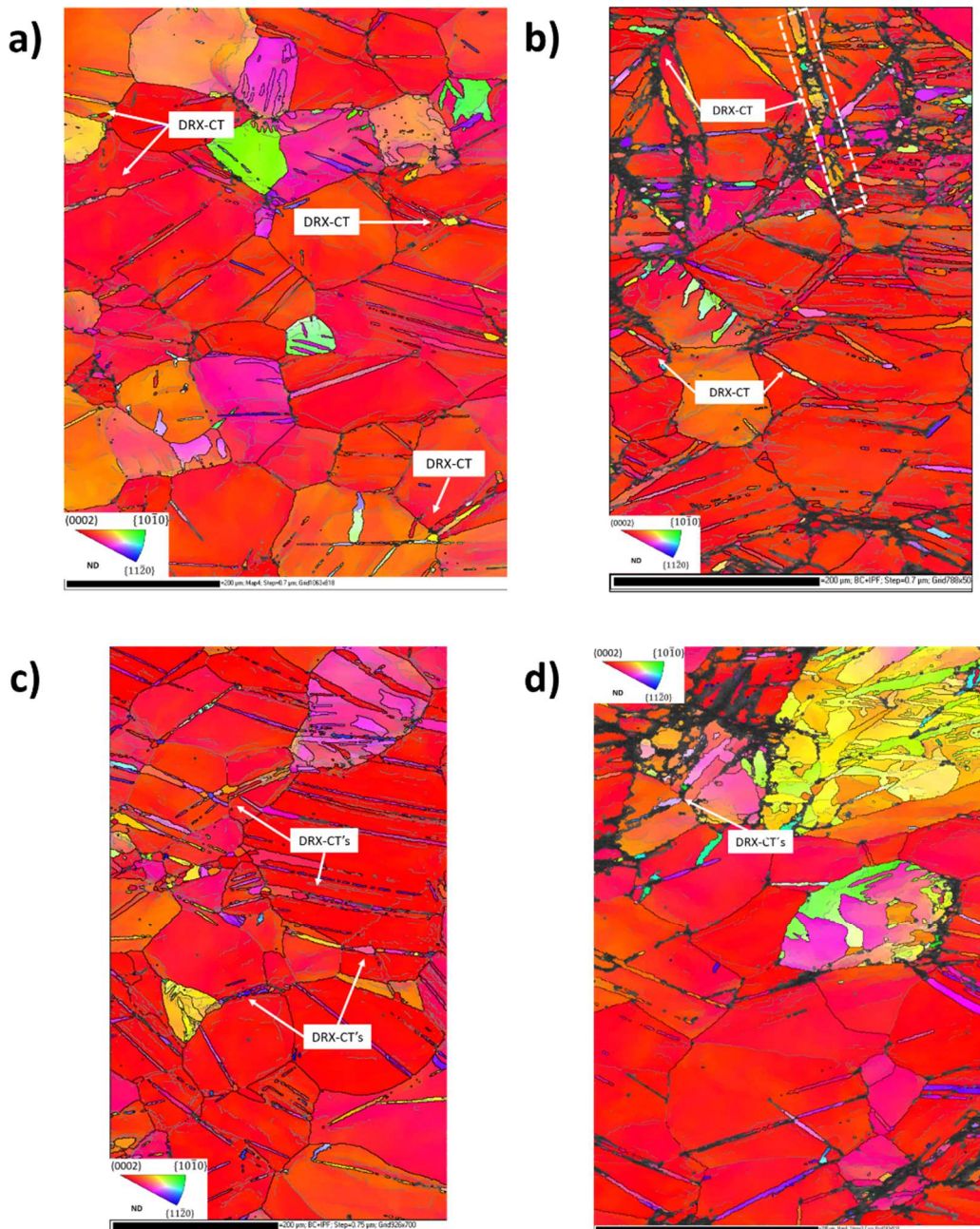


Fig. 5.2. Orientation maps in ND IPF coloring shows DRXed twin bands due strain localized inside CT's. For O-1 a)  $\epsilon = 30\%$ , b)  $\epsilon = 50\%$  and O-2, c)  $\epsilon = 30\%$ , d)  $\epsilon = 50\%$ .

According to the above, prismatic slip must play a crucial role in the formation of new grains ( $SF=0.433$  inside contraction twins), since the grains in the interior band were rotated around the  $c$ -axis of the parent twin (grains colored from yellow to pink). While basal slip causes a rotation towards the CD, prismatic slip entails a rotation of the lattice around the  $c$ -axis [29-31, 134]. Previously, prismatic slip has been reported to operate exclusively above  $180\text{ }^{\circ}\text{C}$  [30]. Reed-Hill and Robertson reported the activation of prismatic slip at  $25\text{ }^{\circ}\text{C}$  and  $-190\text{ }^{\circ}\text{C}$  [31]. Prismatic slip was apparently activated under conditions of extensive localized shear inside  $\{10\bar{1}1\}$  twin bands as in the current case. [26, 27]

It is also of particular interest to note that the recrystallized grains were obviously deformed exclusively by crystallographic slip because there were no twins present inside those newly formed grains, proving the influence of  $\{10\bar{1}1\}$  twin induced DRX mechanism on the 'weakening' of basal texture. Future studies are required to find the correct parameters to cause extensive  $\{10\bar{1}1\}$  twinning and subsequent nucleation of non-basal orientation grains.

### 5.3. DRX MECHANISMS DURING HOT ROLLING.

Dynamic recrystallization (DRX) is typically expected to operate at elevated temperatures regardless of its nature. Since DRX generates new orientations, it can play a key role in avoiding the formation of a basal texture through randomization as long as the orientation change is not limited to a simple rotation around the  $c$ -axis, i.e. there are a high number of grain boundaries with random misorientation axes [125].

In the current work, the microstructure developed continuously as a result of DRX after twinning during rolling. Detailed EBSD observation revealed that continuous (CDRX) and discontinuous (DDRX) recrystallization operated with different effect on the selection of recrystallized grain orientations. In the following, we discussed such DRX mechanisms in detail, as well as their corresponding effect on the nucleation of new orientations.

Compared to CDRX, DDRX has clear grain nucleation and growth stages. The DDRX mechanism is closely related to strain-induced boundary migration that involves the bulging of part of pre-existing high angle grain boundaries (HAGBs), leaving a region behind the migration boundary with a lower dislocation content [103], i.e., it depends on the dislocation density difference and stored energy difference across the boundary [126]. Usually, low angle grain boundaries (LAGBs) result from accumulated dislocations and/or formation of sub-grains in the deformed structure [127, 128].

Fig. 5.7 shows the EBSD results of the interrupted rolling at  $\varepsilon = 30\%$  for a) O-1 and b) O-2. Examination of the inverse pole figure map of O-1 and O-2 indicated that DDRX had begun with finer recrystallized grains and sub-grains formed at triple junctions. The LAGB's within the grains, indicate that dislocations were also quite active in addition to the twinning and revealing the coexistence of CDRX and DDRX. In both orientations the presence of recrystallized twins was evident, this kind of recrystallization was addressed in the section 5.1.

The cyan boxes point sub-grains boundaries (sub-GBs) arrangements that presumably became into high angle grain boundaries (HAGBs), based on the small recrystallized grains also observed in the triple junctions and pointed by the yellow boxes, sustaining the occurrence of DDRX.

On the other hand, evident nets of low angle grain boundaries (LAGBs) were observed within the grains (green boxes). Its subsequent transformation to high angle grain boundaries (HAGBs) can be confirmed by the misorientation line profiles of the lines that cross these zones (black arrows), which show a misorientation of up to  $14.5^\circ$  (L1) for O-1 and  $13.5^\circ$  (L1) for O-2, i.e., these LAGB's have almost become in HAGB's, delating a CDRX process.

It is worth to note in O-2 DDRX is less obvious than O-1, this could be attributed to the presence of greater number of dislocations in the latter, since the initial orientation O-2 was turned into a 'hard' orientation matrix by the extension twinning while the O-1 was reoriented to favor the basal slip. (See section 5.1.1).

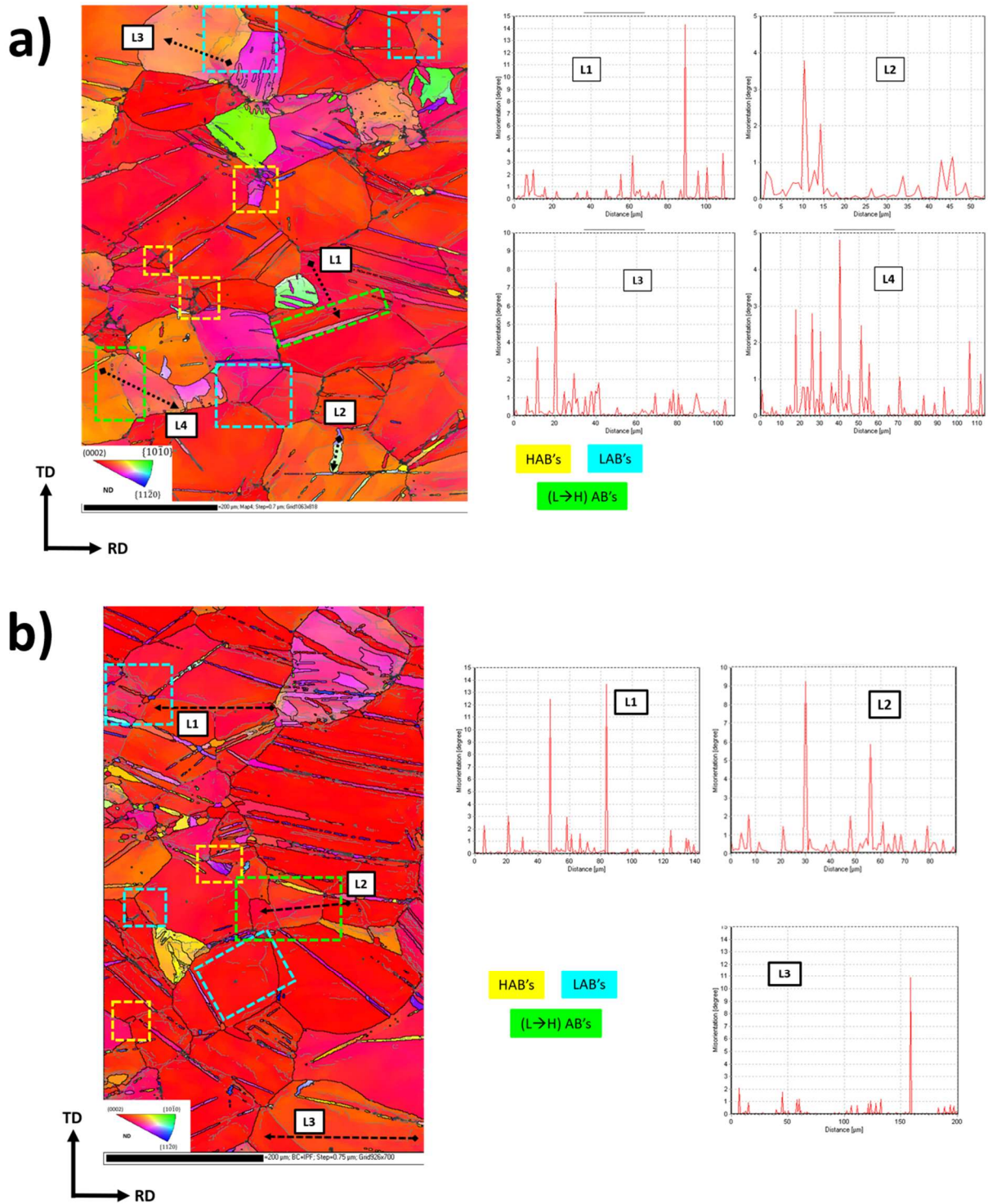


Fig. 5.3. EBSD analysis at  $\epsilon = 30\%$ : EBSD map in ND IPF coloring and corresponding misorientation line profiles along the black arrows for a) O-1 and b) O-2.

In the special case of the misorientation linear profile 'L3' in the map of O-1, the arrow crosses an extension twin. This twin consisted of two (blue and green) colored regions, which present a misorientation angle of up to  $11^\circ$  causing the appearance of a low angle grain boundary (LAGB) that separates these two zones. One of these zones has an orientation close to  $\{11\bar{2}0\}$  (blue fraction) and the other close to  $\{10\bar{1}0\}$  (red fraction), i.e a rotation of the cell around the c-axis, revealing the prismatic slip activity. It is also important to emphasize that this LAGB seems to have continuity towards the basal matrix surrounding the twin, that could indicate slip transmission across twin boundaries [30].

Fig. 5.8 shows the EBSD results at  $\varepsilon = 50\%$  for a) O-1 and b) O-2. As well as 30%, at this stage of rolling the CDRX mechanism was still observed but DDRX no longer. For both orientations, the cyan boxes enclose regions with low angle grain boundaries (LAGBs), and further strain these LAGBs could trap more dislocations and transform into HAGBs turning into new recrystallized grains, i.e., continuous absorption of dislocations in the sub-grains: CDRX mechanism.

The yellow boxes in Fig 5.8 indicate HAGBs. In the case of O-2, this grain seems to have formed due to the partition of a larger grain. This can be observed inside the green box that indicates an area where there is a transition from an LAGB to a HAGB (the line-color of the grain boundary in some sections is black and, in some others, it is gray). Coupled with this, the profile of line L1 that crosses such grain with many LAGB's inside, shows that the misorientation within reaches  $14^\circ$ , revealing the almost completely transformation of this LAGB to HAGB, which is a clear evidence of CDRX. This transition can also be appreciated in L1 of O-1. It is relevant to point out that in Z1 of O-1, the LAGBs seem to be aligned with RD.

Fig. 5.9 shows the DRX behavior at  $\varepsilon = 80\%$ . About O-1 (a), the recrystallized regions characterized by a low misorientation ( $\sim 30^\circ$ ), was very prominent throughout the whole sample. Their morphological feature revealed characteristic band arrangements embedded within unrecrystallized zones especially inside Z1 (Fig. 4.2 y 6.8). This kind of arrangements seems to be recrystallized twin bands (DRXed-TB's), it is evident the grains inside them have a non-basal orientations (blue, yellow, violet and green grains), unveiling again the effect of contraction twins (CTs) to nucleate non-basal orientations.

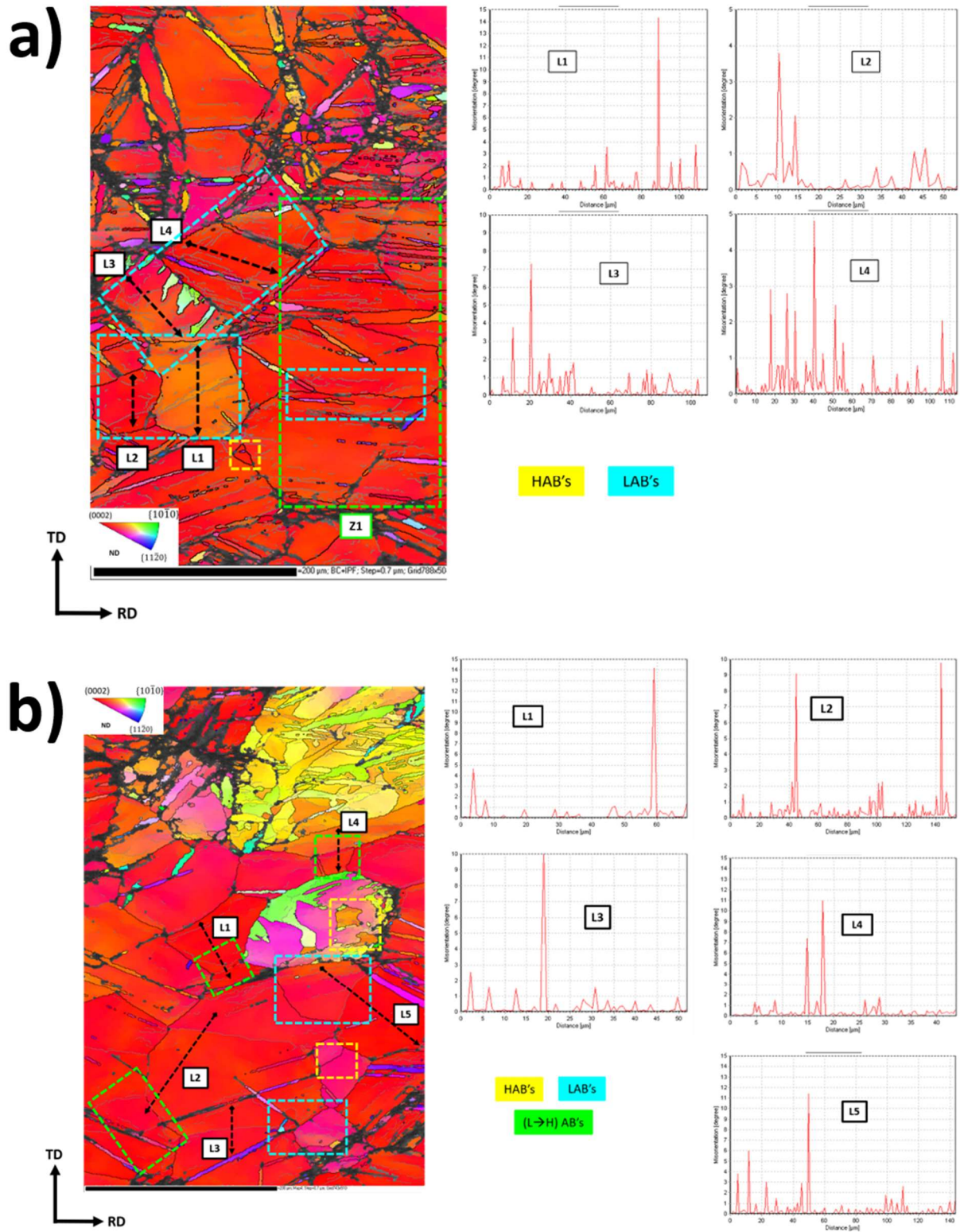


Fig. 5.4. EBSD analysis at  $\epsilon = 50\%$ : EBSD map in ND IPF coloring and corresponding misorientation line profiles along the black arrows for a) O-1 and b) O-2.

The rest of the microstructure (out of the bands) shows most of the recrystallized grains retain a basal orientation. In the line profiles L1-L4, that cross grains presumably belonging to the initial basal orientation matrix, can be observed that misorientation reach  $11^\circ$ , suggesting that this kind of large grains were divided into the small recrystallized grains that retain its basal orientation. Also, the formation of low angle grain boundaries (LAGBs) can be observed inside the grains pointed by cyan boxes and TB's (green boxes).

For O-2, the microstructure is so much coarser and inhomogeneous (coarse basal orientation grains + recrystallized grains within twin bands), high angle grain boundaries (HAGBs) formed within the basal grains (blue boxes) and twin bands (TBs - yellow boxes) subdividing them into several grains. The line profiles of point-to-point along the black arrows show that the misorientation angles gradually increased up to  $10^\circ$  inside the grains of basal orientation matrix, suggesting the high activity of dislocations in these grains.

For both orientations fine grains were observed to form at the region where the sub-grains severely accumulated. It can be inferred that the nucleation of recrystallized grains was associated with the continuous absorption of dislocations in these sub-grains. As stated earlier, such kind of formation of grains is classified as CDRX mechanism.

Additional EBSD measurements at the same strain (Fig. 5.10) revealed similar fragmented twin bands, the same formation of LAGBs within basal orientation grains (cyan boxes) with a similar misorientation up to  $10^\circ$  (line profiles) for both orientations. The importance of these images lies in the inserts where is evident the formation of LAGBs and its transition to HAGBs giving rise to new recrystallized grains without a nucleation site (as grain or twin boundaries). This further confirms the conversion of LAGBs into new grains via continuous increase in misorientation.

It is worth to note, with progressing strain and further DRX it became harder to twin the 'decreasing residual' volume of fragmented parent matrix, reflecting the grain size sensitivity of twinning [129].



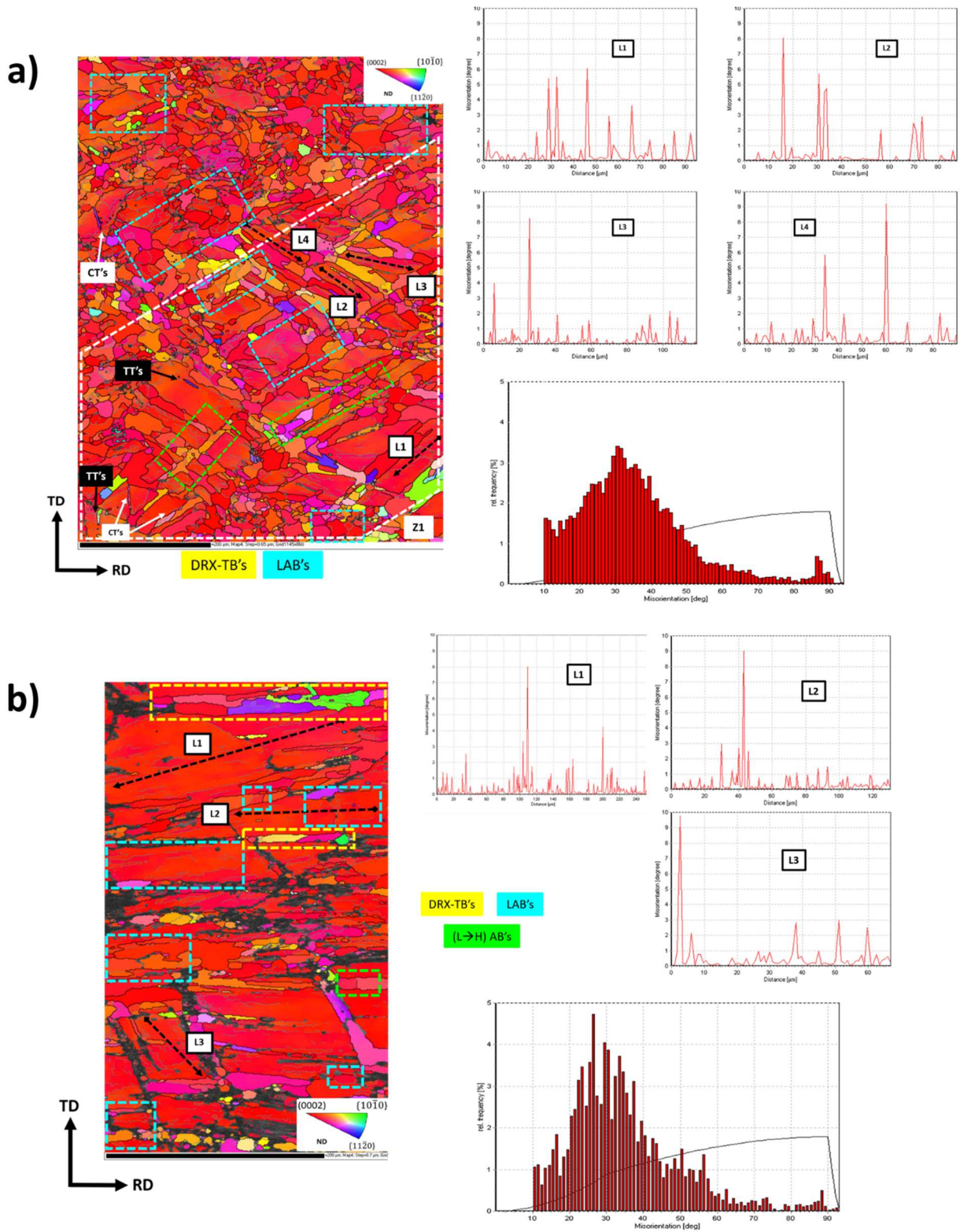


Fig. 5.5. EBSD analysis at  $\epsilon=80\%$ : EBSD map in ND IPF coloring and corresponding misorientation line profiles along the black arrows as well as grain misorientation profile for a) O-1 and b) O-2.

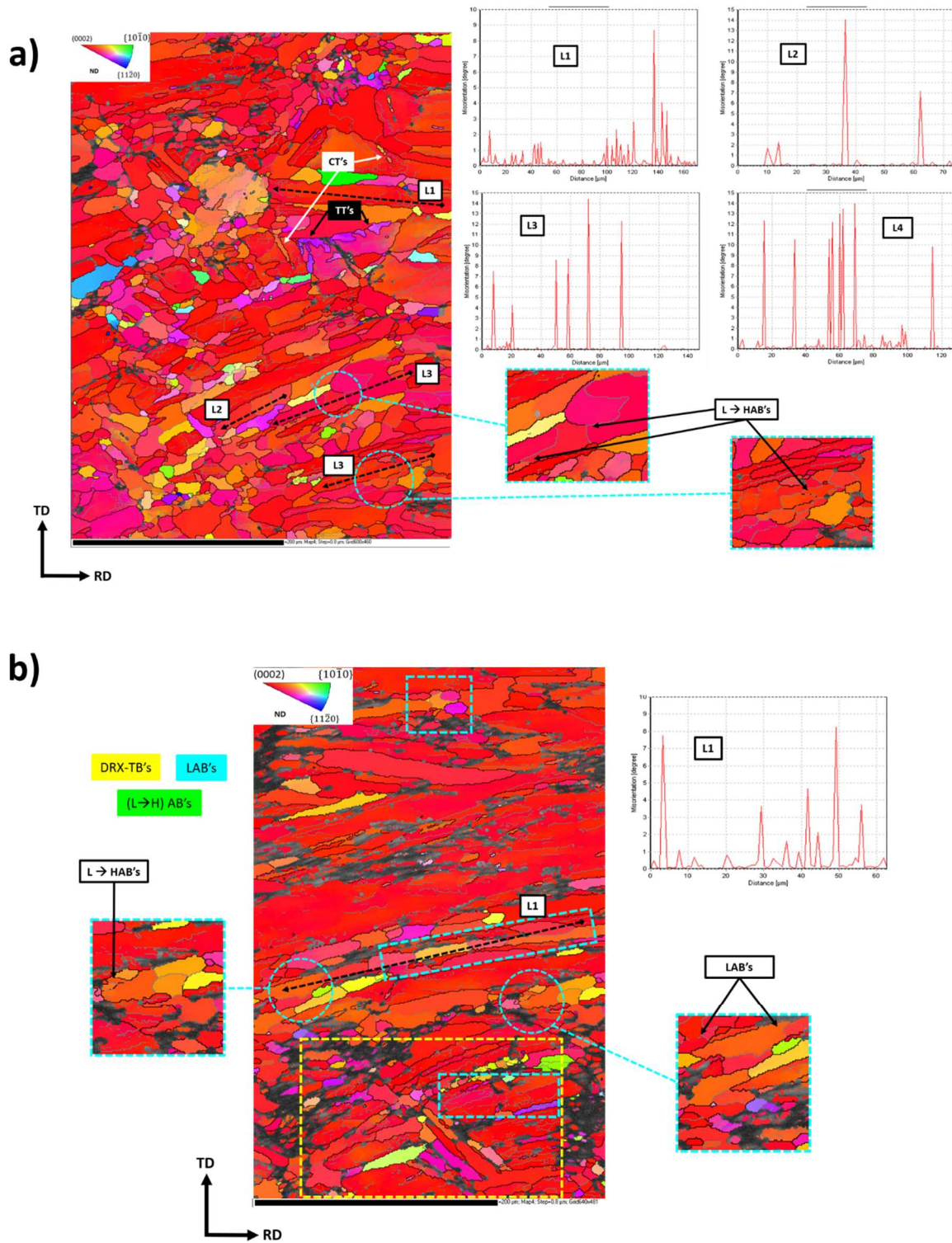


Fig. 5.6. EBSD analysis at  $\epsilon=80\%$ : EBSD map in ND IPF coloring and corresponding misorientation line profiles along the black arrows as well as grain misorientation profile for a) O-1 and b) O-2.

### 5.4. PREFERENTIAL GROWTH MECHANISM DURING POST ROLLING ANNEALING.

After conducted isothermal annealing for 30 min at 450°C followed by cooling inside furnace, the static grain growth was observed. According to Fig. 11 and 12, the O-2 has the sharpest basal texture and present the largest grain size, so, the minimum grain size was obtained for O-1, which has the weakest basal texture. This can be explained because the original microstructure for O-2 was much thicker than for O-1 (Fig 5.9 and 5.10) and the basal component intensity was higher for O-2 than O-1.

However, after a strict analysis of annealing map orientation, it is evident that the grains with the c-axis aligned more parallel to the ND tend to growth, instead the grains with the c-axis more deviated from ND tend to be absorbed by the first. It could be explained by the initial microstructure ( $\varepsilon = 80\%$ ) wherein the grains with a basal orientation were coarser and posse a largest grain boundary curvature than recrystallized grains which have a non-basal orientation.

Fig. 5.11 shows the samples of O-1 (a) and O-2 (b) led to the grain growth by grain boundary movement which depends on the rate of movement of VLAGBs (very low angle boundaries) [130]. The evidence of conversion of high angle grain boundaries (HAGBs  $>15^\circ$ ) to low angle grain boundaries (LAGBs,  $5-15^\circ$ ) to VLAGBs ( $2-5^\circ$ ) was observed irrespective of their orientations (Figs. 5.11a and 5.12b).

The inset 1 of Fig. 5.11a shows the transition of HGBs  $>35^\circ \rightarrow >30^\circ \rightarrow >25^\circ \rightarrow >15^\circ$ , i.e. the red grain boundaries converted to a yellow grain boundaries, the yellow converted into a blue, the blue turned to magenta. The inset 2 shows the transition of  $30^\circ$  to  $25^\circ$  grain boundaries. The inset 3 shows the change of  $15^\circ$  to  $2^\circ$ , and finally, the inset 4 shows the most important evolution, the  $2^\circ$  grain boundaries disappears, also in insert 3 it can be observed, the disappearance verifies that the movement of grain boundaries is from HAGBs to VLAGBs and not vice versa, otherwise a refinement in the grain size and not a growth was observed.

The corresponding grain boundary misorientation figures show that after annealing time, all the grain boundaries have a maximum misorientation of  $40^\circ$ , against to  $\epsilon = 80\%$  where the misorientation grain ranged between  $10-60^\circ$ , delating the grains tend to have the same orientation (basal). It is in total agreement with recent researches that reported magnesium and Mg alloys tend to sharpen their texture upon grain growth [53].

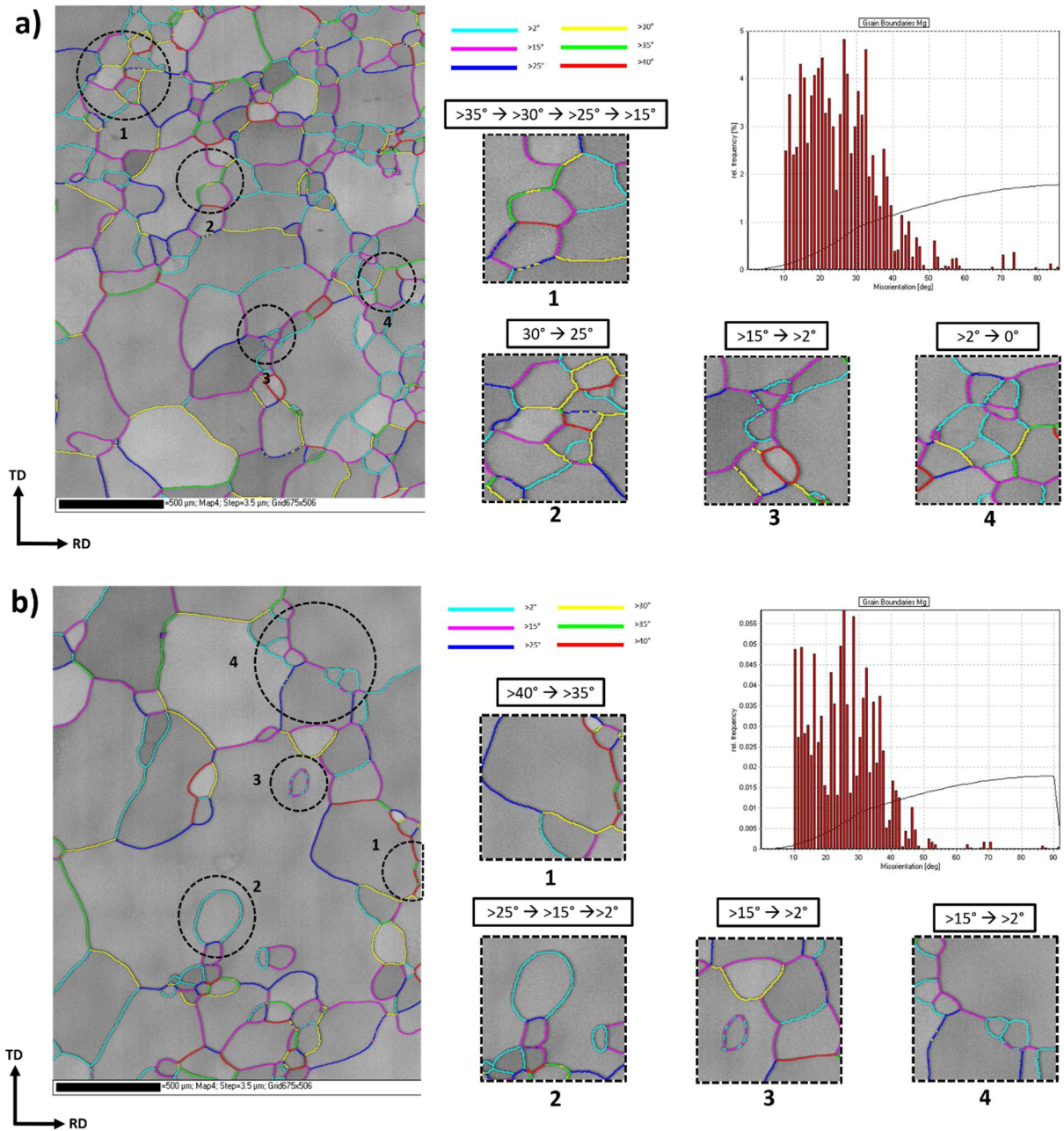


Fig. 5.7. Boundary misorientation maps and corresponding misorientation angle distribution of a) O-1 and b) O-2.



# *Conclusions and Future Research*

## **6.2. CONCLUSIONS**

The deformation rolling parallel to the c-axis of magnesium single crystals was dominated by  $\{10\bar{1}2\}$  twinning at the first rolling steps, which almost completely rotated the original crystal into a new matrix of basal grains, the extension twins variants that took place determined the intensity of the basal texture, orientation 1 presented the weakest basal texture at all strains and annealing state, its extension twins variants aligned the c-axis  $\sim 30^\circ$  deviated from ND, against orientation 2, which extension twins aligned the basal plane almost parallel to sheet plane. In the orientation 1 primary, secondary and tertiary extension twins were observed.

In the new basal matrix contraction twins were observed at  $\varepsilon$  of 30% and 50%. At  $\varepsilon = 80\%$  the deformation was accommodated without twinning. This contraction twins suffered shear localization attributed to easier conditions for plastic flow inside them as than within the 'hard' basal matrix, leading twin-induced CDRX, and formed recrystallized twin bands giving rise to grains with its c-axis  $30^\circ$  rotated from its parent grain, i.e. these grains have a non-basal orientation. On the orientation 1 contraction twins grew and recrystallized until  $= 50\%$ . On the other hand in orientation 2 contraction twins recrystallized since  $\varepsilon = 30\%$ .

The contraction twin bands work as nucleation sites for non-basal grains, however no profuse contraction twinning was developed and the grains that nucleate inside  $\{10\bar{1}1\}$  twins cannot grow outside the twin boundaries so the influence of twin-induced DRX mechanism on the final texture weakening was very limited (there was not a texture change).

DDRX was observed at  $\varepsilon = 30\%$  for both orientations, fine grains and sub-grains boundaries formed at the triple junctions of the grains. Instead, CDRX were observed at all strains, by the transition of LAGBs to HAGBs within the basal grains and recrystallized grains inside the twin bands. At  $\varepsilon = 80\%$  the orientation 1 microstructure was characterized by basal orientation grains and non-basal orientation grains within twin bands arrangements embedded inside basal un-recrystallized zones. For orientation 2 the microstructure consisted in coarse twin bands (recrystallized grains having a non-basal orientation) surrounded by a matrix of basal orientation grains.

After annealing for 30 min at  $450^\circ$ , grain growth was observed in both orientations governed by grain boundary movement. An evident transition sequence of movement of grain boundaries could be observed, high angle grain boundaries (HAGBs,  $>15^\circ$ ) converted into low angle grain boundaries (LAGBs,  $5-15^\circ$ ), that turned to very low angle grain boundaries (VLAGB,  $2-5^\circ$ ), which tend to disappear. The basal orientation grains grew preferentially, strengthening the basal texture after annealing treatment.

### 6.2. FUTURE RESEARCH

The limitations of this research point towards topics to be addressed in the future, a similar study with other four orientations is being carried out in order to compare with the last studies of PSC for these six orientations. Two of them with the c-axis parallel to the ND in order to orient the crystal for contraction twins and the other two orientations with the c-axis parallel to TD, i.e.  $\{10\bar{1}1\}$  and  $\{11\bar{2}0\}$  directions are parallel to RD, in this we expect a profuse extension twinning owing to the compression perpendicular to c-axis.

Also, a more detailed analysis at strain of 10% is being studied to understand and characterize the extension twinning that presumably gave rise to basal texture in this study. This would allow more detailed information about the nature of ETs.

The next stage of this work is comprised by the study of specimen with a few grains as bi-crystals and oligocrystals in order to unveiling the role of grain boundaries during hot rolling.

# Appendix A

## CHEMICAL COMPOSITION OF MAGNESIUM USED FOR THE CRYSTAL GROWTH

The chemical composition of a grown crystal is given in Table A.2. Although a steel mold was used, the amount of Fe increased only marginally compared to the initial material Table A.1.

Table A.2. Chemical composition (wt.%) of the initial pure Mg material used for crystal growth (obtained by spark optical emission spectroscopy).

<b>Al</b>	<b>Zn</b>	<b>Mn</b>	<b>Si</b>	<b>Fe</b>	<b>Cu</b>	<b>Ni</b>	<b>Be</b>
<0.0020	<0.0025	0.0039	0.0038	<0.0012	<0.0005	<0.0015	0.0001
<b>Ca</b>	<b>Cd</b>	<b>Ag</b>	<b>Ce</b>	<b>La</b>	<b>Nd</b>	<b>Pr</b>	<b>Th</b>
<0.0002	<0.0002	<0.0010	<0.0050	0.0013	<0.0060	<0.0030	<0.0150
<b>Zr</b>	<b>Na</b>	<b>P</b>	<b>Pb</b>	<b>Sn</b>	<b>Mg</b>		
<0.0010	0.0003	0.0016	<0.0040	<0.0020	99.98		

Table A.3. Chemical composition (wt.%) of a grown pure Mg single crystal (obtained by spark optical emission spectroscopy).

<b>Al</b>	<b>Zn</b>	<b>Mn</b>	<b>Si</b>	<b>Fe</b>	<b>Cu</b>	<b>Ni</b>	<b>Be</b>
<0.0020	<0.0025	0.0047	0.0015	<0.0028	<0.0005	<0.0015	0.0001
<b>Ca</b>	<b>Cd</b>	<b>Ag</b>	<b>Ce</b>	<b>La</b>	<b>Nd</b>	<b>Pr</b>	<b>Th</b>
<0.0002	<0.0002	<0.0010	<0.0050	0.0015	<0.0060	<0.0030	<0.0150
<b>Zr</b>	<b>Na</b>	<b>P</b>	<b>Pb</b>	<b>Sn</b>	<b>Mg</b>		
<0.0010	0.0002	0.0010	<0.0040	<0.0020	99.98		





# Appendix B

## LAUE PATTERNS OF MAGNESIUM SINGLE CRYSTALS

The Fig. B.1 shows the Laue patterns obtained for both orientations a) O-1 and b) O-2, it corresponds to (0002) plane. A rotation of  $30^\circ$  of the O-1 with respect to the O-2 can be appreciated.

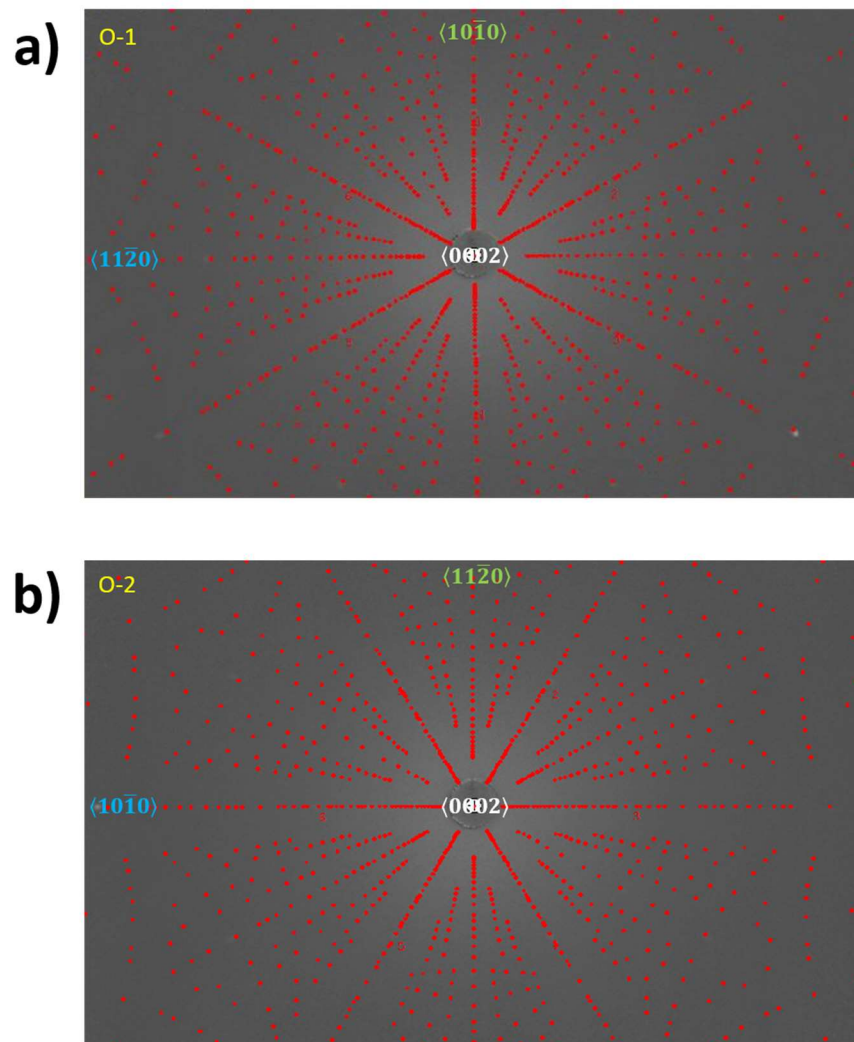


Fig. B.1. (0002) Laue patterns of a) O-1 and b) O-2.



# Appendix C

## ROLLING SCHEDULE

The table C.1 presents the rolling schedule used for the experimental work. Every deformation state analyzed in the current work is highlighted in different color.

Table C.4. Rolling Schedule

Rolling passes	Thickness (mm)	Deformation ( $\varphi$ )	Annealing (min)	Total reduction (%)
0	6.0		30	
1	5.77	0.05	10	4.88
2	5.49	0.05	10	9.52
3	5.22	0.05	10	13.93
4	4.97	0.05	10	18.13
5	4.73	0.05	10	22.12
6	4.45	0.06	10	26.66
7	4.19	0.06	10	30.93
8	3.95	0.10	10	34.95
9	3.57	0.10	10	41.14
10	3.17	0.12	10	47.80
11	2.81	0.12	10	53.70
12	2.42	0.15	10	60.15
13	2.08	0.15	10	65.70
14	1.76	0.17	10	71.06
15	1.48	0.17	10	75.59
16	1.21	0.20	10	80.01



# Appendix D

## COMPLEMENTARY POLE FIGURES

### D.1. COMPLEMENTARY POLE FIGURES OF O-1

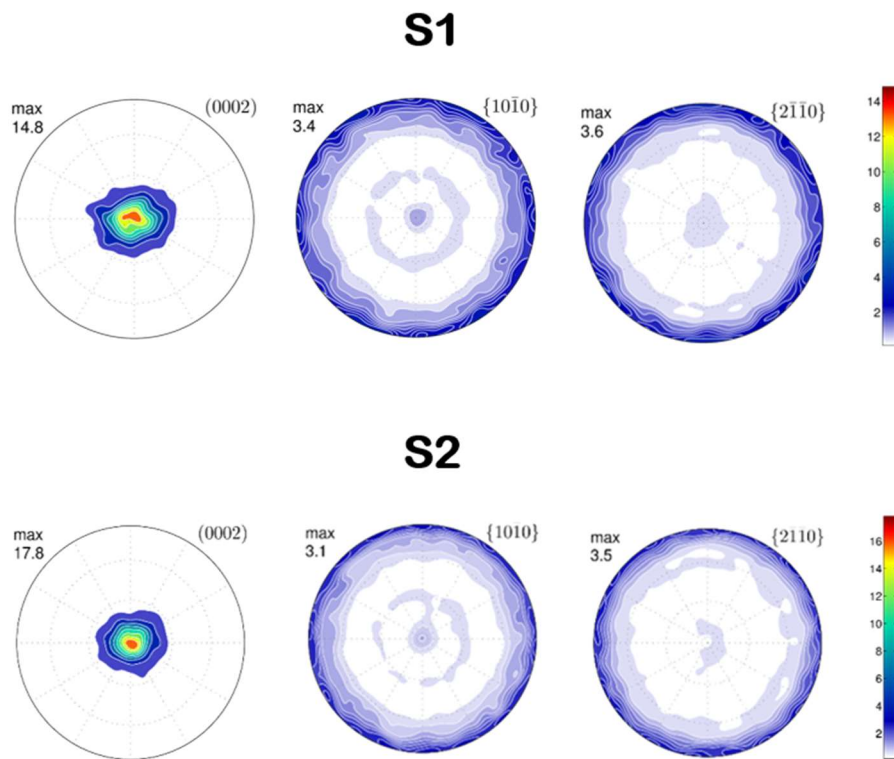


Fig. D.1. Pole Figures of O-1 at  $\varepsilon = 30\%$

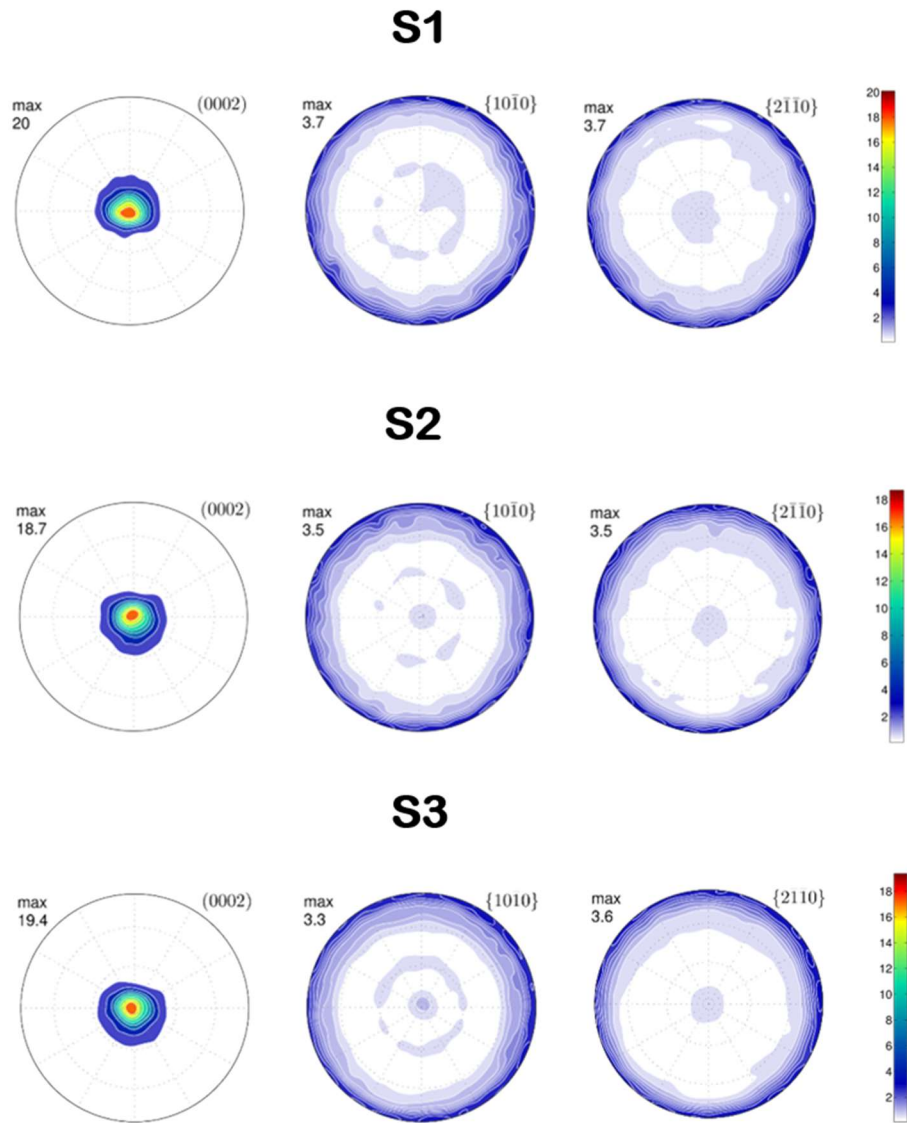


Fig. D.2. Pole Figures of O-1 at  $\varepsilon = 50\%$

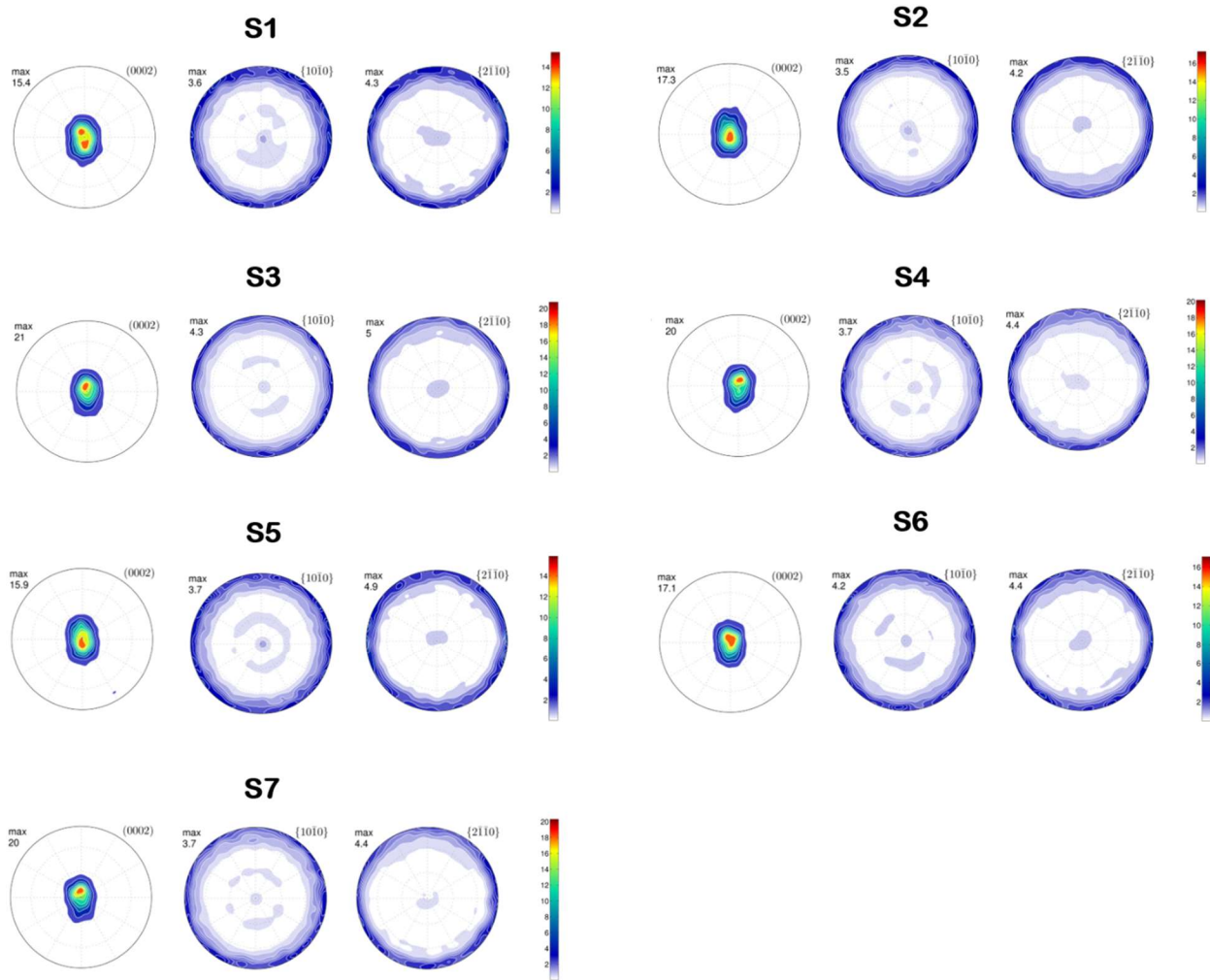


Fig. D.3. Pole Figures of O-1 at  $\epsilon = 80\%$



D.2. COMPLEMENTARY POLE FIGURES OF O-2

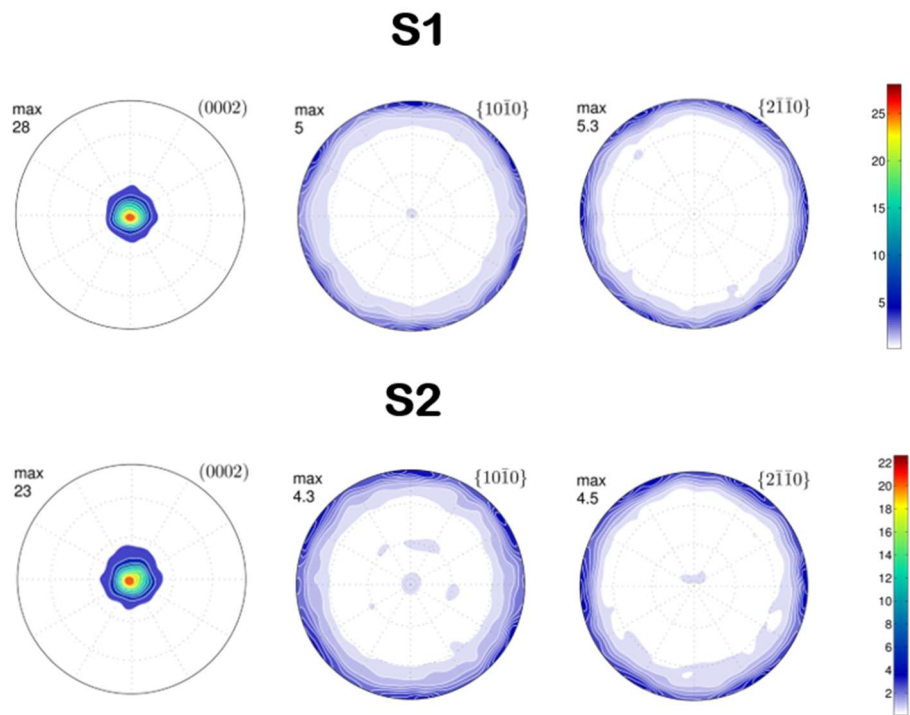


Fig. D.4. Pole Figures of O-2 at  $\epsilon = 30\%$

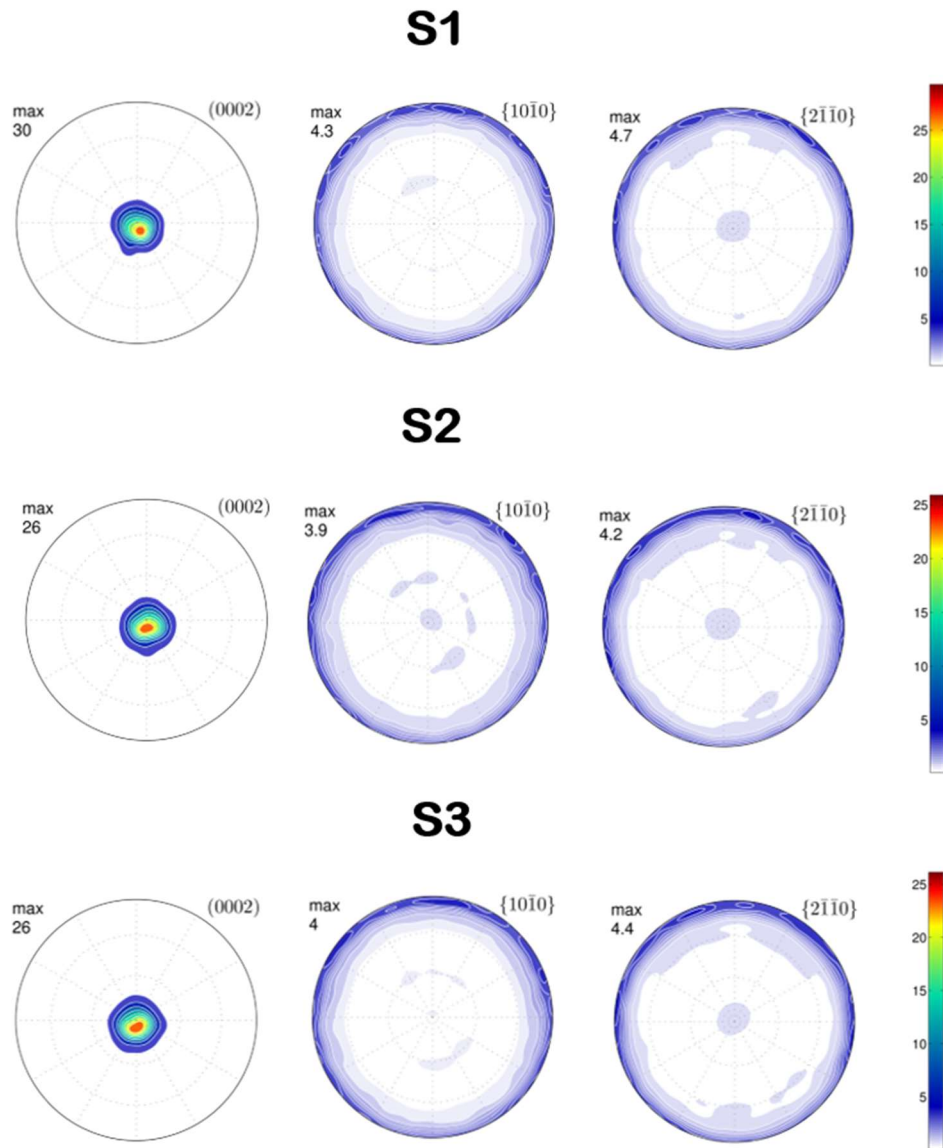


Fig. D.5. Pole Figures of O-2 at  $\epsilon = 30\%$

## APPENDIX D. COMPLEMENTARY POLE FIGURES

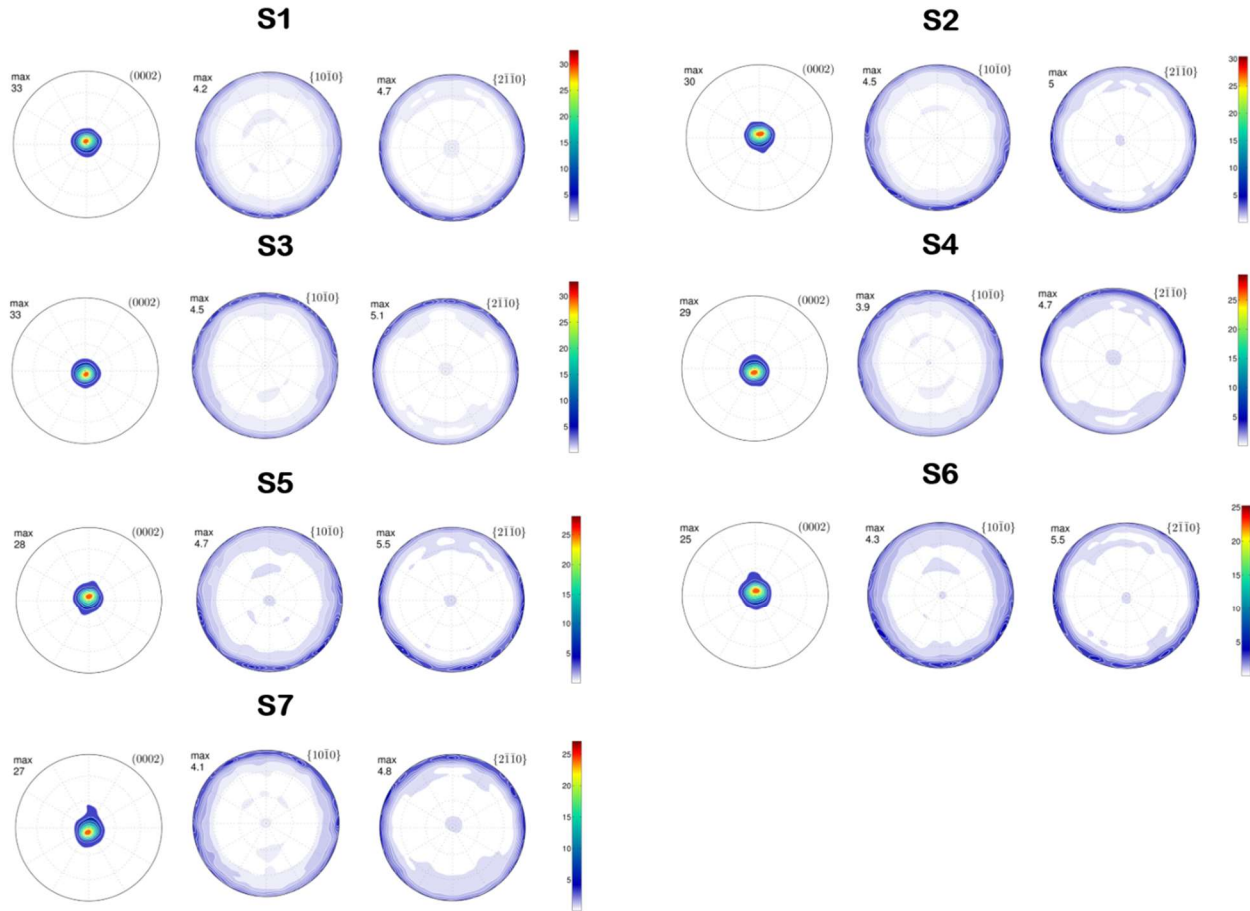
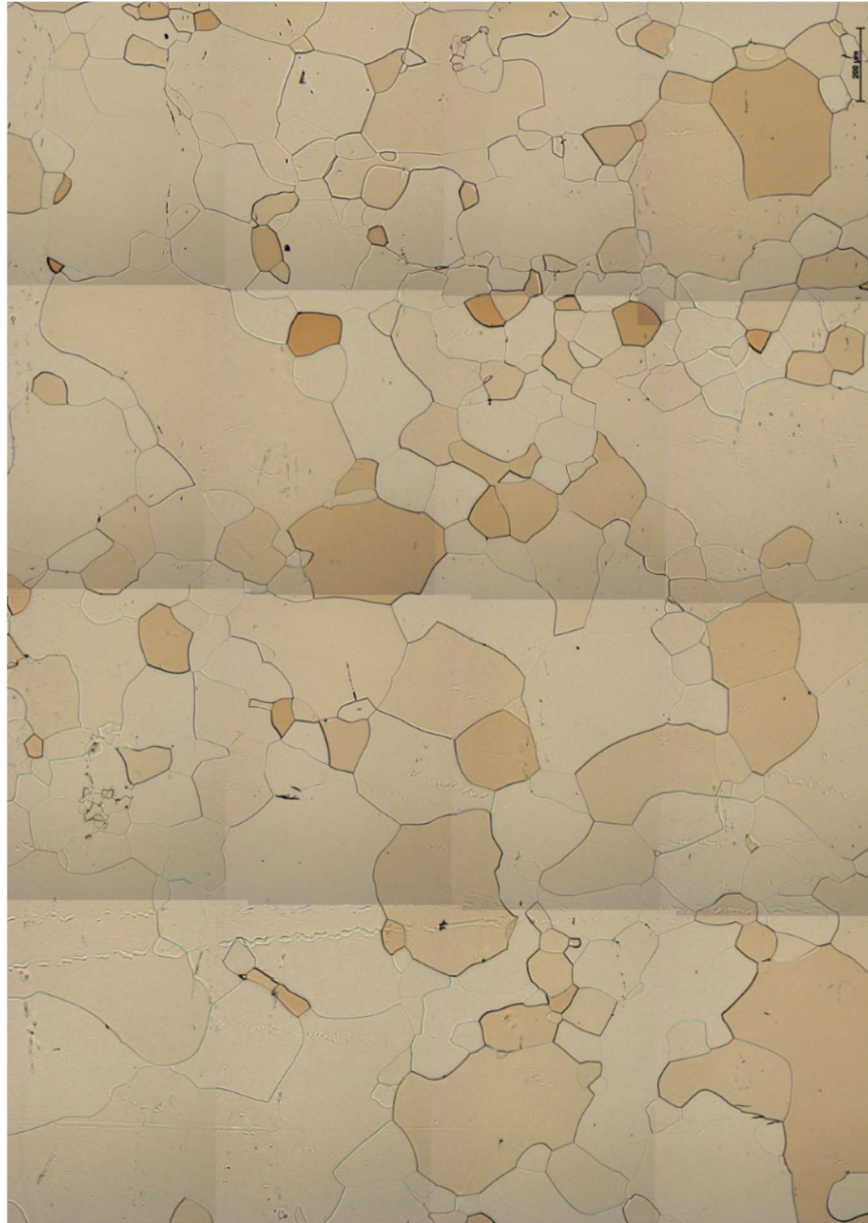


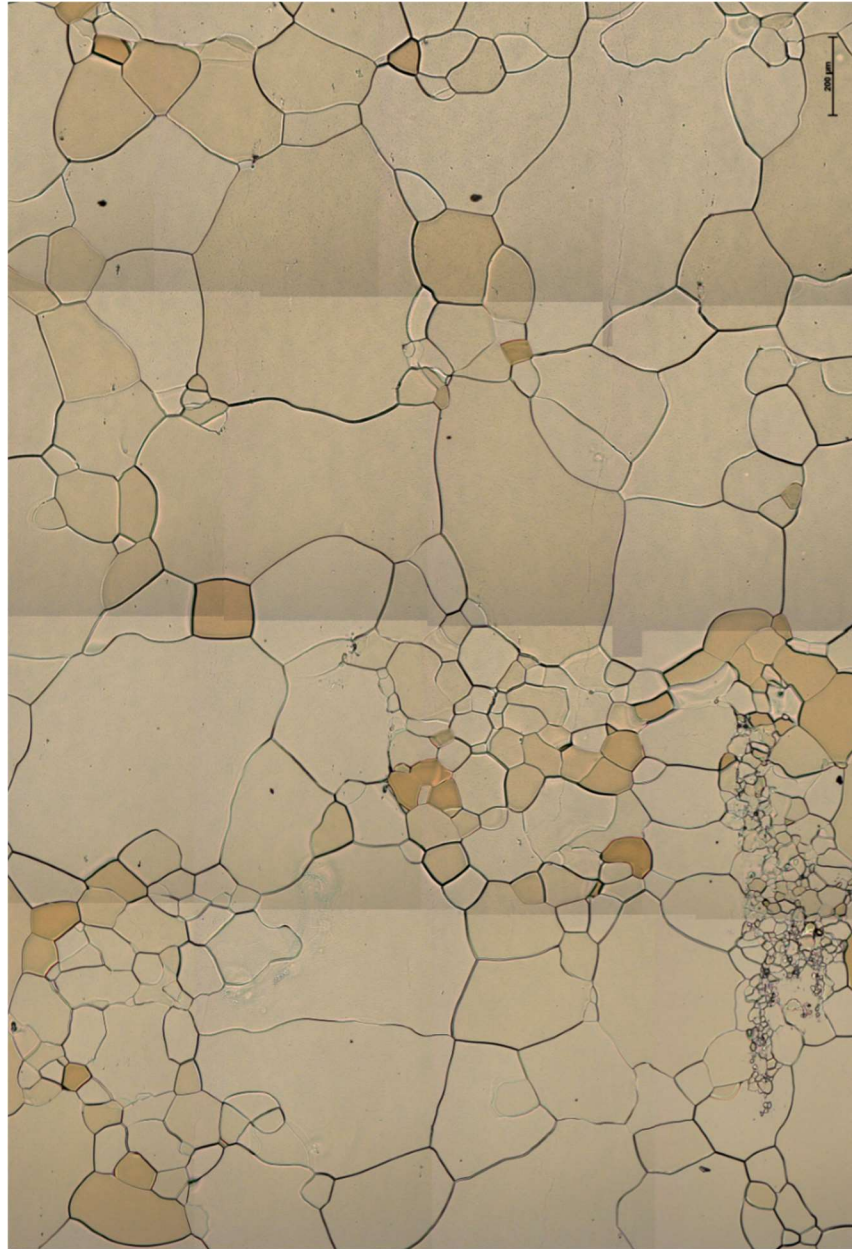
Fig. D.6. Pole Figures of O-2 at  $\varepsilon = 30\%$

# Appendix E

## COMPLEMENTARY METALLOGRAPHIES



*Fig. E.1. Metallography used for grain size measurements of orientation 1.*



*Fig. E.2. Metallography used for grain size measurements of orientation 2.*

1. Brandt, E.N., *We Called it Mag-nificent: Dow Chemical and Magnesium 1916-1998*, MSU Press, East Lansing, 2013.
2. Blawert, C., Hort, N., Kainer, K. U., *Automotive applications of magnesium and its alloys*. Trans Indian Inst Met Vol. 57 No. 4, 2004, 397–408
3. Bowers, P. M., *Boeing Aircraft Since 1916*. Funk & Wagnalls, New York, 1968, pp. 221-281.
4. Mezger, H., *The Development of the Porsche Type 917 Car*. Archive: Proceedings of The Institution of Mechanical Engineers, Vol. 186 No. 2, 1972, pp. 11-28.
5. Hector, B. and Heiss, W., *Magnesium Die-Castings as Structural Members in the Integral Seat of the New Mercedes-Benz Roadster*, SAE Technical Paper 900798, Warrendale, PA, 1990.
6. G. Craig, *Use of WE-43A-T6 Magnesium in the MD600 Helicopter Drive System*, International Magnesium Association, Coronado, CA, 1998, pp. 19-23
7. White, M., *Jaguar Light Weight Vehicle Strategy-The New XJ Body Design*. EuroCarBody Conference; Bad Nauheim, Germany, 2009.
8. M. Wise, K. Calvin, A. Thomson, L. Clarke, B. Bond-Lamberty, R. Sands, S. J. Smith, A. Janetos, and J. Edmonds, *Science* May 2009, Vol. 324, Nr. 5931, p. 1183 –1186.
9. L. R. Kump, *Nature* 2002, Vol. 419, No. 6903, p. 188–190.
10. T. M. Pollock, *Science* May 2010, Vol. 328, Nr. 5981, p. 986 –987.
11. H. A. Patel, D. L. Chen, S. D. Bhole, and K. Sadayappan, *Materials Science and Engineering: A* Nov. 2010, Vol. 528, Nr. 1, p. 208–219.
12. Olguín M. de L., Hernández- Silva D, *“Ductilidad a alta temperatura de las aleaciones de magnesio AZ31 y AZ61”*, Tesis de Maestría en Ciencias en Ingeniería Metalúrgica. ESIQIE, IPN, México D. F. 2012.
13. Barnett, M. R., Stanford, N., Cizek, P., Beer, A., Xuebin, Z., & Keshavarz, Z. *Deformation mechanisms in Mg alloys and the challenge of extending room-temperature plasticity*. The Journal of The Minerals, Vol. 61. No. 8. 2009. Pp. 19–24.

## REFERENCES

---

14. Bettles, C., Gibson, M., *Current wrought magnesium alloys: Strengths and weaknesses*, The Journal of The Minerals. Vol. 57. No. 5. (2005) pp. 46–49.
15. Chapuis A., Driver J.H., *Acta Mater* 2011; 59:1986.
16. E. Ball, P. Prangnell, *Tensile-compressive yield asymmetries in high strength wrought magnesium alloys*, Scripta Metallurgica et Materialia 31 (1994) 111-116.
17. Ulacia I, Dudamell NV, Galvez F, Yi S, Perez-Prado MT, Hurtado I, *Acta Mater* 2010; 58:2988.
18. Barnett M. R., *Metall Mater Trans A* 2003; 34:1799.
19. S. Bräunig, M. Düring, H. Hartmann, B. Viehweger, *Magnesium sheets for industrial application*, in: K.U. Kainer (Ed.), *Magnesium. Proceedings of the 6th International Conference Magnesium Alloys and Their Applications*, Wiley-VCH, Weinheim, 2005, pp. 955-961.
20. A.A. Luo, A.K. Sachdev, *Applications of magnesium alloys in automotive engineering*, in: C. Bettles, M. Barnett (Eds.), *Advances in Wrought Magnesium Alloys. Fundamentals of processing, properties and applications*, Woodhead Publishing, Cambridge, 2012, pp. 393-426.
21. E.W. Kelley, W.F. Hosford, *Deformation characteristics of textured magnesium*. Transactions of the Metallurgical Society of Aime 242 (1968) 654
22. S. Graff, W. Brocks, D. Steglich, *Yielding of magnesium: From single crystal to polycrystalline aggregates*. Int. J. Plast. 23 (2007) 1957-1978.
23. B.C. Wonsiewicz, W.A. Backofen, *Plasticity of magnesium crystals*, Trans. AIME 239 (1967) 1422-1431.
24. E.W. Kelley, W.F. Hosford, *Plane-Strain Compression of Magnesium and Magnesium Alloy Crystals*, Trans. AIME 242 (1968) 5-13.
25. Molodov, K. D., Al-Samman, T., Molodov, D. A., & Gottstein, G. (2014). *On the Ductility of Magnesium Single Crystals at Ambient Temperature*. Metallurgical and Materials Transactions A, 45(8), 3275–3281.
26. Molodov, K. D., Al-Samman, T., Molodov, D. A., & Gottstein, G. (2014). *Mechanisms of exceptional ductility of magnesium single crystal during deformation at room temperature: Multiple twinning and dynamic recrystallization*. Acta Materialia, 76, 314–330.
27. Molodov, K. D., Al-Samman, T., & Molodov, D. A. (2015). *Deformation-Induced Recrystallization of Magnesium Single Crystals at Ambient Temperature*. IOP Conference Series: Materials Science and Engineering, 82, 012014.

28. Molodov, K. D., Al-Samman, T., Molodov, D. A., & Gottstein, G. (2016). *On the role of anomalous twinning in the plasticity of magnesium*. Acta Materialia, 103, 711–723.
29. Molodov, K. D., Al-Samman, T., & Molodov, D. A. (2016). *On the diversity of the plastic response of magnesium in plane strain compression*. Materials Science and Engineering: A, 651, 63–68.
30. Molodov, K. D., Al-Samman, T., & Molodov, D. A. (2017). *Profuse slip transmission across twin boundaries in magnesium*. Acta Materialia, 124, 397–409.
31. Molodov, K. D., Al-Samman, T., Molodov, D. A., & Korte-Kerzel, S. (2017). *On the twinning shear of  $\{10\bar{1}2\}$  twins in magnesium – Experimental determination and formal description*. Acta Materialia, 134, 267–273.
32. M.H. Yoo, *Slip, twinning and fracture in hexagonal closed packed metals*. Metall. Trans. A 12 (1981) 409-418.
33. T. Ungar, A. Borbely, *The effect of dislocation contrast on x-ray line broadening: A new approach to line profile analysis*. Applied Physics Letters 69 (1996) 3173-3175.
34. T. Ungar, J. Gubicza, G. Ribarik, A. Borbely, *Crystallite size distribution and dislocation structure determined by diffraction profile analysis: principles and practical application to cubic and hexagonal crystals*. Journal of Applied Crystallography 34 (2001) 298-310.
35. E. Schiebold, G. Siebel, *Studien an Magnesium und Magnesiumlegierungen*, Z. Phys. 69 (1931) 458-482.
36. E. Schmid, *Beiträge zur Physik und Metallographie des Magnesiums*, Zeitschrift für Elektrochemie und angewandte physikalische Chemie 37 (1931) 447-459.
37. N. Chetty, M. Weinert, *Stacking faults in magnesium*, Phys. Rev. B 56 (1997) 10844-10851.
38. G. Siebel, *Physikalische Eigenschaften des Magnesium-Einkristalls und ihre Bedeutung für den Vielkristall*, in: H. Altwicker, A. Bauer et al. (Eds.), Magnesium und seine Legierungen, Springer-Verlag Berlin Heidelberg, Berlin, 1939, pp. 18-36.
39. E.C. Burke, W.R. Hibbard, *Plastic deformation of magnesium single crystals*, Trans. AIME 194 (1952) 295-303.
40. Z.S. Basinski, *The influence of temperature and strain rate on the flow stress of magnesium single crystals*, Aust. J. Phys. 13 (1960) 284-298.



## REFERENCES

---

41. W.F. Sheely, R.R. Nash, *Mechanical properties of magnesium monocrystals*, Trans. AIME 218 (1960) 416-423.
42. H. Yoshinaga, R. Horiuchi, *Work Hardening Characteristics of the Basal Slip of Magnesium Single Crystals*, Trans. JIM 3 (1962) 220-226.
43. P.B. Hirsch, J.S. Lally, *The deformation of magnesium single crystals*, Philos. Mag. 12 (1965) 595-648.
44. A. Akhtar, E. Teghtsoonian, *Solid solution strengthening of magnesium single crystals—I alloying behaviour in basal slip*, Acta Metall. 17 (1969) 1339-1349.
45. B. Bhattacharya, M. Niewczas, *Work-hardening behaviour of Mg single crystals oriented for basal slip*, Philos. Mag. 91 (2011) 2227-2247.
46. B. Sułkowski, R. Chulist, B. Beausir, W. Skrotzki, B. Mikułowski, *Stage B work-hardening of magnesium single crystals*, Crystal Research and Technology 46 (2011) 439-442.
47. A. Chapuis, J.H. Driver, *Temperature dependency of slip and twinning in plane strain compressed magnesium single crystals*, Acta Mater. 59 (2011) 1986-1994.
48. F. Hiura, M. Niewczas, *Latent hardening effect under self- and coplanar dislocation interactions in Mg single crystals*, Scr. Mater. 106 (2015) 17-20.
49. P.W. Flynn, J. Mote, J.E. Dorn, *On the thermally activated mechanism of prismatic slip in magnesium single crystals*, Trans. AIME 221 (1961) 1148-1154.
50. E. Schmid, W. Boas, *Kristallplastizität mit besonderer Berücksichtigung der Metalle*, Springer-Verlag, Berlin, 1935.
51. R.E. Reed-Hill, W.D. Robertson, *Deformation of magnesium single crystals by nonbasal slip*, Trans. AIME 220 (1957) 496-502.
52. P.W. Bakarian, C.H. Mathewson, *Slip and Twinning in Magnesium Single Crystals at Elevated Temperatures*, Trans. AIME 152 (1943) 226-254.
53. R.V. Mises, *Mechanik der plastischen Formänderung von Kristallen*, Z. Angew. Math. Mech. 8 (1928) 161-185.
54. G.I. Taylor, *Plastic strain in metals*, J. Inst. Met. 62 (1938) 307-324.
55. S.R. Agnew, O. Duygulu, *Plastic anisotropy and the role of non-basal slip in magnesium alloy AZ31B*. Int. J. Plast. 21 (2005) 1161-1193.

56. B.C. Wonsiewicz, *Plasticity of magnesium crystals. Dissertation: Massachusetts Institute of Technology*, 1966.
57. T. Obara, H. Yoshinga, S. Morozumi, *{1122}<1123> Slip system in magnesium*, *Acta Metall.* 21 (1973) 845-853.
58. J.F. Stohr, J.P. Poirier, *Etude en microscopie electronique du glissement pyramidal {1122} <1123> dans le magnesium*, *Philos. Mag.* 25 (1972) 1313-1329.
59. J.W. Cahn, *Thermodynamic and structural changes in deformation twinning of alloys*, *Acta Metall.* 25 (1977) 1021-1026.
60. B.A. Bilby, A.G. Crocker, *The Theory of the Crystallography of Deformation Twinning*, *Proc. Roy. Soc. London Ser. A* 288 (1965) 240-255.
61. J.W. Christian, S. Mahajan, *Deformation twinning*, *Prog. Mater. Sci.* 39 (1995) 1-157.
62. E. Schmid, G. Wassermann, *Über die mechanische Zwillingsbildung von Zinkkristallen*, *Z. Phys.* 48 (1928) 370-383.
63. M.V. Klassen-Neklyudova, *Mechanical Twinning of Crystals*, Springer US, New York, 1964.
64. J. Wang, I.J. Beyerlein, C.N. Tomé, *An atomic and probabilistic perspective on twin nucleation in Mg*, *Sci. Mat.* 63 (2010) 741-746.
65. A. Vinogradov, E. Vasilev, M. Seleznev, K. Máthis, D. Orlov, D. Merson, *On the limits of acoustic emission detectability for twinning*, *Materials Letters* 183 (2016) 417-419.
66. M.R. Barnett, *A rationale for the strong dependence of mechanical twinning on grain size*, *Sci. Mat.* 59 (2008) 696-698.
67. M.R. Barnett, *Twinning and the ductility of magnesium alloys Part I: "Tension" twins*, *Mat Sci Eng a-Struct* 464 (2007) 1-7.
68. M.R. Barnett, *Twinning and the ductility of magnesium alloys Part II. "Contraction" twins*, *Mat Sci Eng a-Struct* 464 (2007) 8-16.
69. C.H. Mathewson, A.J. Phillips, *Twinning in beryllium, magnesium, zinc, and cadmium*, *Trans. AIME* 78 (1928) 445-452.
70. H. El Kadiri, C.D. Barrett, J. Wang, C.N. Tomé, *Why are twins profuse in magnesium?* *Acta Mater.* 85 (2015) 354-361.
71. R.E. Reed-Hill, *A Study of the {10-11} and {10-13} Twinning Modes in Magnesium*, *Trans. AIME* 218 (1960) 554-557.

## REFERENCES

---

72. H. Yoshinaga, T. Obara, S. Morozumi, *Twinning deformation in magnesium compressed along the C-axis*, Mater. Sci. Eng. 12 (1973) 255-264.
73. S. Godet, L. Jiang, A.A. Luo, J.J. Jonas, *Use of Schmid factors to select extension twin variants in extruded magnesium alloy tubes*, Scr. Mater. 55 (2006) 1055-1058.
74. L. Jiang, J.J. Jonas, R.K. Mishra, A.A. Luo, A.K. Sachdev, S. Godet, *Twinning and texture development in two Mg alloys subjected to loading along three different strain paths*, Acta Mater. 55 (2007) 3899-3910.
75. S.H. Park, S.-G. Hong, C.S. Lee, *Activation mode dependent {10-12} twinning characteristics in a polycrystalline magnesium alloy*, Scr. Mater. 62 (2010) 202-205.
76. J.J. Jonas, S. Mu, T. Al-Samman, G. Gottstein, L. Jiang, É. Martin, *The role of strain accommodation during the variant selection of primary twins in magnesium*, Acta Mater. 59 (2011) 2046-2056.
77. S. Mu, J.J. Jonas, G. Gottstein, *Variant selection of primary, secondary and tertiary twins in a deformed Mg alloy*, Acta Mater. 60 (2012) 2043-2053.
78. Bridgman, Percy W. (1924). "*Certain Physical Properties of Single Crystals of Tungsten, Antimony, Bismuth, Tellurium, Cadmium, Zinc, and Tin*". Proceedings of the American Academy of Arts and Sciences. 60 (6): 305–3
79. Donald C. (1935). "*The Production of Large Single Crystals of Lithium Fluoride*". Review of Scientific Instruments. 7 (3): 133–136
80. Rudolph, Peter. *Handbook of Crystal Growth*, Second Edition, (1989)
81. G.E Dieter, *Mechanical Metallurgy*, Third Edition (1988).
82. S.E. Ion, F.J. Humphreys, S.H. White, *Dynamic recrystallisation and the development of microstructure during the high temperature deformation of magnesium*, Acta Metall. 30 (1982) 1909-1919.
83. A. Galiyev, R. Kaibyshev, G. Gottstein, *Correlation of plastic deformation and dynamic recrystallization in magnesium alloy ZK60*, Acta Mater. 49 (2001) 1199-1207.
84. M.M. Myshlyaev, H.J. McQueen, A. Mwembela, E. Konopleva, *Twinning, dynamic recovery and recrystallization in hot worked Mg–Al–Zn alloy*, Mater. Sci. Eng. A 337 (2002) 121-133.
85. J.C. Tan, M.J. Tan, *Dynamic continuous recrystallization characteristics in two stage deformation of Mg–3Al–1Zn alloy sheet*, Mater. Sci. Eng. A 339 (2003) 124-132.

86. T. Al-Samman, G. Gottstein, *Dynamic recrystallization during high temperature deformation of magnesium*, Mater. Sci. Eng. A 490 (2008) 411-420.
87. T. Al-Samman, K.D. Molodov, D.A. Molodov, G. Gottstein, S. Suwas, *Softening and dynamic recrystallization in magnesium single crystals during c-axis compression*, Acta Mater. 60 (2012) 537-545.
88. A.G. Beer, M.R. Barnett, *Influence of initial microstructure on the hot working flow stress of Mg–3Al–1Zn*, Mater. Sci. Eng. A 423 (2006) 292-299.
89. J.A. del Valle, O.A. Ruano, *Influence of texture on dynamic recrystallization and deformation mechanisms in rolled or ECAPed AZ31 magnesium alloy*, Mater. Sci. Eng. A 487 (2008) 473-480.
90. R. Kaibyshev, *Dynamic recrystallization in magnesium alloys*, in: C. Bettles, M. Barnett (Eds.), *Advances in Wrought Magnesium Alloys. Fundamentals of processing, properties and applications*, Woodhead Publishing, Cambridge, 2012, pp. 186-225.
91. J.L. Urai, W.D. Means, G.S. Lister, *Dynamic Recrystallization of Minerals*, in: B.E. Hobbs, H.C. Heard (Eds.), *Mineral and Rock Deformation: Laboratory Studies, The Paterson Volume*, American Geophysical Union, Washington, D.C., 1986, pp. 161-199.
92. T. Mohri, M. Mabuchi, M. Nakamura, T. Asahina, H. Iwasaki, T. Aizawa, K. Higashi, *Microstructural evolution and superplasticity of rolled Mg-9Al-1Zn*, Mater. Sci. Eng. A 290 (2000) 139-144.
93. O. Sitdikov, R. Kaibyshev, *Dynamic Recrystallization in Pure Magnesium*, Mater. Trans. 42 (2001) 1928-1937.
94. A. Galiyev, R. Kaibyshev, T. Sakai, *Continuous dynamic recrystallization in magnesium alloy*, Mater. Sci. Forum 419 (2003) 509-514.
95. X. Yang, H. Miura, T. Sakai, *Dynamic Evolution of New Grains in Magnesium Alloy AZ31 during Hot Deformation*, Mater. Trans. 44 (2003) 197-203.
96. M.T. Pérez-Prado, J.A. del Valle, J.M. Contreras, O.A. Ruano, *Microstructural evolution during large strain hot rolling of an AM60 Mg alloy*, Scr. Mater. 50 (2004) 661-665.
97. S.B. Yi, S. Zaefferer, H.G. Brokmeier, *Mechanical behaviour and microstructural evolution of magnesium alloy AZ31 in tension at different temperatures*, Mater. Sci. Eng. A 424 (2006) 275-281.

## REFERENCES

---

98. R. Cottam, J. Robson, G. Lorimer, B. Davis, *Dynamic recrystallization of Mg and Mg–Y alloys: Crystallographic texture development*, Mater. Sci. Eng. A 485 (2008) 375-382.
99. K.D. Molodov, T. Al-Samman, D.A. Molodov, G. Gottstein, *Mechanisms of exceptional ductility of magnesium single crystal during deformation at room temperature: Multiple twinning and dynamic recrystallization*, Acta Materialia 76 (2014) 314-330.
100. S.E. Burrows, F.J. Humphreys, S.H. White, *Dynamic Recrystallisation and Textural Development in Magnesium Deformed in Compression at Elevated Temperatures*, in: P. Haasen, V. Gerold, G. Kostorz (Eds.), *Strength of Metals and Alloys*, Pergamon, New York, 1980, pp. 607-612.
101. J.D. Robson, D.T. Henry, B. Davis, *Particle effects on recrystallization in magnesium–manganese alloys: Particle-stimulated nucleation*, Acta Mater. 57 (2009) 2739-2747.
102. É. Martin, J.J. Jonas, *Evolution of microstructure and microtexture during the hot deformation of Mg–3% Al*, Acta Mater. 58 (2010) 4253-4266.
103. F. Humphreys, M. Hatherly, *Recrystallization and related annealing phenomena*, Elsevier, Oxford, 2004.
104. A. Chapuis, *Low temperature plane strain compression of a magnesium single crystal with <c> axis constrained*, Mater. Sci. Eng. A 590 (2014) 401-405.
105. B. Li, M. Liao, Q. Ma, Z. McClelland, *Structure of grain boundaries with 30° [0001] misorientation in dynamically recrystallized magnesium alloys*, Computational Materials Science 101 (2015) 175-180.
106. Li, Q. (2013). *Microstructure and deformation mechanism of 0001 magnesium single crystal subjected to quasistatic and high-strain-rate compressive loadings*. Materials Science and Engineering: A, 568, 96–101.
107. Molodov, D.A., Ivanov, V.A., Gottstein, G., *Low angle tilt boundary migration coupled to shear deformation*, Acta Materialia. Vol. 55 No. 5, (2007) 1843-1848.
108. Hielscher, R., Schaeben, H., *A novel pole figure inversion method: specification of the MTEX algorithm*, Journal of Applied Crystallography. Vol. 41, No. 6, (2008) pp. 1024–1037.
109. Čapek, J., Máthys, K., Clausen, B., Barnett M. *Dependence of twinned volume fraction on loading mode and Schmid factor in randomly textured magnesium*. Acta Materialia. Vol. 130, (2017), 319-328.

110. Cepeda-Jiménez, C.M., Molina-Aldareguia, J.M., Pérez-Prado, M.T. *Origin of the twinning to slip transition with grain size refinement, with decreasing strain rate and with increasing temperature in magnesium*. Acta Materialia. Vol. 88 (2015) 232-244.
111. Ye Jin Kim, Jong Un Lee, Sang-Hoon Kim, Young Min Kim, Sung Hyuk Park. *Grain size effect on twinning and annealing behaviors of rolled magnesium alloy with bimodal structure*. Materials Science and Engineering: A. Vol. 754 (2019) 38-45.
112. B.Q. Shi, Y.Q. Cheng, X.L. Shang, H. Yan, R.S. Chen, W. Ke. *Hall-Petch relationship, twinning responses and their dependences on grain size in the rolled Mg-Zn and Mg-Y alloys*. Materials Science and Engineering: A. Volume 743 (2019) 558-566.
113. M.D. Nave, M.R. Barnett. *Microstructures and textures of pure magnesium deformed in plane-strain compression*. Scripta Mater. Vol. 51 (2004) 881-885.
114. S.-G. Hong, S.H. Park, C.S. Lee, *Role of {1012} twinning characteristics in the deformation behavior of a polycrystalline magnesium alloy*. Acta Materialia. Vol. 58 (2010) 5873-5885.
115. S.H. Park, J.H. Lee, B.G. Moon, B.S. You, *Tension-compression yield asymmetry in as-cast magnesium alloy*, J. Alloy. Comp. 617 (2014) 277-280.
116. S. Godet, L. Jiang, A. Luo, J. Jonas. *Use of Schmid factors to select extension twin variants in extruded magnesium alloy tubes*. Scripta Mater. Vol. 55 (2006) 1055-1058.
117. J. Jiang, A. Godfrey, W. Liu, Q. Liu, *Identification and analysis of twinning variants during compression of a Mg-Al-Zn alloy*, Scripta Mater. Vol. 58 (2008) 122-125.
118. Z. Liu, R. Xin, D. Li, L. Sun, Q. Liu, *Comparative study on twinning characteristics during two post-weld compression paths and their effects on joint enhancement*. Sci. Rep. 6 (2016) 39779.
119. F. Wang, S.R. Agnew, *Dislocation transmutation by tension twinning in magnesium alloy AZ31*, Int. J. Plast. 81 (2016) 63-86.
120. S. Xu, N. Matsumoto, S. Kamado, T. Honma, Y. Kojima, *Dynamic microstructural changes in Mg<sub>9</sub>Al<sub>1</sub>Zn alloy during hot compression*, Scripta Mater. 61 (2009) 249-252.
121. X. Li, P. Yang, L.-N. Wang, L. Meng, F. Cui, *Orientational analysis of static recrystallization at compression twins in a magnesium alloy AZ31*, Mater. Sci. Eng., A 517 (2009) 160-169.
122. A. Levinson, R.K. Mishra, R.D. Doherty, S.R. Kalidindi, *Influence of deformation twinning on static annealing of AZ31 Mg alloy*, Acta Mater. 61 (2013) 5966-5978.

## REFERENCES

---

123. D. Guan, W.M. Rainforth, L. Ma, B. Wynne, J. Gao, *Twin recrystallization mechanisms and exceptional contribution to texture evolution during annealing in a magnesium alloy*, Acta Mater. 126 (2017) 132-144.
124. D. Guan, W.M. Rainforth, J. Gao, J. Sharp, B. Wynne, L. Ma, *Individual effect of recrystallisation nucleation sites on texture weakening in a magnesium alloy: Part 1- double twins*, Acta Mater. 135 (2017) 14-24.
125. J. Hirsch, T. Al-Samman, *Superior light metals by texture engineering: Optimized aluminum and magnesium alloys for automotive applications*, Acta Mater. 61 (2013) 818-843.
126. K. Huang, R.E. Logé, *A review of dynamic recrystallization phenomena in metallic materials*, Mater. Des. 111 (2016) 548-574.
127. Y.C. Xin, M.Y. Wang, Z. Zeng, G.J. Huang, Q. Liu, *Tailoring the texture of magnesium alloy by twinning deformation to improve the rolling capability*. Scripta Mater. 64 (2011) 986-989.
128. J. Luo, W.W. Hu, Q.Q. Jin, H. Yan, R.S. Chen, *Unusual cold rolled texture in an Mg-2.0Zn-0.8Gd sheet*, Scripta Mater. 127 (2017) 146-150.
129. M.R. Barnett, Z. Keshavarz, A.G. Beer, D. Atwell, *Influence of grain size on the compressive deformation of wrought Mg–3Al–1Zn*, Acta Mater. Vol. 52 (2004) 5093-5103.
130. R.K. Sabat, S.K. Sahoo, D. Panda, U.K. Mohanty, S. Suwas, *Orientation dependent recrystallization mechanism during static annealing of pure magnesium*, Materials Characterization, Vol. 132, (2017), 388-396.